Computational Analysis for Mixing of Newtonian and Non-Newtonian Fluids Flowing through 3D Micromixers

Thesis Submitted
In Fulfillment of the Requirements
for the Degree of

DOCTOR OF PHILOSOPHY

by

MD GULAM MUSTAFA
(Roll No. 2K18/PHDME/504)

Under the Supervision of

DR. MOHAMMAD ZUNAID
(Supervisor)

PROF. SAMSHER
(Joint Supervisor)

Department of Mechanical Engineering
Delhi Technological University, Delhi
(Formerly Delhi College of Engineering)

Shahbad Daulatpur, Bawana Road, Delhi-110042, India.

March, 2025

ACKNOWLEDGEMENTS

This thesis was written during my tenure as a doctoral candidate at Delhi Technological University, Delhi. First and foremost, I am profoundly grateful to the Almighty, whose blessings of strength and patience have guided me throughout this journey of knowledge and learning.

I extend my heartfelt gratitude to my PhD supervisors, **Dr. Mohammad Zunaid** and **Prof. Samsher**, for their invaluable guidance and unwavering support in this research. Their scholarly insights and constructive feedback have been instrumental in shaping this work. I sincerely appreciate their mentorship, which has enriched my understanding of academic writing, research methodologies, and future perspectives. I am also thankful to the anonymous reviewers of our research papers for their insightful suggestions and comments, which broadened our exploration into new dimensions of the study.

I sincerely thank the members of my SRC and DRC for their willingness to be part of my doctoral examination and for their valuable feedback and thought-provoking questions, which have contributed significantly to refining this research. Additionally, I express my deep appreciation to the Department of Mechanical Engineering, Delhi Technological University, for providing the necessary facilities and support for my research endeavours.

My sincere thanks also go to Prof. Qasim Murtaza (DTU, Delhi), Prof. Nand Kumar (DTU, Delhi), Prof. Abid Haleem (JMI, Delhi), Dr. Mohd Shuaib (DTU, Delhi), and Dr. Nausad Ansari (DTU, Delhi) for their guidance, encouragement, and moral support throughout my research journey. Their inspiration has fuelled my passion for learning and steered me toward an academic career. I am genuinely grateful for their wisdom and for pushing me beyond my perceived limits.

PhD research is not a solitary endeavour, and I am deeply appreciative of my colleagues Dr. S. Lalhraitpuia, Dr. S. Ahmad, Mr. H. Sadique, Mr. R. Kumar, and Mr. V. Sharma for their engaging discussions and unwavering moral support, which played a significant role in my accomplishments. My sincere thanks go to all those who, in various ways, have contributed to this journey—your support has been truly invaluable.

Finally, I am profoundly thankful to my parents for their unwavering support and faith in me. I sincerely thank my mother, father, brothers, sisters, brother-in-law, and friends for their encouragement, care, and constant support, whether through thoughtful suggestions or countless phone calls. Their belief in me has been a pillar of strength, and I am truly blessed to have such a supportive circle.

MD GULAM MUSTAFA

DELHI TECHNOLOGICAL UNIVERSITY

(Formerly Delhi College of Engineering)

Shahbad Daulatpur, Main Bawana Road, Delhi-42

CANDIDATE'S DECLARATION

I, Md Gulam Mustafa, hereby certify that the work which is being presented in the thesis titled "**Computational Analysis for Mixing of Newtonian and non-Newtonian Fluids Flowing through 3D Micromixers**" in fulfilment of the requirements for the award of the Degree of Doctor of Philosophy, submitted in the Department of Mechanical Engineering, Delhi Technological University is an authentic record of my work carried out during the period from 01-01-2019 to 30-12-2024 under the supervision of Dr Mohammad Zunaid and Prof. Samsher. I have not submitted the matter presented in the thesis for the award of any other degree from this or any other institute.

Place: Delhi

MD Gulam Mustafa

(2K18/PhD/ME/504)

DELHI TECHNOLOGICAL UNIVERSITY

(Formerly Delhi College of Engineering)

Shahbad Daulatpur, Main Bawana Road, Delhi-42

CERTIFICATE BY THE SUPERVISORS

Certified that **Md Gulam Mustafa (**2K18/PHDME/504) has carried out their research work presented in this thesis entitled **"Computational Analysis for Mixing of Newtonian and non-Newtonian Fluids Flowing through 3D Micromixers"** for the award of **Doctor of Philosophy** from Department of Mechanical Engineering, Delhi Technological University, Delhi, under our supervision. The thesis embodies the results of the original work carried out by the candidate. The contents of the thesis do not form the basis for the award of any other degree to the candidate or anybody else from this or any other University/Institution.

Dr. Mohammad Zunaid
(Associate Professor)
Department of Mechanical Engineering
Delhi Technological University,
Delhi-110042

Dr. Samsher
(Professor)
Department of Mechanical Engineering
Delhi Technological University,
Delhi-110042

ABSTRACT

In microfluidic systems, fluid mixing is critical for applications in chemical synthesis, drug delivery, diagnostics, and lab-on-a-chip technologies. However, achieving efficient mixing in microscale environments is challenging due to the predominance of laminar flow and low Reynolds numbers, which limit turbulence. This thesis addresses these challenges by computationally analyzing the mixing of Newtonian and non-Newtonian fluids in 3D micromixers using advanced numerical simulation techniques.

The study systematically investigates the performance of various micromixer geometries, such as hybrid T-junction designs, focusing on their ability to enhance mixing through passive mechanisms. The analysis also examines how fluid rheology (the flow behaviour of fluids, particularly Newtonian vs. non-Newtonian) influences mixing performance. Non-Newtonian fluids, such as polymer solutions or biological fluids, often exhibit complex behaviours like shear-thinning or shear-thickening, significantly impacting flow patterns and mixing efficiency.

A crucial part of this research involves studying operational parameters such as inlet velocity, Reynolds number, and fluid viscosity. These parameters affect the flow regime and mixing dynamics, and understanding their influence is key to optimizing micromixer design. Another novel aspect of the study is the incorporation of nanoparticles, which are increasingly used in microfluidic systems for enhanced mixing, heat transfer, and targeted delivery. The thesis explores how nanoparticle size, concentration, and distribution influence the mixing index—a quantitative measure of mixing quality.

By comparing Newtonian and non-Newtonian fluid mixing in the presence and absence of nanoparticles, the study provides valuable insights for designing efficient micromixers tailored to specific applications. These findings advance the fundamental understanding of microscale fluid dynamics and offer practical guidelines for developing next-generation microfluidic devices.

The initial design is motivated by a simple-T micromixer using different twists and bends. Ansys fluent with finite volume analysis, conducts a simulation for this parameter. We investigate the impact of twist and bend on mixing performance and pressure drops. For data analysis, we consider the twist, bend angle, and Reynold number as input variables and mixing index and pressure drop as outputs variables for training using a neural network. With the moth flame optimization algorithm, the micromixer model was optimized for the maximum mixing performance and the minimum pressure drop. The optimal value for the twist and bend angle is 4 and 70°, respectively, at Reynold number (Re) 10. This technique has a significant benefit for microfluidic channel optimization.

Using metaheuristic algorithms for a novel passive micromixer featuring bends and twists with offsets. The twists and bends cause constant changes in the direction of liquid flow, leading to chaotic advection that enhances species mixing while minimizing pressure loss. Although increasing channel length generally improves mixing performance, the proposed design's performance was higher than the reference channel for Reynolds numbers (Re) greater than 100. Key findings include achieving an excellent mixing performance of 87.76% at a Reynolds number of 400, with a bend angle of 60° and a twist factor of 4. The Harris Hawk Optimization (HHO) algorithm was most effective for optimizing microfluidic channel designs**.**

Keywords: Numerical Modelling; Mixing Index; CFD; Micromixing; Thermo-Fluidic; Passive Micromixer; Moth Flame Optimization; Haris Hawk Optimization; Response Surface Method;

LIST OF FIGURES

LIST OF TABLES

LIST OF SYMBOLS

D_h	Hydraulic Diameter	u	Velocity
η	Mixing Index/Efficiency	μ	Dynamic Viscosity
Re	Reynold Number	ρ	Density of fluid
PI	Performance index	τ	Dimensional time
p	Dimensional Pressure	υ	Kinematic viscosity
c	Species Concentration	σ	Variance of concentration
N	Sample Size	R	Correlation function
U	Velocity scale characteristic	R^2_{adj}	Fit Goodness
U_i	Velocity vector components	f	Force vector
V_p	Velocity of particle	k_B	Boltzmann constant
c_p	Specific heat	λ	Mean free path
D	Diffusion coefficient	De	Dean Number
$\bar{u}$	Mean velocity	$\bar{C}$	Mean species concentration
w	Channel width	ΔP	Pressure drops
L	Channel length	γ	Fluid diffusion coefficient
d	Channel depth	m	Mass
k	Thermal Conductivity	$\dot{\gamma}$	Shear Strain
∅	Nanoparticle volume fraction		

Abbreviation

3D	Three-Dimensional
CFD	Computational fluid dynamics
DOE	Design of experiment
MOEA	Multi-Objective Evolutionary Algorithm
GA	Genetic algorithm
LHS	Latin hypercube sampling

ANN	Artificial neural network
TBM	Twist and Bend Micromixer
OMTB	Offset twist and bend micromixer
HSTM	Helical spiral twist micromixer
MFO	Moth flame optimization
HHO	Haris hawk optimization
RSM	Response surface method
μ-TAS	Micro-total analysis system
Obfn	Objective function
C-Y	Carreau Yasuda Model

TABLE OF CONTENTS

Chapter 1 INTRODUCTION

1.1 Introduction

The degree of mixedness is a distinct characteristic that does not assess the property itself rather its uniformity. When referring to the "distribution of different masses within a specified volume," the term "mixing" describes the situation in which the masses in question differ in at least one property, such as density, colour, or viscosity. Mixing aims to achieve uniformity in the components and, consequently, in the properties mentioned. The level of mixedness must reflect both the definition of mixing and the goals of the mixing process. Typically, information is restricted to temporal and local concentration functions in molecular-disperse systems. For quantitative analysis of the data, it is necessary that the properties of the "pure" components and all mixing conditions be measurable factors.

Depending on the application, reducing the length scales on which variations occur, their amplitudes, or both is often desired. In some cases, simply decreasing the scale at which segregation remains below a certain threshold may be enough to achieve the desired product quality, such as in blending processes. However, mixing at the molecular level is essential for any chemical reaction. Molecular diffusion, a mechanism driven by the random thermal motion of individual particles, is the only mechanism utilized in this process. Over the time, these random movements lead to a statistically homogeneous distribution of properties within a system. However, molecular diffusion only influences the large-scale distribution of a property when spatial gradients exist. Convective mixing—at the macro or mesoscopic scale—is crucial to enhance or control this process. It can perform its role by creating steep property gradients or lowering the characteristic length scale across these gradients. Although the ultimate goal is to achieve uniformity, convective mixing accelerates the process by intensifying local differences, thereby enhancing the effectiveness of molecular diffusion. The rate of many reactive processes is often controlled by mixing rather than diffusion, highlighting the importance of gaining a deeper understanding of the mixing process.

1.2 Motivation

Micromixers are pivotal components in modern microfluidic systems, playing a crucial role in various applications such as biomedical devices, chemical processing, and lab-on-a-chip technologies. These devices facilitate the rapid and efficient mixing of fluids at the microscale, which is essential for numerous biochemical assays and analyses. The design and operation of micromixers are carefully engineered to align with the specific requirements of their intended applications. These devices utilize passive and active mixing strategies, offering distinct advantages regarding efficiency, control, and adaptability.

Passive micromixers use intricate channel geometries, such as serpentine, herringbone, or chaotic advection structures, to enhance mixing through diffusion and fluid inertia without requiring external energy input. This approach mainly benefits applications demanding simplicity, low power consumption, and integration into lab-on-a-chip systems.

On the contrary, active micromixers use external forces, such as acoustic waves, magnetic fields, electrokinetic fluxes, or mechanical agitation, to dynamically alter the movement of fluids and increase the mixing efficiency. These methods enhance controllability, enabling precise modulation of mixing rates in response to varying process conditions.

By strategically integrating these mixing mechanisms, micromixers can be optimized for diverse applications, ranging from chemical synthesis and biomedical diagnostics to drug delivery and environmental monitoring. The choice of design and mixing strategy ultimately depends on factors such as fluid properties, mixing time constraints, and the level of control required for the specific process.

The following sections delve into the broader importance of micromixers and their roles in contemporary applications.

1.2.1 Biomedical applications

Micromixers are integral to lab-on-a-chip systems for sample preparation, drug delivery, and biological synthesis. They enable rapid and homogeneous mixing, crucial for processes like polymerase chain reaction (PCR) amplification, DNA hybridization, and enzyme assays ("Analysis, Design and Fabrication of Micromixers, Volume II", 2023) ("Recent advancements in induced-charge electrokinetic micromixing", 2022).

In biomedical devices, micromixers facilitate precise control over mixing concentrations, which is vital for diagnostic applications and the manipulation of genetic material (Takayama & MAKI 2024, Hassani et al. 2024).

1.2.2 Chemical processing

i. In chemical analysis, micromixers enhance reaction rates and improve the efficiency of chemical processes by ensuring uniform mixing of reactants. This is particularly important in nanoparticle synthesis and other chemical assays where precise control over reaction conditions is required (Hassani et al. 2024) (Wang et al. 2023).

ii. The use of micromixers in chemical processing also reduces reagent costs and enhances safety by minimizing the volume of hazardous chemicals needed for reactions (Wang et al. 2023).

1.2.3 Lab-on-a-chip technologies

i. Lab-on-a-chip innovations, which integrate laboratory tasks onto a single chip, require micromixers as an essential component.

ii. These systems are used for environmental monitoring, disease diagnosis, and new energy applications (Han et al. 2024).

iii. Incorporating micromixers into lab-on-a-chip devices makes it possible to miniaturize laboratory procedures, resulting in portable and cost-effective solutions for conducting complicated tests (Kim 2022).

1.2.4 Design and innovation

The design of micromixers continually evolves, with innovations in passive and active mixing strategies. Passive micromixers rely on complex geometries to enhance mixing through diffusion and chaotic advection, while active micromixers use external energy sources like magnetic or electric fields for precise control (Soltani et al. 2024, Bazaz et al. 2024).

Recent advancements in manufacturing techniques, such as 3D printing, have facilitated the development of novel micromixer designs, enabling more efficient and customizable mixing solutions (Soltani et al. 2024).

1.3 Microscale Mixing

This discusses the design and characteristics of micromixers, compact mixing devices that combine at least two phases: liquids, solids, or gases. Micromixers are partially or entirely fabricated with microtechnology or precision engineering techniques, featuring channels typically sized in the submillimetre range. Standard channel widths range from 100 to 500 micrometres, with several millimetres or more channel lengths and heights similar to or smaller than the width. The total volume of a micromixer spans from microliters to millilitres. Micromixers operate on a much larger scale in comparison to molecular dimensions, which results in two principal characteristics: first, their design focuses on manipulating flow through channel geometry or external forces, and second, although they introduce new advantages to molecular-level chemical engineering processes, such as reaction kinetics, they remain largely unaffected.

The mixing process helps to move species, temperature, and phases to reduce the amount of inhomogeneity that exists. This process also induces secondary effects, like chemical reactions and changes in material properties. In conventional large-scale mixing methods, three primary mixing levels are defined: micromixing, mesomixing, and macromixing. Macromixing pertains to mixing facilitated by the most significant fluid motions, often characterized by the diameter of the mixing vessel. Micromixing transpires at the most minor fluid and molecular motion scales, typically at the level of turbulent eddies, referred to as the Kolmogorov scale. Between the macro and micro scales is mesomixing. In micromixers, transport may still be classified as micromixing even with micrometre-sized structures. Since micromixer dimensions can approach the Kolmogorov scale, this text avoids using "micromixing" to describe mixing processes within them.

Mixing can be achieved in macroscale systems through various mechanisms such as eddy diffusion, molecular diffusion, Taylor dispersion and advection. Eddy diffusion involves transporting large groups of particles and relies on turbulent flow. However, due to the strong influence of viscous forces at the microscale, turbulence does not occur in micromixers, making eddy diffusion irrelevant to them. Hence, the key mixing processes are micromixers' molecular diffusion, advection, and Taylor dispersion. The molecular diffusion coefficient is a measure used to quantify the phenomenon of molecular diffusion caused by the random motion of molecules. Advection, driven by fluid motion, can produce chaotic distribution in mixed species through a simple Eulerian velocity field. Even in a stable, laminar flow, chaotic advection can still occur, making it suitable for micromixers. In contrast to axial dispersion, which results from a combination of advection and the interdiffusion of fluid layers moving at different speeds, velocity gradients induce Taylor dispersion, a specific kind of advection. This technique speeds up mixing by Taylor dispersion by two to three times that of mixing by molecular diffusion alone.

Since existing macroscale designs cannot be quickly shrunk for microscale applications, creating micromixers constitutes a new branch of engineering. One of the primary challenges in this miniaturization is that surface effects become more dominant than volume effects. Many actuation methods that depend on volume forces, which are highly effective at the macroscale, encounter significant challenges when

applied at the microscale. This issue primarily arises in microscale fluid systems due to the predominance of surface forces, which include surface tension and viscosity, over volumetric forces, including gravity and inertia. As a result, techniques that work efficiently in larger systems often fail to achieve the same level of performance in microfluidic environments.

A clear example of this limitation is the conventional magnetic stirrer, which illustrates the fundamental difference between surface and volume forces. A standard magnetic stirrer generates a rotating magnetic field, typically using a combination of a bar magnet (stirring bar) and a rotating or stationary external magnet. This setup effectively induces fluid motion at the macroscale and enhances mixing through bulk flow and turbulence. However, at the microscale, the influence of viscous forces becomes dominant, significantly suppressing inertial effects and preventing the formation of turbulent flow. Consequently, the effectiveness of traditional stirring mechanisms diminishes, necessitating alternative mixing approaches specifically designed to leverage microscale physics.

To address these challenges, microfluidic systems often employ specialized mixing techniques, such as electrokinetic stirring, acoustically driven mixing, or magnetically actuated micro-rotors, which are tailored to operate within the constraints of microscale fluid dynamics. These methods exploit localized forces and controlled actuation strategies to achieve efficient mixing without relying on the large-scale turbulence characteristic of conventional macroscopic mixers.

The magnetic driving force depends on the magnet's volume, whereas the friction force depends on its surface area. When scaling down, this relationship follows the cube-square law: reducing the stir bar's size by ten would decrease its volume by roughly 1000 times but only reduce its surface area by about 100 times. At its initial magnitude, the magnetic field produces a force equivalent to the frictional force, enabling the stir bar to move. However, shrinking the stir bar by 10 times reduces the driving force to only 1/10th of the friction force, preventing movement. In contrast, an actuation approach based on surface forces would scale down more effectively, as the friction force to the driving force would remain constant.

At the microscale, mixing processes that include immiscible interfaces are also influenced by dominating surface phenomena. In a solid-liquid system, mixing begins by suspending solid particles, with dissolution following afterwards. The high surface-to-volume ratio at the microscale benefits the dissolution process, making it relatively straightforward. Consequently, the primary challenge lies in achieving suspension. Due to their larger size and low diffusion coefficients, particles can only be effectively suspended at this scale through chaotic advection. The effectiveness of the suspension process significantly determines the efficacy of solid-liquid mixing over a small scale.

Extra energy is required to overcome interfacial tension in a system involving immiscible liquids. While dispersing these immiscible phases is challenging, surface tension helps by breaking the stretched fluids into segments, forming microdroplets. At the microscale, this droplet formation can be precisely controlled for each droplet. As a result, micromixers can produce emulsions with uniform droplet sizes.

Dominant surface effects also impact gas-liquid systems. Dispersion of gas and liquid is essential for various chemical reactions, including hydrogenation, oxidation, carbonation, and chlorination. In contrast to liquid-liquid emulsions, which are separated from one another, gas molecules can be absorbed into the liquid phase while maintaining their integrity. Gas-liquid mixing involves two main steps: gas bubble dispersion and gas molecule absorption. Although the larger interfacial area enhances absorption, the primary challenge in designing micromixers for gas-liquid systems is achieving effective dispersion of fine gas bubbles.

In addition to surface phenomena, laminar flow conditions present a challenge when designing micromixers. Due to the high viscosity and low flow rates involved, similar problems exist with laminar mixers at the macroscale. These mixers are extensively employed in the food, biotechnology, and pharmaceutical sectors. Because of their diminutive size, micromixers create significant shear stress even at very low velocities. This means the flow velocity cannot be excessively high in many micromixer applications. This shear stress can damage cells and other sensitive bioparticles. High shear stress can cause the fluid to behave non-Newtonian in complex fluids containing large molecules or cells. High shear may compromise cells'

metabolic and structural integrity, while the resulting viscoelastic effects can cause flow instability, enhancing mixing.

Miniaturization alters the timescale of mixing processes. Micromixers are primarily used as platforms for analytical or synthetic reactions, where mixing and chemical reactions are closely linked. Although reaction kinetics and time of response remain unchanged with miniaturization, mixing time can vary significantly depending on the design and type of micromixer. This variation brings two key considerations in chemical reactions: accurately measuring real reaction kinetics and controlling reaction products.

At larger scales, the mixing process frequently occurs significantly slower than the intrinsic reaction kinetics. This means that the total reaction rate is predominantly driven by the rate of mixing rather than the speed at which the chemical reaction happens. In such cases, incomplete or slow mixing can lead to concentration gradients, non-uniform reactant distributions, and diffusion-limited reaction kinetics, ultimately constraining the system's efficiency and performance.

However, at the microscale, mixing times can be dramatically reduced due to the short diffusion distances and the ability to control fluid flow precisely. In microfluidic systems, mixing can occur on timescales comparable to, or even shorter than, the reaction times. This fundamental shift allows chemical reactions to proceed under conditions where mass transfer limitations are minimized or eliminated, enabling a more accurate measurement of intrinsic reaction kinetics.

Researchers and engineers can study reaction mechanisms in greater detail by achieving rapid and efficient mixing at the microscale, uncovering kinetic parameters without interference from macroscopic mixing constraints. This capability is particularly valuable in catalysis, pharmaceutical development, and synthetic chemistry, where precise kinetic analysis is crucial for optimizing reaction conditions and designing efficient processes. Furthermore, microfluidic platforms provide a controlled environment for high-throughput screening of reactions, enabling rapid experimentation and real-time monitoring of dynamic chemical processes.

At the microscale, mixing duration and reaction products may be regulated. Mixing time will primarily influence the reaction rate if the reaction yields a single product. However, if multiple products are formed, mixing time will dictate the composition and distribution of these products. The following example demonstrates how the type of mixing affects the reaction outcome: Consider a reaction between substrate S and reagent R.

$$S + R \rightarrow P_1 \tag{1.1}$$

P_1 is the result of the intended reaction; however, it is also possible for P_1 to react with R, which yields a product that is not desired, which is P_2.

$$P_1 + R \rightarrow P_2 \tag{1.2}$$

1.4 Degree of Homogeneity and Scale of Segregation

The design must use metrics to evaluate the quality of mixes while assessing mixing. The intensity of segregation is an example of an integral measure that can be useful for practical applications. Variance-based measurements, on the other hand, are especially pertinent when considering reactive mixing. Despite this, variance alone cannot account for the scales on which segregation occurs; hence, an integral scale of segregation supplements variance. This scale is strongly associated with the idea of contact area, and it is possible to compute it effectively by utilizing a formula derived from geometric measure theory. The pace at which the total variation flow, which is a term from image processing intended to eliminate sharp contrasts, may vary segregation intensity, is another important feature used to define the integral scale of segregation. This approach provides insight into how rapidly variations in concentration are smoothed out within a system, offering a mathematical framework for analyzing the dynamics of mixing and segregation at different scales.

A unique dependency on the Schmidt number is revealed by the integral scale of segregation when it is applied to secondary flow mixing in a T-shaped micromixer. This number is used to quantify the relative effect of momentum diffusion (viscosity) against mass diffusion. This relationship highlights the impact of fluid properties on

the effectiveness of mixing. It underscores how changes in diffusivity and viscosity influence the distribution of segregated regions within the microfluidic environment.

In contrast, the shortest length scales of segregation exhibit a dependence analogous to Batchelor's length scale, which describes the minor scales at which scalar mixing occurs in turbulent or laminar flows. This suggests that, at finer length scales, the interplay between diffusion and flow structures follows classical mixing theories. In comparison, at larger integral scales, new dependencies emerge due to the complexities introduced by secondary flow patterns. Understanding these relationships is essential for optimizing micromixer designs, as it allows for precise control over mixing efficiency and minimises segregation within microfluidic systems.

Quantitative approaches are required to evaluate mixing efficiency to optimize mixing devices or processes successfully. Since mixing depends on relative motion inside the material, it is essential to have a solid grasp of the underlying kinematics. In particular, when it comes to the mixing of fluids, doing a thorough analysis of the velocity field can provide a wealth of helpful information concerning convective mixing. Techniques from the mathematical theory of dynamical systems are applied to measure the efficacy of mixing. These techniques include Poincaré sections, length and area-stretch rates, and Lyapunov exponents. These techniques are discussed in Ottino's monograph from 1989. The Lyapunov exponent is a measurement that determines how sensitive flow paths are to beginning circumstances. This sensitivity may be used to determine whether or not chaotic advection is present (Aref 1984). For the sake of this study, the velocity gradient $\iiint \mathrm{v}$, also known as the rate of strain tensor, is an essential parameter.

$$\mathrm{D} = (\Delta \mathrm{v} + \Delta \mathrm{v}^{\mathrm{T}}) \tag{1.3}$$

Since D represents the component of ∇v associated with relative motion, in viscous fluids, this motion results in the dissipation of energy (ε) at a specific rate

$$\varepsilon = 2\upsilon \mathrm{D}: \Delta \mathrm{v} \tag{1.4}$$

where ν denotes the kinematical viscosity.

Mixing reactants influences the rate of a chemical reaction, as the response requires a homogeneous mixture. Therefore, the rate at which the reaction occurs is directly related to the homogeneity of the mix and can serve as an indicator of the degree of homogeneity. This is especially true for the usual bimolecular reaction of this kind.

$$A + B \xrightarrow{k} P \tag{1.5}$$

$$kC_A C_B = \frac{1}{|V|} \int_V kC_A C_B dV \tag{1.6}$$

as an indicator of the mixing degree within the domain V, where $|V|$ represents the spatial region volume V. $kC_A C_B$ is the reaction rate based on mass action kinetics, with C_B and C_A denoting the molar concentrations of B and A, respectively.

Numerical tracer experiments are becoming increasingly crucial for analyzing mixing processes. However, a substantial challenge occurs when combining very viscous liquids or, more broadly, dealing with large tracer Schmidt numbers. In these situations, the accuracy of the species equation solution can be compromised by "numerical diffusion," which refers to the artificial smoothing of the tracer profile caused by discretization errors. This numerical diffusion can be much stronger than the actual physical diffusion. One solution to this problem is replacing the continuous tracer concentration with several concentrations derived from Lagrangian (inertia-free) particles tracked during the simulation. The Brownian motion of diffusive particles must be taken into consideration while utilizing this technique; however, in order to do so, random displacements that are based on a Wiener process must be incorporated. More details on the tracking of Lagrangian particles in mixing estimations may be found in the most recent work that was produced by (Phelps and Tucker 2006).

To accurately assess mixing quality, the degree of segregation must be considered alongside a quantifiable measure of the segregation scale. There are several approaches to defining this scale. One standard method is to derive it from a given

measure of segregation intensity. In batch mixing processes, where species mass is conserved due to impermeable boundaries, the rate described in (section 1.6) corresponds to the decay rate of variance. Defining a meaningful scale of segregation for a scalar quantity requires understanding the distribution's structure. In convection-dominated mixing, small-scale structures often exhibit a lamellar pattern, which arises, for example, when the interface between regions of higher and lower concentration is twisted into secondary, vortex-like velocity fields.

1.5 Types of Micromixers

Micromixers are classified into two categories: active and passive. Active micromixers enhance mixing by utilizing moving parts or external energy sources, such as magnetic fields, electrical energy, pressure disturbances, or ultrasonic waves, to stir the fluids. In contrast, passive micromixers rely on geometrical modifications to induce chaotic advection or lamination, promoting fluid mixing without needing external energy. These passive designs are more straightforward to fabricate and integrate into lab-on-a-chip and micro-total analysis systems (μ-TAS).

This section covers both active and passive micromixers, primarily focusing on the design and mechanisms of passive micromixers and their applications. While it is not feasible to provide an exhaustive review of all active and passive micromixers due to space constraints, an effort is made to introduce a broad range of micromixer designs and concepts.

Typically, micromixers possess dimensions that fall within the sub-millimeter range. Channel widths and heights range from 100 to 500 μm, and lengths up to a few millimetres. The limits of the microfluidic platform for particular applications determine these dimensions. Microfluidic systems offer some benefits in comparison to large-scale mixing devices. These benefits include reduced sample consumption, lower production costs, and greater throughput.

On the other hand, mixing at the microscale creates difficulties because laminar flow within the channels (with Reynolds numbers ranging from 0.01-1000) is brought about by the predominance of viscous forces. That being the case, the random

turbulent fluctuations necessary for the fluid's homogeneity are absent at this site. In its place, micromixing is principally dependent on advection and diffusion processes. In laminar flows, diffusional mixing is a sluggish process requiring considerable channel lengths to complete mixing. In this context, it is essential to remember that the dimensions of the microfluidic platform constrain the length of the channel. The diffusion process is determined by the molecular diffusion coefficient, which usually has a value of around $10e{-}10\ m^2s^{-1}$ for tiny proteins in aqueous solutions.

Advection, on the other hand, improves mixing by straining and flexing the fluid surface. This is how it takes place. Consequently, the interfacial area is expanded, which results in an improvement in mass transfer, a reduction in the thickness of the striation, an acceleration of the mixing process, and an increase in the concentration gradient. All of these outcomes are advantageous.

Researchers have created various micromixers, which may be roughly classified as active or passive, to optimize the mixing process on a microscale. Passive micromixers use channel geometry to create complex flow fields for efficient fluid mixing and require no external energy. On the other hand, active micromixers improve mixing performance by using moving components or external energy sources, such as magnetic, electrical, pressure-based, or ultrasonic. While active micromixers achieve higher mixing efficiency, passive micromixers are more straightforward to design, fabricate, and integrate into complex systems.

The authors (Hardt & Schönfeld 2003) classified passive micromixers based on the underlying hydrodynamic principles, including flow separation, chaotic advection, hydrodynamic flow splitting and recombination focusing. Their review aimed to guide micromixer designers in selecting the optimal concept for specific applications. Similarly, (Nguyen and Wu 2005) reviewed micromixer developments based on various working principles, focusing on the design and mechanisms of passive micromixers. They also discussed operating conditions, fabrication techniques, and mixing characterization.

The authors (Hessel, Löwe, and Schönfeld 2005) comprehensively reviewed active and passive mixing principles, covering typical mixing element designs,

characterization methods, and application areas, including gas mixing in microchannels. A comprehensive review of the relevant literature investigated the operating ranges of passive and active micromixers about Re and Pe numbers (Kumar et al. 2017). Passive micromixers demonstrated wider operational ranges, with $0.001 \leq Re \leq 10000$ and $0.01 \leq Pe \leq 1,00,000$. While micromixers built for diffusive mixing function effectively at low Reynolds and Peclet numbers, those that use chaotic advection are successful throughout a wider Reynolds number range.

1.5.1 Passive Micromixers

Passive micromixers utilize the geometry of their channels to create intricate flow fields, enabling efficient mixing without the need for moving parts. They can be manufactured in both planar and three-dimensional configurations. Basic designs, including T-shaped and Y-shaped microchannels, have been widely investigated through experimental and numerical studies to understand fundamental mixing dynamics (Kockmann et al. 2006a).

Dreher et al. investigated T-shaped micromixers over a wide range of Reynolds numbers (0.01–1000), identifying different flow regimes based on Reynolds numbers, including stratified, vortex, and engulfment flows. The engulfment flow at high Reynolds numbers significantly improved mixing efficiency among these. (Kockmann et al. 2006b) examined mixing behaviours in various mixer designs, such as asymmetric T-mixers, T-tree mixers, and tangential mixers. (Afzal and Kim 2014) studied T- T-micromixers with non-Newtonian fluids microchannels employing shear-dependent viscosity models, finding that at higher flow rates, mixing efficiency increased for Newtonian fluids like water but showed negligible improvement for non-Newtonian fluids like blood.

(Ansari et al. 2012) introduced a vortex micro-T-mixer featuring tangentially aligned inlet channels, creating a vortex at the inlet to stretch and fold the fluid interface, thereby improving mixing efficiency.

Passive micromixers are typically classified into two main categories:

i. Multi-lamination and focusing: This approach splits a fluid stream into multiple sub-streams to increase surface contact for diffusion-based mixing. In some designs, designed interdigital micromixers featuring alternating feed channels to generate periodic liquid lamellae, significantly decreasing mixing time to mere milliseconds (Hessel et al. 2003).

ii. Chaotic advection: Involves stretching, folding, and breaking flow patterns to increase fluid mixing. This is achieved through channel geometries with surface patterning, serpentine channels, obstacles, and split-and-recombine paths. (Stroock et al. 2002) introduced staggered herringbone grooves to generate transverse flows, significantly enhancing mixing. Numerical studies by (Yang, Huang, and Lin 2005) and experimental work by (Wang, Yang, and Lyu 2007) highlighted the importance of geometric parameters and overlapping crisscross inlet designs for superior performance.

1.5.1.1 *Serpentine channels and dean vortices*

Curved channels with rectangular or circular cross sections generate Dean vortices through centrifugal forces, improving mixing by stretching and folding fluid interfaces. (Liu et al. 2000b) 3D serpentine channels with C-shaped units outperformed planar serpentine channels, achieving near-complete mixing at Reynolds numbers as low as 70.

1.5.1.2 *Obstructions in flow channels*

Adding obstacles, such as cylindrical or diamond-shaped structures, to channels enhances mixing by breaking and recombining flows. (Bhagat, Peterson, and Papautsky 2007) demonstrated that spatial arrangements of flow breakup obstructions in microchannels resulted in excellent mixing performance at low Reynolds numbers ($Re < 1$). (Alam, Afzal, and Kim 2014) further highlighted the superior mixing efficiency of curved channels with cylindrical obstructions compared to simple curved channels or T-channels.

Additional designs include planar micromixers with sinusoidal or zigzag patterns and complex 3D micromixers fabricated using advanced techniques like stereolithography. These studies underline the versatility of passive micromixers in achieving efficient mixing across a wide range of flow conditions.

1.5.2 Active Micromixers

Active micromixers enhance mixing efficiency by incorporating external energy sources such as pressure fluctuations, acoustic waves, mechanical vibrations, rotating impellers, and electric or magnetic fields. These energy inputs generate controlled fluid disturbances, promoting faster and more effective mixing than passive methods. Active micromixers can be classified into various categories depending on the specific external force utilised, each optimized for different applications and fluid dynamics:

i. Pulsed Flow**:** Comprehensive research on pulsed flow in T-mixers with different configurations and operating conditions was carried out using CFD and experiments (Glasgow & Aubry, 2003a, 2003b). They applied a low-frequency sinusoidal flow superimposed on steady flow, observing significant improvements in mixing compared to steady-state conditions. For instance, in one study (Glasgow, Lieber, and Aubry 2004), ribbed and 3D twisted micromixers showed enhanced mixing under pulsed flow. More recently, (Afzal and Kim 2015) demonstrated that a sinusoidal wall channel coupled with pulsatile flow achieved a mixing index of 92% between the two sinusoidal input periods, rapidly increasing the interfacial area and producing discrete fluid puffs.

ii. Electrokinetic Flow**:** Electrokinetic micromixers use fluctuating electric fields to enhance mixing as an alternative to pressure-driven flows (Jacobson, McKnight, and Ramsey 1999; El Moctar, Aubry, and Batton 2003; Oddy, Santiago, and Mikkelsen 2001). The interaction of electric fields with ionic conductivity creates electric body forces that induce flow instabilities, improving mixing efficiency. Oddy et al. developed electrokinetic micromixers for bioanalytical applications, leveraging electroosmotic flow instabilities at low Reynolds numbers to mix fluid streams effectively.

iii. Magnetohydrodynamic Flow**:** Magnetohydrodynamic micromixers use magnetic fields and suspended magnetic particles in the fluid to improve mass transport (Bau, Zhong, and Yi 2001; Fu et al. 2010; Hejazian and Nguyen 2017; Tsai et al. 2009). Tsai et al. and Fu et al. enhanced the efficiency of Y-shaped micromixers by incorporating ferrofluids and permanent magnets to generate magnetoconvective flow. This approach leverages the interaction between the magnetic field and the ferrofluid, creating controlled fluid motion that accelerates mixing. Optimizing magnet placement and fluid properties significantly improves mixing performance, making it suitable for applications requiring rapid and homogeneous mixing at microscale levels. Hejazian et al. employed an irregular magnetic field, a hydrodynamic flow and a diluted ferrofluid-focusing configuration in a microfluidic system to enhance mass transport. The system achieved improved mixing by generating secondary magnetoconvective flows.

iv. Acoustic-Induced Flow**:** (Liu et al. 2002) introduced a bubble-induced acoustic microstreaming technique. Their micromixer incorporated a piezoelectric disk attached to a reaction chamber, trapping air bubbles of specific sizes. Vibrations generated circulatory flows via sound fields acting on the bubbles, dramatically reducing mixing time from hours (diffusion-based) to seconds for a 100 μL chamber.

v. Coriolis Force-Induced Flow**:** (Haeberle et al. 2005) proposed a centrifugal mixing concept using Coriolis forces generated by a rotating system. This method rapidly mixed with high throughput.

Comprehensive reviews of active micromixer designs and applications are available in the works of (Nguyen and Wu 2005), (Hessel et al. 2005), and (Kumar, Paraschivoiu, and Nigam 2011). These reviews provide detailed insights into the mechanisms and effectiveness of various active micromixer designs.

1.6 Mixing Mechanism

Micromixers can operate across a broad range of Reynolds numbers, with their mixing mechanism and performance heavily influenced by the Reynolds number regime.

When the Reynold number is low (Re<1), the mixing process is mainly caused by diffusion, which is contingent upon the duration of residence of the fluids co-occurring within the micromixer. With Reynold number increased, the amount of time the fluids spent in the mixer decreased, resulting in a lower mixing performance. Transverse flows begin to build up within the channel, which causes the mixing index to significantly increase with successive increases in the Reynolds number when the mixing index is at a minimum. This occurs as the Reynolds number continues to climb. This rapid improvement in mixing efficiency is due to the stretching and folding of fluid layers, which expand the fluid interface and promote chaotic advection.

In the microchannel at Re=10, the region where mass transfer occurs mostly by diffusion at the intersection of fluids of differing concentrations, concentration contours show discrete strata that are closely aligned with one another. At Re=55, on the other hand, the fluid layers become misaligned as a result of the stretching and folding of the interface, which brings about an even more significant improvement in mixing efficiency.

Mixing at T-junctions has been investigated concerning aspects like the impact of the mixer's aspect ratio, flow regimes, fluid speed, and strategies to improve mixing efficiency. Sultan et al. (Ashar Sultan et al. 2012) observed four distinct flow patterns in the T-junction micromixer:

i. Segregated flow regime: At low Reynolds numbers, two fluid streams flow in parallel from the source to the exit without significant mixing, maintaining a stable flow regime.
ii. Vortex flow regime: Each jet contains vortices, and their rotation axis is parallel to the axis of the micromixer channel.
iii. Engulfment flow regime: Under continuous flow conditions, the fluid patterns deviate from parallel to the channel axis and rotate across it, transporting the fluid from one end to another.

iv. Chaotic flow regime: It can be recognised by the evolution of a vortex street that travels through a micromixer, allowing the two jets to mix quickly. In the chaotic flow regime, a highly dynamic state of fluid motion, vortices form immediately after jet impingement but dissipate just as quickly. It is estimated that the diameter of these vortices is roughly equivalent to half the breadth of the mixing channel. The vortex channel, which begins at the point where the jets collide and extends toward the outlet, allows the fluid that enters from the two intake jets to become contained inside its confines.

Improving the design of micromixers can enhance the efficiency of these devices and encourage more research on microdevice production techniques. Due to the swift advancement of manufacturing techniques, constructing prototypes of optimised micromixers in the following years is becoming increasingly viable and cost-effective. By taking advantage of the opportunity to build inexpensive prototypes, testing and confirming the effectiveness of the optimised designs is necessary.

Dataset creation presents the first hurdle for the optimization process. The expenditure on experimentation will increase with only experimental methods, as many geometries have to be constructed and tested in different configurations. Aside from the processing expense, the computational calculation technique based on CFD takes much time for a definitive number of simulations. Optimization eliminates many experimental and simulation simulations (Dehghani et al. 2020; Nimafar, Viktorov, and Martinelli 2012). ML is an innovative technique; it induces data and enables prognosis to develop faster than the traditional CFD method. Although many studies integrate ML with CFD, the literature review indicated that ML is rarely used in microfluidics. For micromixer performance enhancements, (Lv, Chen, Wang et al. 2022) optimization technique for a micromixer model for fractal baffle design was proposed using grey relational analysis. To optimize a cantor fractal micromixer, you can use a multi-objective evolutionary algorithm (MOEA) to search for solutions that balance the conflicting objectives of mixing efficiency (η) and pressure drops (ΔP) (Lv, Chen, Li, et al. 2022). The MOEA can optimize the geometric parameters of the

cantor fractal baffles, such as their size, shape, and spacing, to find solutions that maximize mixing efficiency while minimizing pressure drop.

Nanofluids are engineered colloidal suspensions consisting of a base fluid (such as water, ethylene glycol, or oil) and nanoparticles (typically metal, metal oxide, or carbon-based materials) with sizes ranging from 1 to 100 nm. The addition of nanoparticles significantly alters the base fluid's thermal, rheological, and flow properties, making them highly beneficial for heat transfer and fluid flow applications. When introduced into micromixers, nanofluids offer several advantages that can improve mixing efficiency:

i. Brownian Motion Effect - The random motion of nanoparticles at the nanoscale enhances mixing by creating micro vortices and disrupting the laminar flow.
ii. Altered Fluid Viscosity - Nanoparticles modify the fluid's viscosity, impacting flow characteristics and mixing efficiency.
iii. Surface Interactions – Nanoparticles can interact with channel walls, promoting chaotic advection and improving fluid dispersion.
iv. Tunable Fluidic Devices – Development of smart fluids with programmable mixing properties using external magnetic fields.
v. Chemical and Pharmaceutical Processing – Controlled mixing of reagents for microreactors and nanoparticle synthesis.
vi. Biomedical and Lab-on-Chip Devices – Precise manipulation of biofluids for diagnostics, drug delivery, and cell sorting.

1.7 Nanofluids

Nanofluids in micromixers are an emerging research area due to their enhanced heat transfer and mixing capabilities. Nanofluids—suspensions of nanoparticles (such as Al_2O_3, CuO, or TiO_2) in a base fluid (like water or ethylene glycol)—exhibit improved

thermal conductivity, viscosity, and surface properties. The concept of nanofluids was first introduced and developed in 1995 by Choi and Eastman (Eastman et al. 1996) at the Argonne National Laboratory, USA. The literature shows nanoparticles exhibit superior mechanical, optical, electrical, magnetic, and thermal properties, including a high surface area-to-volume ratio, enhanced thermal conductivity, and dimension-dependent physical characteristics.

A key advantage of using nanoparticles over microparticles is their ability to remain well-dispersed within the fluid, preventing issues such as channel blockage and erosion of channel walls. In contrast, microparticles tend to settle rapidly, leading to problems like abrasion, clogging, and increased pressure drops. However, nanoparticles tend to aggregate due to their high surface area and surface activity. To mitigate this, nanofluids often add surfactants to enhance stability and dispersion.

Hybrid nanofluids constitute an advanced category formed by dispersing two or more varieties of nanoparticles inside a single base fluid to attain enhanced thermophysical, optical, rheological, and morphological characteristics. They are anticipated to supplant traditional single-nanoparticle nanofluids owing to their broader absorption spectrum, diminished extinction coefficient, enhanced thermal conductivity, decreased pressure drop, and lower frictional losses and pumping power than mono nanofluids. Figure 1.1 shows the fundamental classification of nanoparticles based of the working media

Key feature of Nanofluids in Micromixers

i. Nanoparticles induce secondary flows and enhance chaotic advection, improving mixing performance in microchannels.
ii. Brownian motion and thermophoresis effects contribute to faster and more uniform mixing.
iii. Nanoparticles alter the rheological properties of the base fluid, affecting pressure drop and flow characteristics in micromixers.

The main challenges for nanofluids are

i. Stability and aggregation of nanoparticles over time.

ii. Potential clogging in microchannels.

iii. Increased viscosity affecting pumping power.

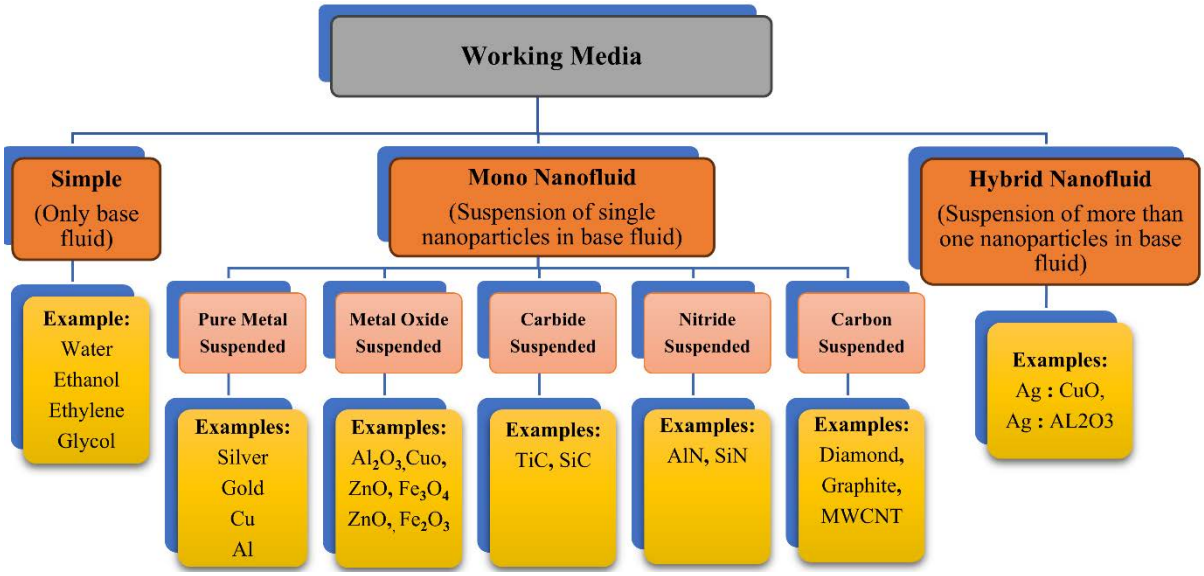

Figure 1.1 Classification of nanofluid (Bumataria, Chavda, and Panchal 2019)

1.8 Parameters Related to Micromixer

The following dimensionless parameters govern the flow dynamics in micromixers:

i. $\text{Reynolds Number} = \frac{UL}{\nu}$

ii. $\text{Peclet number} = \frac{UL}{D}$

iii. $\text{Schmidt number} = \frac{\nu}{D}$

A micromixer's characteristic length and velocity scales are denoted by the letters L and U. In contrast, the letters v and D represent the kinematic viscosity and the mass diffusivity coefficient, respectively.

The Reynolds number (Re) is a dimensionless quantity used in fluid mechanics to predict fluid flow regime in a pipe or over a surface. It helps determine whether the flow is laminar, turbulent, or transitional. The Peclet number (Pe) evaluates the predominance of convective mass transfer relative to diffusion, with convection

becoming prominent at elevated Peclet values. The Schmidt number (Sc) describes the ratio of momentum diffusivity (kinematic viscosity) to mass diffusivity. It is used in fluid dynamics and mass transfer problems.

1.9 Outline of the Thesis

The thesis begins with **Chapter 1: Introduction**, which provides an overview of fluid mixing in microfluidics, emphasizing its importance in various applications.

Chapter 2: Literature Review explores the literature available on principles of microfluidic mixing, the characteristics of Newtonian and non-Newtonian fluids, and different types of micromixers, including passive, active, and hybrid designs. It reviews the use of Computational Fluid Dynamics (CFD) in microfluidic analysis and identifies research gaps to formulate the objectives for the present study.

Chapter 3: Methodology presents the governing equations for fluid flow, including the Navier-Stokes, continuity, and momentum equations used in the present study. Additionally, it explains CFD methodologies and key performance metrics like the mixing index, pressure drop, and residence time distribution, and also details the computational approach, including the design of the 3D micromixer, numerical simulation setup, and mesh sensitivity analysis. It describes the simulation cases for both Newtonian and non-Newtonian fluids, outlining boundary conditions for the study.

Chapter 4: Results and Discussion analyzes the flow behaviour and mixing performance across different micromixer designs, and validates the strategies against bench data. The effects of flow rate, Reynolds number, and fluid rheology on mixing

efficiency have also been discussed. A comparative study of various micromixer configurations is presented, with insights into performance optimization.

Finally, **Chapter 5: Conclusions and Future Work** summarizes the key findings and contributions of the study. It discusses the limitations and practical implications of the research while providing recommendations for future investigations.

The thesis concludes with references and appendices containing supplementary data and computational details.

Chapter 2 LITERATURE REVIEW

Microfluidic devices may be categorized into two groups according on their stimulus: passive and active. Passive microfluidic systems operate without external actuators to manipulate fluids, direct particles inside the fluid, or facilitate separation. Active microfluidic systems utilize external energy sources for mixing and separation. The researchers use some equations to quantify the mixing quality. Table 2.1 provides an overview of these relationships, where Ci, C_o, $\bar{C}$ and C_∞ signify the concentration at a specific location, the concentration at a point within the non-mixing cross-section, the mean concentration, the mean concentration in the non-mixing cross-section, and the overall mixing concentration, respectively. In contrast, N and δ represent the quantity of nodes in the section and its breadth, respectively. Equation (2.1) (Tekin et al. 2011)calculates the mixing index using pixel intensities over a cross-section of channels. MI = 0.5 at the intake and zero after the fluids are entirely mixed. Equation (2.2) (Chen, Chen, and Liu 2020) better defines (Phan et al. 2015) the mixing index. The nondimensional mixing parameter in the following formula is calculated by assessing the ratio of the standard deviation to the mean intensity. This ratio is referred to by some researchers as the Mixing Index (MI) (Hashmi and Xu, 2014). 0 and 1 denote unmixed and thoroughly mixed states, respectively. When the mixing index is not dimensionalized, equation (2.2) applies. This is performed by linking the standard deviation and intensity in a non-mixing cross-section. The distinction between equation (2.3) (Phan et al. 2015) and equation (2.4) (Du et al. 2013)lies in the latter's foundation on the cumulative effect of point concentration and pixel intensities. Some of the mixing index empirical formulas used by researchers are as follows.

2.1 Passive Micromixers

Improving the molecular diffusion and chaotic advection of fluids in passive (static) micromixers improves the mixing grade of these devices. The chaotic advection and molecular diffusion of fluids can be enhanced by expanding the contact area between the fluids and shortening the mixing path (Nguyen and Wu 2005). Two-dimensional and three-dimensional passive micromixers are separated initially based on the micromixers' structural dimensions. It should be noted that manufacturing passive

micromixers in two dimensions using lithography is less complicated than producing micromixers in three dimensions. A lot of different architectures have been suggested for passive micromixers. Numerical and experimental investigations consider multi-lamination, parallel lamination, curved-channel, convergence-divergence-based, obstacle (or baffle) based and unsymmetrical features.

$$\eta = \left[\sum_{i=1}^{N} \frac{(C_i - \bar{C})^2}{N}\right]^2 \tag{2.1}$$

$$\eta = 1 - \left[\sum_{i=1}^{N} \frac{(C_i - \bar{C})^2}{N}\right]^2 \tag{2.2}$$

$$\eta = 1 - \frac{\left[\sum_{i=1}^{N} \frac{(C_i - \bar{C})^2}{N}\right]^2}{\left[\sum_{i=1}^{N} \frac{(C_0 - \overline{C_0})^2}{N}\right]^2} \tag{2.3}$$

$$\eta = 1 - \frac{\int_0^{\delta} |C_i - C_\infty| dy}{\int_0^{\delta} |C_0 - C_\infty| dy} \tag{2.4}$$

η is the mixing performance, and C is the concentration gradient defined at the inlet and outlet.

2.1.1 Lamination-based patterns

The micromixers that use parallel lamination are designed to segregate the incoming flows into two distinct sub-streams (as seen in T-type and Y-type mixers) or further divided into multiple sub-streams (in multi-lamination configurations) (Nguyen and Wu 2005). Various micromixer designs, including T-type and Y-type configurations, are widely recognized for their structure, which involves introducing two separate

streams into distinct channels. These streams then converge into a single straight channel. In such micromixers, mixing occurs primarily through molecular diffusion. As a result, achieving high mixing efficiency at low Reynolds numbers typically necessitates using two sequential microchannels. (Hessel et al. 2005) demonstrated the mixing length $L_m = P_e \times w$ for laminar flow, where w represents the width channel. Researchers generate secondary flows, swirling motions, and vortices, typically achieved under high Reynolds number conditions to enable rapid mixing in such micromixers. Such as, (Wong et al. 2004) employed a diamond-shaped step subsequent to the primary straight channel of a T-type micromixer constructed from silicone and glass to disrupt fluid flow, functioning within a Reynolds number from 400 to 500 (Figure 2.1a). (Gobby et al. 2001) examined the impact of inlet orientation in microchannel Y-mixers on mixing efficiency, revealing that the shortest mixing length is achieved by incorporating a throttle section at the start of the straight channels (Figure 2.1b).

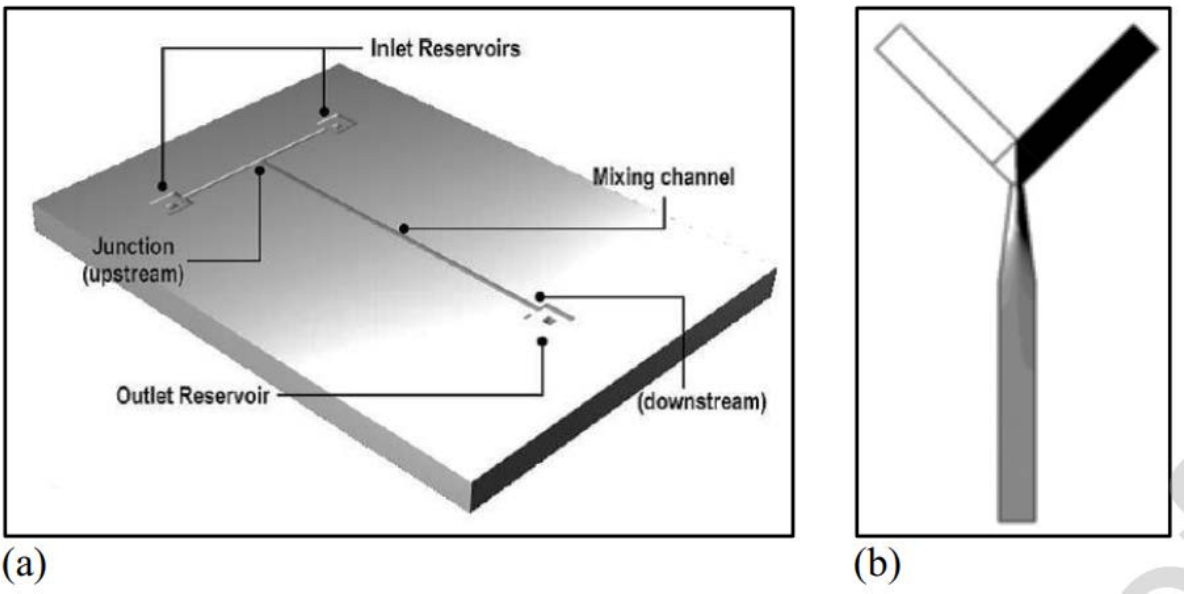

Figure 2.1 (a) Illustrations of T-type micromixer constructed from glass/silicon (Wong et al. 2004) and (b) methanol mass fraction distribution profiles in a venturi-style Y-mixer designed for the blending of oxygen and methanol (Gobby et al. 2001).

In contrast to the Y-type configuration, multi-lamination designs facilitate the mixing process by introducing fluids into the mixer through varied flow patterns. They include multiple flows (Bessoth et al. 1999), hydrodynamic focusing (Hessel et al.

2005; Löb et al. 2004), interdigitated mixing (Hardt & Schönfeld 2003; Hessel et al. 2003) and cyclone arrangements. Most of the multilaminate patterns have three dimensions (Branebjerg et al. 1996; Buchegger et al. 2011; Gray et al. 1999; Lim et al. 2011; Melin et al. 2004, 2004; Munson & Yager 2004; SadAbadi et al. 2013; Schwesinger et al. 1996; Walker 2004), the streams are combined both horizontally and vertically in successive stages. (Hong et al. 2004) a 2-D adapted Tesla design (Figure 2.2a) was proposed, constructed from olefin copolymer (cyclic) through thermoplastic. The Coanda effect improved the mixing efficiency of this micromixer through the chaotic advection. (Hossain et al. 2010) modified Tesla design was optimized by analyzing the relationship between the diffuser gap and channel width and the ratio of the curved gap to the channel width, focusing on Reynolds numbers in the $0.05 < Re < 40$ range. The authors (Yang et al. 2015) introduced a 3D Tesla configuration designed for cancer cell analysis applications (Figure 2.2b). Additionally, other three-dimensional designs, such as C-shaped structures, have been suggested for use in multi-lamination micromixers (Liu et al. 2000), H-C-shape (Viktorov et al. 2016), H-shape (Nimafar et al. 2012), L-shape (Vijayendran et al. 2003), etc. Table 2.1 summarises some of the lamination-based analyses of micromixers.

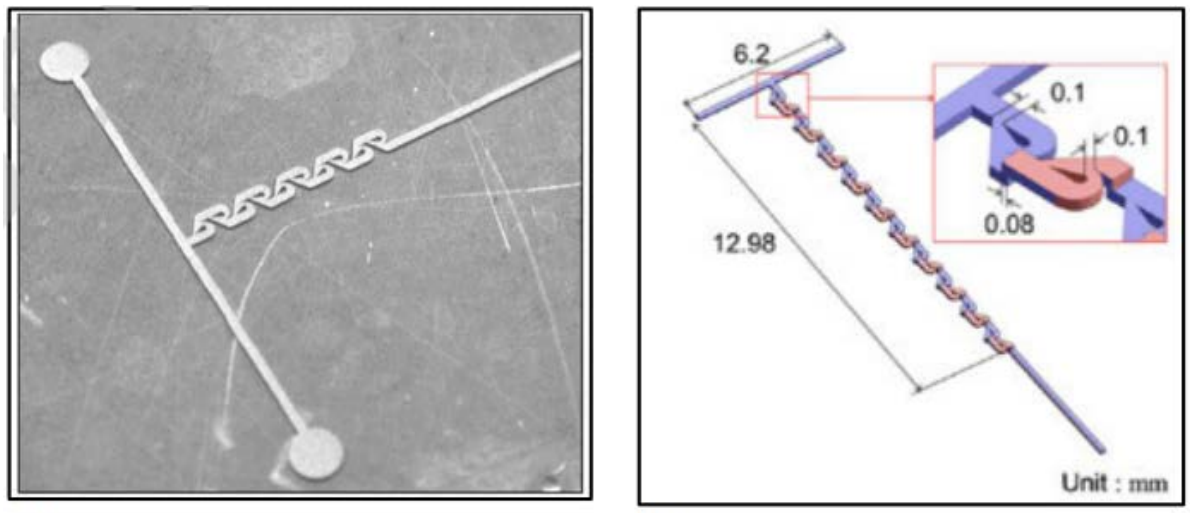

Figure 2.2 (a) Schematic of two-dimensional modified Tesla structure (Hong et al. 2004) and (b) three-dimensional Tesla structure (Yang et al. 2015).

Table 2.1 Lamination-based micromixers.

Characteristic/ mixing species	Re	Pe	Mixing Index	Material/ Method	Reference
Optimized zigzag microchannel	0.1-100	-	100%	Numerical Simulation	(Chen and Li 2017)
T-shape: simple and Serpentine/ distilled water and Rhodamine B	1-80	-	91%	PDMS	(Ansari et al. 2018)
Hybrid	0.001-45	-	100%	PDMS	(Bazaz et al. 2018)
T-shape / blue dye and a colourless liquid	500	$7x10^5$	83%	Silicon/Pyrex glass	(Wong et al. 2004)
Y-shape / oxygen and methanol	0.1	150	-	-	(Gobby et al. 2001)
Interdigital	0.07	60	95%	Glass	(Bessoth et al. 1999)
Interdigital / water blue and pure water	2-341	$6.41x10^3$ - $1.07x10^6$	-	Glass	(Hessel et al. 2003)
Star/dye liquid	108	-	-	Numerical Simulation	(Hardt and Schönfeld 2003)
(Walker, 2004) Split-join / M chloric acid +	18	-	-	Silicon	(Walker 2004)

methyl orange dissolved in water - oil + air - water + air					
Split-join / fluorescein dissolved into two different buffers	0.05	50	97%	Myler	(Munson and Yager 2004)
Multi-stream / dyed water	0.1	14	-	Silicon/ PDMS	(Melin et al. 2004)
Split-join / phenol- red and an acid	0.03-0.66	15-330	-	Silicon/glass	(Branebjerg et al. 1996)
Four-layer / D_2O and H_2O	-	-	90%	Silicon	(Buchegger et al. 2011)
Three-layer / red and green-coloured water	< 5.5	-	85%	Numerical simulation	(SadAbadi et al. 2013)
Crossing manifold / DI water and ethanol	-	-	90%	Numerical simulation	(Lim et al. 2011)
Modified 2D Tesla / dyed DI water	n/r	-	-	Cyclic Olefin Copolymer (COC)	(Hong et al. 2004)
Modified 2D Tesla / dyed DI water	0.05-40	-	70.2%	Numerical simulation	(Hossain et al. 2010)

3D Tesla / DI water and DI water a solution containing fluorescent dye	0.1-100	-	94%	PDMS	(Yang et al. 2015)
H-C-shape / Blue- and yellow-coloured food-grade water	1-100	-	93%	Polycarbonate	(Viktorov et al. 2016)
H-shape / coloured water solutions	0.08-4.16	-	98%	Plexiglas	(Nimafar et al. 2012)
Serpentine / dyed water and pure water	1-120	1×10^{4}-1.2×10^{6}	n/r	Numerical simulation	(Wasim Raza et al. 2018)
Serpentine / blue ink and yellow ink	0.1-100	-	> 95%	PMMA	(Lee et al. 2006)
T-shape / deionized water	100-500	-	~ 65%	PMMA	(Mariotti et al. 2019)

2.1.2 Obstacle (baffle-based patterns)

Introducing barriers in the microchannel induces chaotic advection and vortices, decreasing the mixing length, particularly in basic configurations like T- and Y-mixers. Numerous computational and experimental studies have employed various obstacle layouts to assess the mixing process. There are two categories of barriers: wall barriers and microchannel barriers. The fact that these designs are intimately connected to other configurations, such as spiral patterns and convergence-divergence patterns, should be considered.

Various obstacle arrays layout were studied by (Wang et al. 2002) Y-type micromixer (Figure 2.3a). Thus, obstacles can generate turbulence and disturb the liquid flows for high Reynolds numbers. It was further demonstrated that the most effective configuration aligns with the asymmetric arrangement. (Alam et al. 2014) determine the effectiveness of mixing water and ethanol, cylindrical obstacles were employed in a curved-channel micromixer that was working at Reynolds numbers ranging from 0.1 to 60. A comparison of different obstruction shapes revealed that micromixers with hexagonal and circular cross-sections demonstrate similar mixing performance. (Lin et al. 2003) additionally, cylindrical obstacles were incorporated into a microchannel to enhance mixing efficiency, particularly for operation at high Reynolds numbers, specifically within the $200 < Re < 2000$ range. (Bazaz et al. 2020) refined the configuration of four rectangular obstacles within a T-type micromixer (Figure 2.3b) for Reynolds numbers ranging from 0.1 to 60. Using the Taguchi method, they evaluated the effect of obstacle geometry and determined that obstacle height had a more significant impact on performance than width. (Bhagat et al. 2007) examined the influence of the shape and height of obstacles—specifically triangular, circular and smooth diamonds—on the mixing approach. Their findings indicated that increasing the obstruction heights enhances the mixing grade. Among the configurations studied, circular obstacles were shown to achieve a higher mixing index than the others. The obstacle designs explored included check mark, chevron, straight and arc geometries (Sadegh Cheri et al. 2013), leakage side-channels (Lee et al. 2006), triangle (Wang et al. 2014) and staggered grooves (Afzal & Kim 2014; Du et al. 2010; Hama et al. 2018; Whulanza et al. 2018; Yoshimura et al. 2019) have been introduced by researchers to achieve shorter mixing lengths and higher mixing efficiencies across a wide range of Re. To determine the efficiency of mixing, Sadeghcheri and colleagues deployed round-corner rectangular and hexagonal chambers. These chambers were equipped with four obstacles (Figure 2.3c) through numerical and experimental means. Their findings led them to conclude that the RCR chamber with straight obstacles had a more excellent mixing performance than other geometries they investigated. Various staggered grooves have also been investigated to achieve a more significant mixing of fluids in shorter microchannels. In a recent study, Hama and colleagues conducted a computational and experimental investigation of reverse-staggered herringbone micromixers (shown in Figure 2.3d)

for values of Re ranging from 1 to 100. Their findings demonstrated that the mixing efficiency remains independent of the Re and the diffusion coefficient within this range of Re. This suggests that, under these conditions, other factors—such as flow patterns, channel geometry, or secondary flow effects—play a more dominant role in determining mixing performance. The results indicate that, beyond a certain threshold, increasing the Reynolds number or altering the diffusion coefficient does not significantly enhance or hinder mixing, implying the presence of a regime where mixing dynamics are governed primarily by convective mechanisms rather than molecular diffusion or inertial effects.

Certain micromixers, including lamination-based, obstacle-based, and divergence-convergence-based designs, operate on the principles of split-and-recombine (SAR) or split-joint mechanisms (Bahei Islami & Ahmadi 2019; He et al. 2019). Both experimental and numerical analyses demonstrated that a D-shaped obstacle induced the formation of extended Dean flows and vortices, achieving a peak mixing efficiency of 95% at a Reynolds number of 80. (Islami and Ahmadi 2019) integrated passive mixing techniques (utilizing rectangular obstacles) with active mixing methods (employing oscillatory inlet velocity) to attain a maximum mixing efficiency of 98% at a Reynolds number of 0.156.

Obstacle-based micromixers are those with obstacles embedded in the walls (Hussain et al. 2019; Jain & Nandakumar 2010; Karthikeyan et al. 2018; Milotin & Lelea 2016; Tsai & Wu 2011). Micromixers with triangular and rectangular obstacles on the walls were utilized by Karthikeyan et al. to study and optimize the mixing quality of fluids with extremely low diffusivity (~ 10^{-12} m^2/s). This optimization was accomplished via the application of the ANOVA methodology.

They discovered that the mixing efficiency might reach one hundred per cent in the case of a quarter cross-section when Re equalled ninety-one. The Koch fractal snowflake pattern has recently been incorporated into micromixers with obstacles to enhance their mixing performance (S. Zhang et al. 2019). The authors (Chen et al. 2019) conducted research on a Koch fractal mixer that included a pattern of rounding corners. According to their research findings, the micromixer with rounded corners has a smaller pressure drop than the one with a secondary fractal design. This suggests

that smoother, curved channel geometries reduce flow resistance and energy dissipation, leading to more efficient fluid transport. In contrast, the secondary fractal structure introduces additional complexity, likely increasing flow disturbances and resistance, contributing to a higher pressure drop. These findings are significant for optimizing micromixer designs, as minimizing pressure loss can improve overall efficiency, reduce pumping power requirements, and enhance mixing performance without unnecessarily increasing operational costs. Table 2.2 summarises some of the obstacle-based micromixer analyses.

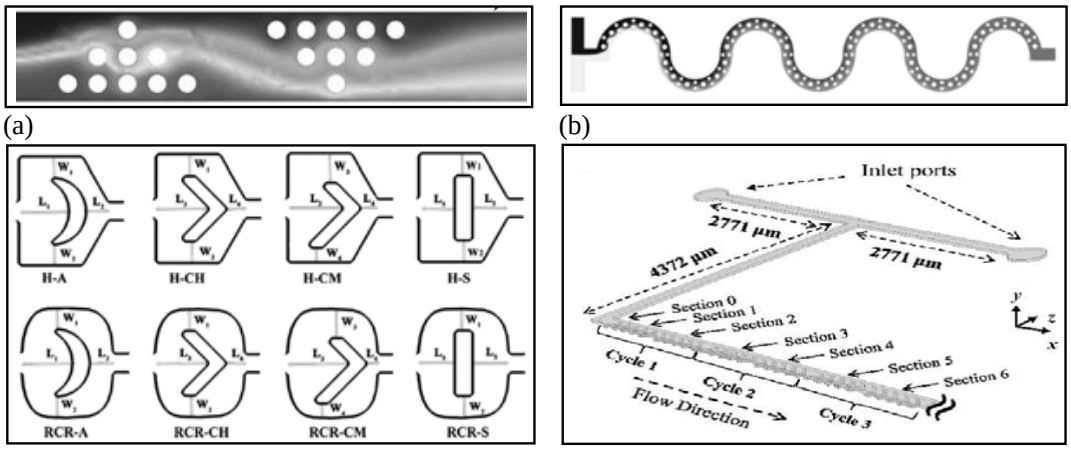

Figure 2.3 Diagram of obstacle-based micromixers with obstacles positioned within the channel: (a) cylindrical array (Wang et al. 2002), (b) cylindrical obstacles in a curved-channel mixer (Alam et al. 2014), (c) Round-corner rectangular (RCR) and hexagonal (H) chambers featuring chevron (CH), check mark (CM), arc (A), and straight (S) obstructions (Sadegh Cheri et al. 2013) and (d) reverse-staggered herringbone (Hama et al. 2018).

Table 2.2 Obstacle based micromixers

Characteristic	**Re**	**Pe**	**Mixing Index**	**Materials**	**References**
Circular obstacle array in channel	0.13-1333	100-10^6	55%	Computational	(Wang et al. 2002)
Circular and hexagonal	0.1-60	-	88%	Numerical simulation	(Alam et al. 2014)

obstacles in curved channel					
Cylindrical obstacle in channel	0.2	200	-	Glass/Silicon	(Lin et al. 2003)
Rectangular obstacle in channel	0.1-60	-	74.5%	Numerical simulation	(Bazaz et al. 2020)
Circular, triangular, diamond (smooth) and diamond (stepped) obstacles in channel	0.02-10	-	30%	PDMS	(Bhagat et al. 2007)
Chevron, check mark, arc, and straight obstacles in channel	0.1-40	-	99%	PDMS	(Sadegh Cheri et al. 2013)
Reverse-staggered herringbone in-channel	0.01-100	34.4-34400	-	PDMS	(Hama et al. 2018)
Triangular and rectangular obstacles on the wall	-	-	68%	Numerical simulation	(Karthikeyan et al. 2018)
Radial obstacles on	0.01-100	-	93%	PDMS	(Tsai and Wu 2011)

curved wall					
Half and quarter cross-section of circular obstacles on the wall	0.2-91	-	100%	Numerical simulation	(Milotin and Lelea 2016)
Koch fractal baffles on the wall	0.05-100	-	95%	Numerical simulation	(S. Zhang et al. 2019)
Rounded Koch fractal baffles on the wall	0.1-100	-	90%	Numerical simulation	(Chen et al. 2019)

2.1.3 Convergence-divergence patterns

These designs produce Expansion vortices if there is a rapid rise in the cross-sectional area. Since these vortices originate horizontally, the interfacial area between the fluids is increased, which results in improved mixing (Mondal et al. 2019). Consequently, the mixing grade is improved. It has been indicated before that convergence-divergence designs are commonly integrated with various configurations, such as obstacle-based, split-and-recombine (SAR), and curved-channel pattern designs (Afzal and Kim 2015, 2012; Arshad Afzal & Kwang-Yong Kim 2014; Chen & Li 2016; Chung & Shih 2007; He et al. 2019; Tran-Minh et al. 2014). Khosravi Parsa and Hormozi investigated the formation of Dean vortices and expansion vortices in micromixers characterized by convergent-divergent structures, specifically within the range of 0.2 to 75. Adjusting the phase shift among the sidewalls resulted in a convergent-divergent cross-sectional design, effectively enhancing mixing performance. The phase changes between $\pi/2$ and $3\pi/4$ brought about the highest possible mixing efficiency, which was determined to be 90%. Figure 2.4a evaluates the mixing efficacy of micromixers with two different topologies—raccoon and serpentine—in research performed by (Mondal et al. 2019). While the raccoon micromixer demonstrated superior mixing performance to the serpentine micromixer for specific Reynolds numbers and wavelengths, the results revealed that the mixing index improved with increasing wavelength for both designs. In a separate

investigation, Afzal and Kim explored various combinations of split-and-recombine (SAR) and convergence-divergence configurations for Reynolds numbers ranging from 10 to 70. Their findings indicated that the mixing index was markedly affected by the proportion of the throat length to the circumference of the circular wall in the micromixer, as seen in Figure 2.4b. Using ellipse-shaped micropillars, Tran-Minh and colleagues developed a micromixer that achieved a 90% efficiency rate for laminar blood mixing (Figure 2.4c). This micromixer was intended to induce the fluid to converge and diverge throughout the device. To enhance the mixing performance, Chen and Li utilized a topological micromixer (Figure 2.4d). This was accomplished by increasing the amount of chaotic advection. For the ranges of $0.1 < Re < 10$, the mixing efficiency was 95% and 85%. Therefore, the mixing efficiency was 95%. Table 2.3 shows convergence-divergence-based micromxers analyses.

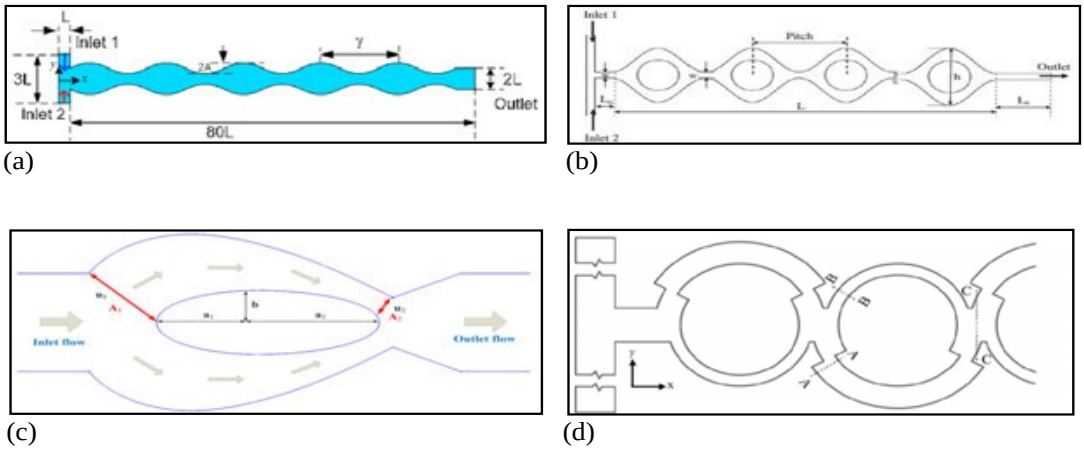

(a) (b)

(c) (d)

Figure 2.4 Illustration of convergence-divergence based micromixers: (a) serpentine (Zhang et al. 2019), (b) SAR and convergence-divergence (Arshad Afzal and Kwang-Yong Kim 2014), (c) ellipse-like micropillars (Tran-Minh et al. 2014), and (d) unbalanced SAR (Raza and Kim 2020).

Table 2.3 Convergence-divergence-based micromixers.

Characteristics	**Re**	**Mixing Index**	**Material**	**References**
Sinusoidal side walls	0.2-75	90%	Plexiglas	(Parsa and Hormozi 2014)
Raccoon and	0.1-100	~ 100%	Numerical	(Mondal et al.

serpentine			simulation	2019)
SAR and convergence-divergence	10-70	95%	Numerical simulation	(Afzal and Kim 2012)
SAR and convergence-divergence	10-70	95%	Numerical simulation	(Arshad Afzal and Kwang-Yong Kim 2014)
Ellipse-like micropillars	0.238-2.38	90%	Numerical simulation	(Tran-Minh et al. 2014)
Topological	Re < 0.1 and Re > 10 0.1-10	85% 95%	Numerical simulation	(Chen and Li 2016)
Rhombic	> 20	84%	PDMS	(Hossain and Kim 2014)
Unbalanced SAR	Re > 20	86%	PDMS	(Raza and Kim 2020)

2.1.4 Curved-channel pattern

One of the most notable qualities of curved micromixers is that they can function well even when the Reynolds number is high. The Dean number is a dimensionless metric that characterizes fluid flow in this specific type of micromixer (Hessel et al. 2005). subsequently, it was revealed that for De > 150, the secondary flow consists of two vortices, and for De < 150, it contains four vortices. (Cheng et al. 1976). High mixing efficiency requires multiple flow loops to enhance fluid interaction and dispersion. However, increasing the number of loops can lead to higher pressure drops and greater energy consumption, making it less practical for specific applications. To address this challenge, researchers have developed innovative designs that optimize mixing performance in curved-channel micromixers using a limited number of loops.

These advanced designs leverage chaotic advection, secondary flow generation, and strategically engineered curvature to enhance mixing without excessive looping. By carefully shaping the channel geometry, incorporating asymmetrical structures, or

introducing strategically placed obstacles, these designs effectively promote fluid stretching and folding, leading to rapid and efficient mixing. Such improvements are crucial for applications in microfluidics, lab-on-a-chip systems, and chemical or biomedical processing, where maintaining high efficiency while minimizing pressure loss and energy consumption is essential.

Moreover, as noted earlier, this design is frequently combined with other configurations, including obstacle-based and convergence-divergence structures, to improve overall performance (Afzal & Kim 2015; Arshad Afzal & Kwang-Yong Kim 2014; Chen & Li 2016; Chung & Shih 2007; Hossain & Kim 2014; Raza & Kim 2020; Tran-Minh et al. 2014). (Schönfeld and Hardt, 2004) introduced a 3-D micromixer composed of two curved square channels, leveraging different forms of Dean vortices to enhance mixing efficiency. (Jiang et al. 2004) was determined that the mixing process is influenced by the Dean number, depending on whether it is greater or less than 140. They developed a planar meander mixer, asserting that it can achieve chaotic mixing without relying on a multi-step process or complex three-dimensional structures. This approach simplifies fabrication, reduces manufacturing costs, and facilitates integration into lab-on-a-chip and microfluidic systems. Additionally, the absence of intricate 3D features minimizes potential pressure losses and operational challenges, making the design more practical for various applications, including chemical analysis, biomedical diagnostics, and point-of-care testing. They also claimed that chaotic mixing may be created without a multistep or three-dimensional framework-dimensional structure (Figure 2.5a). Spiral microchannels featuring multiple mixing sections connected through a central S-section were introduced by (Sudarsan & Ugaz 2006) (Figure 2.5b) who analyzed five spiral configurations within the Reynolds number range of 0.02 to 18, concluding that transverse Dean flows result in a mixing efficacy of 90%. (Harrson Santana et al. 2015) the design was used to mix ethanol and Jatropha curcas oil, revealing that spiral micromixers achieve a much higher mixing efficiency compared to T-type micromixers (Mehrdel et al. 2018, p. 3) revised the design by adding expansion and contraction sections (Figure 2.5c), achieving mixing efficiencies of 85% and 98.5% for one and three loops, respectively, with a 10% expansion at Re 1. Several designs inspired by spiral patterns, have been created to examine the influence of Dean vortices on the mixing efficiency of

micromixers. (Al-Halhouli et al. 2015; Balasubramaniam et al. 2017; Joshua Clark et al. 2018; Liu et al. 2015; Rafeie et al. 2017; Scherr et al. 2012; Sheu et al. 2012; Vanka et al. 2003; Yang et al. 2013). Table 2.4 summarises the curved-channel micromixers analyses.

Table 2.4 Curved-channel micromixers.

Characteristic	Re	Mixing Index	Materials	References
Double spiral	0.02-18.6	> 90%	SEBS	(Harrson Santana et al. 2015)
Double spiral with expansion and contraction	0.1-10	98.5%	PDMS	(Mehrdel et al. 2018)
Spiral and concentric circular	0.6	~ 40%	Aluminium	(Vanka et al. 2003)
Logarithmic spiral	1-70	86%	PDMS	(Scherr et al. 2012)
Tapered curved	1-100	88%	PDMS	(Sheu et al. 2012)
Two layers of spiral channels overlapped together	8-40	90%	Glass	(Yang et al. 2013)
Fine-threaded lemniscated-shaped	1-1000	> 90%	PDMS	(Rafeie et al. 2017)
Non-rectangular cross-section	1-100	~ 100%	Numerical simulation	(Joshua Clark et al. 2018)
Spiral, interlocking-	0.01-50	~ 100%	PDMS	(Al-Halhouli et al. 2015)

semicircle, Ω channel				
Double helical channel	0.003-30	99%	Numerical simulation	(Liu et al. 2015)
Square, semi-circle, trapezoid cross sections	20-277	> 90%	PDMS	(Balasubramaniam et al. 2017)

(Scherr et al. 2012) studied a micromixer with logarithmic-spiral-based experimentally using PDMS (Figure 2.5d). With a Re value of 67, they attained % mixing efficiency of 86%. As a result of the varying cross-sectional area, they revealed that logarithmic curvature creates Dean vortices in three dimensions inside the system. A micromixer incorporating staggered a semi-circular microchannel and 3-quarter ring-shaped microchannels was created by (Sheu et al. 2012) (Figure 2-5e). The authors concluded that the secondary flows are insignificant when the value of Re is less than five, but they are significant when the value of Re is fifty. Double-layered spiral microchannels were utilized by (Yang et al. 2013) (Figure 2.5f), (Rafeie et al. 2017) (Figure 2.5g) and (Joshua Clark et al. 2018) (Figure 2.5h) to design 3D micromixers. (Yang et al. 2013) exemplify that the mixing index improves as the channel height increases and that cylindrical geometry is more effective than cubic. (Rafeie et al. 2017) a fine-threaded lemniscate-shaped mixer was designed for the Reynolds number range of 1 to 1000, achieving a mixing efficiency greater than 90%. The non-rectangular micromixer design was studied by (Joshua Clark et al. 2018) to examine the influence on the Dean vortices in a spiral micromixer. Their suggested mixers demonstrated that complete mixing may be attained at a Reynolds number of twenty. However, achieving complete mixing at a Re value of one hundred in rectangular cross-section mixers is possible.

2.2 Active Micromixer

External energy inputs can improve mixing performance by expanding the interfacial area between fluids, disturbing their flow patterns, or generating chaotic advection. Pressure filed (Deshmukh et al. 2000; Du et al. 2013; Li and Kim, 2017; Niu & Lee,

2003; Oh et al. 2012; Wu et al. 2019; Xia & Zhong, 2013; Zhang et al. 2019), acoustic filed (Ahmed et al. 2009; Ang et al. 2016; Choi et al. 2009; Fu et al. 2017; Lim et al. 2019; Liu et al. 2002; Moroney et al. 1991; Orbay et al. 2017a; Qi et al. 2008; Wang et al. 2009; Yang et al. 2001; Yaralioglu et al. 2004), magnetic field (Ballard et al. 2016; Chen and Zhang, 2017; Ergin et al. 2015; Fu et al. 2010; Hejazian and Nguyen, 2017; Jeon et al. 2017; Kang and Choi, 2011; Kumar et al. 2019a; Lee et al. 2016; Liu et al. 2016; Nouri et al. 2017; Owen et al. 2016; Saroj et al. 2016; Veldurthi et al. 2015), electric field (Ahmadian Yazdi et al. 2015; Bhattacharyya and Bera, 2015; Choi et al. 2009; Daghighi et al. 2013; Deval et al. 2002; Ebrahimi et al. 2014; El Moctar et al. 2003; S. Kazemi et al. 2017; Z. Kazemi et al. 2017; Kim et al. n.d., 2018; Matsubara and Narumi, 2016; Peng and Li, 2015; Shamloo et al. 2016; Usefian et al. 2019, 2019; Usefian and Bayareh, 2019; Zhang et al. 2006, 2018; Zhao et al. 2017), thermal field (Bird 2002; Evans, Palhares Junior, and Oishi 2017; Gale et al. 2018; Huang et al. 2012; Huang and Tsou 2014; Kunti, Bhattacharya, and Chakraborty 2017a, 2017b, 2018; Mao, Yang, and Cremer 2002; Sasaki, Kitamori, and Kim 2012; Tsai and Lin 2002; Zhang et al. 2016) are some genre of external energy sources.

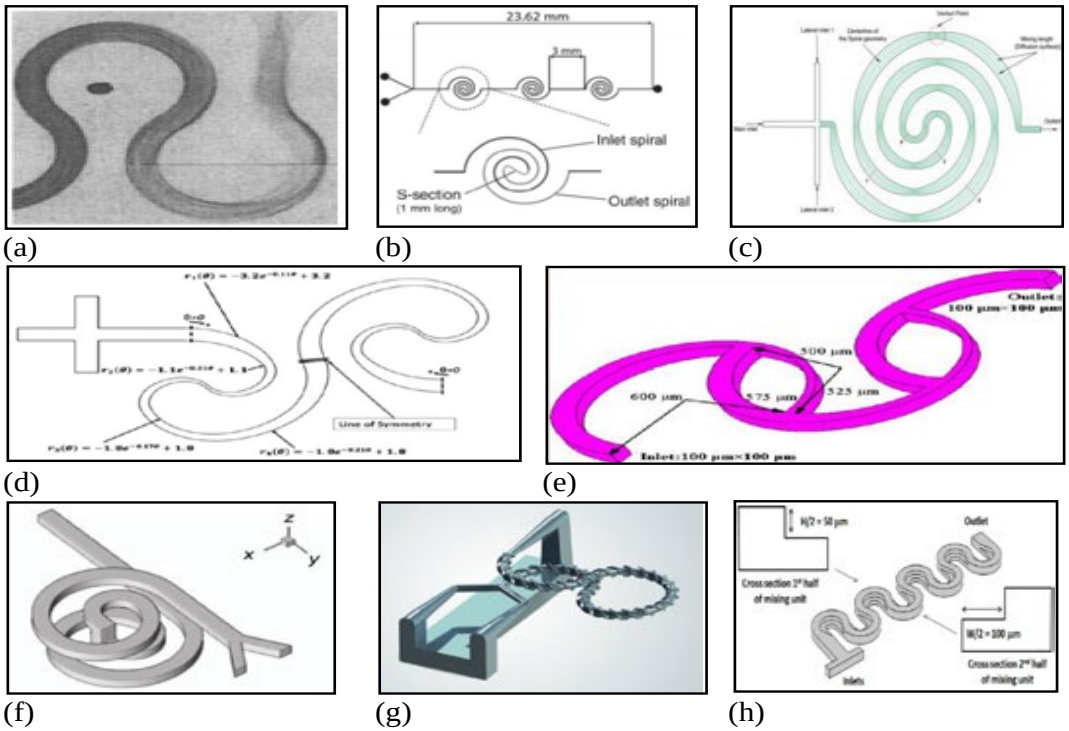

Figure 2.5 Illustration of curved-channel micromixers: (a) plan meander mixer (Jiang et al. 2004), (b) double spiral (Sudarsan and Ugaz, 2006), (c) double spiral with

expansion and contraction (Mehrdel et al. 2018), and (d) logarithmic spiral (Scherr et al. 2012)

2.2.1 Pressure-driven micromixer

Pressure-field-driven micromixers are microfluidic devices that use externally applied pressure fields to enhance fluid mixing at the microscale. The initial pressure-driven micromixer was developed by (Deshmukh et al. 2000) was a T-type micromixer. By simultaneously controlling and halting the flow in the channel, they were able to produce alternate fluid perturbation through the utilization of an integrated planar micropump. In essence, the step function was chosen to produce a pulsatile flow, necessitating multiple pulses to ensure the complete mixing of the fluids. Velocity oscillation has disrupted fluid flows and enhanced their interaction with the outer area (Du et al. 2013; Niu and Lee, 2003; Oh et al. 2012; Xia and Zhong, 2013). A pressure-driven micromixer was designed by (Niu and Lee, 2003) based on the principles of fluid stretching and folding. The Lyapunov exponent was employed to analyze the chaotic behaviour and enhance the optimization of the micromixer. The study revealed that oscillatory flow improves fluid stretching and folding, achieving a mixing efficiency of 97% after four mixing units, with a total flow velocity of 44 mL/min and an average viscosity of 8 mPa·s (Zhang et al. 2018). (Li and Kim, 2017) creating pulsatile pressure in the mixer unit was accomplished using a constant input of water head pressure. The micromixer they introduced achieved a mixing performance of approximately 90% at flow of 20 microliters per minute and within a frequency range of 14 to 20 hertz. The research investigated time-throbbed mixing for viscoelastic fluids and Newtonian in a T-mixer (Zhang et al. 2019). Table 2.5 summarises the pressure-driven micromixer analyses.

Table 2.5 Pressure-driven micromixers.

Characteristics	Re	Mixing Index	Materials	References
Pulsatile flow	2.4	-	SOI and quartz wafers	(Deshmukh et al. 2000)
Electric circuit	0.17	-	Analytical	(Oh et al. 2012)

methods			solution	
Planar mixing channel	83-250	90%	n/r	(Xia and Zhong, 2013)
Pulsatile micromixer	-	90%	PDMS	(Wu et al. 2019)
Oscillator and divergent chambers	-	97%	PMMA	(Li and Kim, 2017)
Time-pulsed flow	0.002-0.1	Newtonian: ~ 53% Viscoelastic: 82%	PDMS	(Zhang et al. 2019)

2.2.2 Acoustic field-driven micromixer

Micromixers utilize acoustically-driven microstreams, wherein air bubbles within a liquid are activated via an acoustic field (Liu et al. 2002). The study concentrated on utilizing an acoustic actuator to agitate liquids in a flexible plate-wave (FPW) system (Moroney et al. 1991). It was noted that using higher frequencies (> 50 Hz) increases fluid temperature, which can be detrimental to biological samples (Nguyen & Wu, 2005; Yang et al. 2001). In bubble-based acoustic micromixers, single (Liu et al. 2002) or many bubbles (Ahmed et al. 2009) can arise from various factors, utilising acoustic waves to form a horseshoe-shaped air bubble in a micromixer. The agitated trapped air bubble interrupts the channel's laminar flows, causing sound and quick mixing. They defined the mixing time as $t = \frac{dmix}{vavg}$, d_{mix} represents the distance between thoroughly mixed and unmixed regions, and v_{avg} denotes the average fluid velocity. It was concluded that the mixing time significantly decreases with increased air bubbles (Liu et al. 2002). The impact of exerted frequency (0.5–10 kHz) on the mixing index of a micromixer was investigated. The study reckoned that both frequencies between 0.5 kHz and 10 kHz have no impact on the mixing index (Wang et al. 2009). The mixing performance, however, depends highly on the frequencies used, which vary from 1.0 to 5.0 kHz. This frequency range caused one or more bubbles, disturbing the local flow field. Research demonstrates that the improvement of mixing performance is greatly affected by bubble production throughout the

frequency range of 1.0 to 5.0 kHz. Bubbles did not develop in the microchannel beyond this frequency range. A bubble-driven acoustic micromixer featuring three inlets was developed, with nitrogen introduced via the central inlet to generate bubbles within the mixer (Orbay et al. 2017b). Table 2.6 summarises the acoustic field-driven micomixers analyses.

Table 2.6 Acoustic field-driven micromixers.

Characteristics	**Re**	**Frequency**	**Mixing Index**	**Material**	**References**
Bubble vibration	-	5	91%	PZT	(Liu et al. 2002)
Single-bubbled based	-	70-100	-	PDMS	(Ahmed et al. 2009)
Multi-bubbled based	-	1-5	-	PMMA	(Wang et al. 2009)
Multi-bubbled based	~ 0.01	1-5	93%	PDMS	(Orbay et al. 2017b)
Ultrasonic vibration	60	0-100	-	Glass	(Yaralioglu et al. 2004)
Surface-acoustic-wave-driven	3.1-15.4	1300	88%	PDMS	(Choi et al. 2009)

The other types of acoustic micromixers involve ultrasonic transducers (Jang et al. 2005; Yaralioglu et al. 2004), thin-film piezoelectric devices (Fu et al. 2017; Yang et al. 2001) and surface acoustic wave ones (Ang et al. 2016; Qi et al. 2008). A piezoelectric lead-zirconate generated the ultrasonic vibration--titanate (PZT) ceramic. In contrast to many researchers who employed planar piezoelectric transducers with flat surface (Choi et al. 2009), (Lim et al. 2019) analyzed the characteristics of concave and convex surface architecture. The research findings indicate that convex geometry yields enhanced mixing characteristics compared to flat and concave geometry.

2.2.3 Magnetic field-driven micromixers

Magnetic field-driven micromixers are microfluidic devices that utilize external magnetic fields to induce fluid mixing at the microscale. These mixers are handy in lab-on-a-chip (LOC) applications, biomedical diagnostics, and chemical synthesis, where efficient mixing of small fluid volumes is crucial. Magnetic micromixers rely on magnetic forces to create flow disturbances, enhancing mixing in an otherwise low-Reynolds-number regime (where laminar flow dominates and diffusion alone is inefficient). They achieve this by magnetic beads/nanoparticles, magnetic stirring, and Magneto-hydrodynamic. Micromixers operate through magnetic drive mechanisms utilizing permanent magnets (Ballard et al. 2016; Hejazian & Nguyen, 2017; Kumar et al. 2019a; Lee et al. 2016; Nouri et al. 2017), electromagnet (Bayareh et al. 2018; Boroun, 2016; Ergin et al. 2015; Fu et al. 2010; Kang et al. n.d.; Liu et al. 2016)], micro stirrer (Chen et al. 2014; Kang et al. n.d., n.d.; Owen et al. 2016; Veldurthi, 2015) and integrated electrodes (Jeon et al. 2017; Kang & Choi, 2011). As part of this review, magnetically actuated micromixers were analyzed, incorporating studies published in recent years (Chen & Zhang 2017). A permanent magnet (Ballard et al. 2016) was used to rotate above a micromixer, while magnetic microbeads orbiting around iron-nickel alloy discs were placed on the base (Nouri et al. 2017). A permanent magnet was utilized to investigate the mixing behaviour of ferrofluid, consisting of DI water and Fe_3O_4, within a Y-shaped mixer featuring a rectangular cross-section. A non-uniform magnetic field produced by a permanent magnet in a straight microchannel was employed to evaluate the mixing of diluted ferrofluid with a non-magnetic fluid (Hejazian & Nguyen 2017). A numerical model was developed to simulate the improvement in mass transfer resulting from an irregular magnetic field. The results showed that mass transfer improves with both the magnetic field's strength and the magnetic particles' size (Kumar et al. 2019b). (Fu et al. 2010) study focused on the mixing process of deionized water and ferrofluid within a micromixer, utilizing an electro-magnet activated by a DC electric field. This investigation incorporated both numerical simulations and experimental methodologies. (Ergin et al. 2015) employed the micro-PIV technique to analyse transient flow fields during the mixing operation. Furthermore, it presented an innovative magnetic micromixer incorporating features of a flexible artificial cilium constructed from iron-doped

PDMS (Liu et al. 2016). Cilia-based micromixers reached a mixing efficiency of 80% under 200 G magnetic field strength. In an alternative arrangement, four electromagnets positioned in opposition were used in the micromixer to amalgamate deionized water and Rhodamine dye (Saroj et al. 2016). They identified a critical actuation frequency beyond which the degree of mixing declines as the actuation frequency increases. The mixing index of a T-mixer was investigated under oscillating, static, and rotating magnetic fields for Reynolds numbers ranging from 10 to 200. (Boroun 2016). They found that rotating magnetic fields resulted in superior mixing performance to static and oscillating magnetic fields.

Moreover, artificial cilia's symmetric and asymmetric motion was examined (Chen et al. 2014) to improve fluid mixing and demonstrated that mixing through asymmetric motion is 1.35 times quicker than mixing through symmetric motion. (Veldurthi 2015) positioned a micro-rotor within a chamber to achieve optimal mixing quality. The micromixer was fabricated using PDMS, and the magnetic actuator was created by dispersing magnetic nanoparticles in PCM, obtaining an efficiency of up to 90%. An organized arrangement of magnetic microbeads was employed to enhance fluid mixing within a microchannel. A more extended array of beads yields an increased mixing index (Owen et al. 2016). A micropump was designed and constructed for mixing at low Reynolds numbers. The findings indicate that electrodes of varying lengths provide superior mixing performance compared to uniform-length electrodes (Kang and Choi 2011). (Hejazian and Nguyen 2017) evaluated how electrode shape, configuration, and applied voltage influence the blending of a reagent with a phosphate-buffered solution. Table 2.7 summarises the magnetic field driven micomixer analyses.

Table 2.7 Magnetic field-driven micromixers.

Characteristics	**Re**	**Magnetic field Strength (G)**	**Mixing Index**	**Material**	**References**
A permanent magnet rotating over a micromixer with magnetic	<< 1	-	70%	PDMS	(Ballard et al. 2016)

microbeads					
Permanent parallel magnet	-	1280-3000	90%	Plexiglas	(Nouri et al. 2017)
Permanent parallel magnet	-	1750-2500	88%	PDMS	(Hejazian and Nguyen, 2017)
Electromagnet	0.004 and 0.02	200	> 95%	-	(Fu et al. 2010)
Electromagnet	-	2200	80%	Fe doped PDMS	(Liu et al. 2016)
Electromagnet	-	4200 and 6000	80%	Polystyrene	(Saroj et al. 2016)
Static, oscillating and rotating electromagnet	10-200	0-90 kA/m	~ 53%	Glass	(Boroun, 2016)
Electromagnet	5-50	-	96%	Numerical simulation	(Bayareh et al. 2018)
Asymmetric actuation of artificial cilia	4.64×10^{-3}	-	100%	PDMS	(Chen et al. 2014)
Cylindrical chamber with micro-rotor	0-40	-	90%	PDMS	(Veldurthi, 2015)
Array of rotating magnetic microbeads	-	-	~ 72%	NiFe	(Owen et al. 2016)
Integrated electrodes	-	-	27.8%	PDMS	(Kang and Choi, 2011)
Integrated	-	-	100%	Numerical	(Jeon et al.

electrodes	simulation	2017)

2.2.4 Electric-field-driven micromixers

Electric field-driven micromixers are microfluidic devices that use electric fields to enhance mixing in microchannels. These mixers exploit electrokinetic phenomena such as electroosmosis, electrophoresis, and di-electrophoresis to induce chaotic advection and improve mixing efficiency at small scales, where diffusion alone is often insufficient Electrohydrodynamic disturbance (El Moctar et al. 2003; Huang et al. n.d.; Kim et al. 2018). Moreover, electrokinetic instability (Daghighi et al. 2013; Daghighi & Li 2013; S. Kazemi et al. 2017) are used in electrical field-driven micromixers. EHD instability-based micromixers are equipped with electric fields that charge the fluids. These electric fields include direct current (DC) and alternating current (AC). The highly charged fluids disrupt the interface, which ultimately results in an improvement in the mixing index of micromixers. (El Moctar et al. 2003) suggested the T-type micromixer. This micromixer applied A perpendicular electric field across the fluid interface, generating secondary flow. This phenomenon was seen in the micromixer. In less than 0.1 seconds, they produced a satisfactory mixing by utilizing alternating direct current (DC) and current (AC) electric fields at a rate of 0.0174. (Huang, Lin, and Yang 2005) investigated the potential of a Y-mixer incorporating a group of slanted electrodes placed at the channel's base.

EKI mixing methods include electroosmosis, electrophoresis (Daghighi et al. 2013, 2013; S. Kazemi et al. 2017) and dielectrophoretic (Choi et al. 2009; Deval et al. 2002; Kim et al. n.d.). (Zhang et al. 2006) performed numerical and analytical investigations on mixing electroosmotic flow within microchannels characterized by heterogeneous zeta potential. The study demonstrated that heterogeneous zeta potential results in symmetrical secondary flows and asymmetrical rolls, contributing to an increased fluid mixing rate. The authors (Ebrahimi et al. 2014) studied a T-type microchannel to evaluate the effects of a non-uniform DC electric field on mixing and heat transfer in four distinct ribbed channel configurations. They (Bhattacharyya and Bera 2015) improved vertical flow was observed in an electroosmosis pressure-driven microchannel featuring a rectangular block.

This enhancement is attributed to the surface potential difference between the block and the microchannel wall. (Ahmadian Yazdi et al. 2015) studied Y-micromixer at high zeta potential influence for ionic size diffusion conditions. They discovered that the mixing length decreases as ionic concentration increases, provided the zeta potential is sufficiently high. (Shamloo et al. 2016) explored the mechanism of chaotic mixing by employing a charged electrode with an alternate current electric field. They examined various configurations, including one-ring, two-ring, and diamond types. They concluded that the diamond configuration achieved the highest mixing index, close to 99.8%, outperforming the one and two-ring designs.

An electro-osmotic micromixer was introduced, characterized by a staggered arrangement of electrodes powered by an alternating current (AC). This design operates effectively for Reynolds numbers (Re) ranging from 0.005 to 1.0, demonstrating the formation of a core vortex between the electrode pairs (Matsubara & Narumi, 2016). The mixing efficacy of an electro-osmotic micromixer was evaluated by positioning an electrically conductive flap at the entrance of the main channel (Z. Kazemi et al. 2017). (Zhang et al. 2018) incorporated asymmetrical planar floating electrodes into a T-mixer to generate asymmetrical vortices. While using a mixing length of 3.2 millimeters and a frequency of 400 hertz, they achieved a mixing quality of 94.7%. (Usefian and Bayareh, 2019) introduced a new electroosmotic micromixer operating under both AC and DC electric fields. Their findings revealed that vortices produced by the DC electric field are more intense than those created by the AC electric field. It was proved that increasing the voltage of both the alternating and direct current electric fields increases the mixing index.

Electrophoresis is the movement of conductive or non-conductive particles in an electrolyte solution caused by applying an external electric field (Daghighi and Li, 2013). (Daghighi et al. 2013) conducted an experimental analysis of the vortex generated for the conductive and non-conductive fragments under an exerted electric field. The formation of vortices and flow circulations for a conductive particle was analyzed during the mixing process in a micromixer with a rectangular chamber microchannel (S. Kazemi et al. 2017). They demonstrated that the outlet mass flow rate increases with a heightened electric field for a specific zeta potential, resulting in diminished mixing efficacy.

Di-electrophoresis refers to the accessibility of neutral particles caused by an alternating current electric field. This process causes particles to become asymmetrically polarized. When particles are exposed to a dipole moment, a force is created that forces them to migrate away from or about the electrodes. (Deval et al. 2002) introduced a di-electrophoretic micromixer designed to generate chaotic motion for the particles, demonstrating a significant reduction in mixing time. The author (Kim et al. n.d.) introduced a novel micro/nano mixer utilizing the dielectrophoretic approach. They demonstrated that the mixing quality increases as the channel depth decreases. Nevertheless, the channel depth must exceed roughly 20 micrometres. Table 2.8 summarises the electric field driven micromixers analyses.

Table 2.8 Electric-field driven micromixers.

Characteristics	**Re**	**Frequency**	**Mixing Index**	**Materials**	**References**
EHD (perpendicular electrode array)	0.0174	0.5-100	~ 81%	Lexan	(El Moctar et al. 2003)
EHD (inclined electrode array)	-	1000	94%	-	(Huang et al. n.d.)
Electroosmosis-pressure-driven	10	-	71%	Numerical simulation	(Peng and Li, 2015)
Electroosmosis mixing at high zeta potentials	-	-	99.5%	Numerical simulation	(Ahmadian Yazdi et al. 2015)
Electroosmosis mixing in a diamond type mixer	-	2-16	99.8%	Numerical simulation	(Shamloo et al. 2016)
Electroosmotic micromixer with a staggered array of electrodes	0.005-1.0	0.2-2 (dimensionless frequency	~ 98%	Numerical simulation	(Matsubara and Narumi, 2016)

		)			
Electroosmotic micromixer with a throat	-	-	51.5%	Numerical simulation	(Z. Kazemi et al. 2017)
Electroosmotic micromixer with rotating inner obstacle	-	-	~ 98%	Numerical simulation	(Usefian et al. 2019)
Turbulent-like electroosmotic mixer	< 1	1-10000	-	Transparent acrylic	(Zhao et al. 2017)
Planar floating-electrodes in a T-mixer	-	400	94.7%	Glass	(Zhang et al. 2018)
Electroosmotic micromixer with two electrodes in a chamber	-	0.5-4	~ 96%	PDMS	(Usefian and Bayareh, 2019)
Electrophoretic micromixer with a cylindrical chamber	-	-	100%	Numerical simulation	(Daghighi and Li, 2013)
Electrophoretic micromixer with rectangular chamber	-	-	99.5%	Numerical simulation	(S. Kazemi et al. 2017)

2.2.5 Thermal-field driven micromixers

Thermal field-driven micromixers are microfluidic devices that utilize temperature gradients to enhance mixing at the microscale. Unlike passive micromixers that rely on geometric structures or active micromixers that use external forces (such as electric

or magnetic fields), thermal field-driven micromixers exploit temperature-induced phenomena like thermophoresis, convection, bubble-induced, and viscosity variation. Thermal energy can enhance the mixing index of micromixers by enhancing the diffusion (Mao et al. 2002), employing thermal bubbles (Huang and Tsou, 2014, 2014; Tan, 2019) or using electrothermal effects (Huang et al. 2012; Kunti et al. 2018, 2017; Meng et al. 2018; Sasaki et al. 2012; Zhang et al. 2016). A thermal bubble-based micromixer was implemented using a micropump and microvalve. It was found that larger thermal bubbles result in greater mixing efficiency (Huang & Tsou, 2014). The simulation involved using a Y-mixer equipped with an integrated micro heater to combine a dye solution with distilled water (Tan, 2019).

Thermal bubbles act as micropumps and are responsible for driving the streams on their own. When the microheater is inserted asymmetrically, the author discovered that this results in the generation of an asymmetric vortex and secondary flow, increasing the mixing rate. When the microheater was positioned at the channel intake, it was possible to obtain a mixing efficacy of up to 95.6%. (Zhang et al. 2016) used AC electro-thermal flow to improve the mixing of two laminar streams. The microchannel was equipped with two asymmetric planar electrodes installed along its length, and a thin film resistive was positioned underneath the electrodes. The microchannel was fitted with two asymmetric planar electrodes along its length, with a thin-film resistor placed beneath them. It was demonstrated that the temperature gradient, generated by externally increasing the temperature, induces fluid stretching and folding, ultimately enhancing mixing potency.

Electro-thermal actuated micromixers were explored by (Kunti et al. 2018, 2017) integrated passive micromixer characteristics by adding grooves with electro-thermal micromixer advantages by placing a couple of asymmetric electrodes at the walls. (Meng et al. 2018) leveraged the advantages of AC electro-thermal effects to develop a micromixer for applications in microfluidics. Table 2.9 summarises the thermal field-driven micromixer analyses.

Table 2.9 Thermal-field driven micromixers.

Characteristics	Flow Rate (µl/s)	Mixing Index	Material	References
Thermal-bubble actuated micromixer	4.5	-	SOI	(Huang and Tsou, 2014)
Electrothermal micromixer	0.214	95.6%	Numerical simulation	(Tan, 2019)
Electrothermal micromixer	-	83.6%	Numerical simulation	(Zhang et al. 2016)
Electrothermal micromixer	29.9	97.25%	Numerical simulation	(Kunti et al. 2017)
Electrothermal micromixer	Inlet velocity 40 µm/s	~ 100%	PDMS	(Meng et al. 2018)

2.3 Nanofluids

Nanofluids are a unique type of heat transfer fluids that are produced by dispersing nanoparticles that are either metallic or non-metallic and have a high thermal conductivity into traditional fluids such as water, ethylene glycol, or oils. These nanoparticles, typically ranging from 1 to 100 nanometers, enhance the thermal properties of the base fluid, improving its ability to transfer heat efficiently. This makes nanofluids useful for heat exchangers, cooling systems, and other thermal management technologies. Table 2.10 shows various nanoparticles' thermo-physical properties and their cost analysis.

Over the past several years, nanofluids, which are two-phase systems consisting of a base fluid and nanoparticles suspended in the fluid, have garnered substantial attention in the fields of biomedicine and industry. (Rudyak, Pryazhnikov, and Minakov 2024). Their widespread use includes separating blood components, targeted drug delivery, and cooling microdevices (Matouq et al. 2024). In particular, nanofluids are

considered highly promising for thermal management in advanced electronic and biomedical systems due to their enhanced heat transfer properties.

One of the key aspects of these applications is the need for adequate mixing, which is essential for ensuring uniform distribution of nanoparticles, improving process efficiency, and optimizing performance. However, designing efficient mixing microdevices presents unique. Table 2.11 summaries the nanofluid analysis on hydro-thermal performanes.

Table 2.10 Thermal-physical properties of nanoparticles and their cost analysis challenges.

Nanoparticles	**ρ ($kg.m^{-3}$)**	**C_p ($J.kg^{-1}K^{-1}$)**	**K ($W.m^{-2}k^{-1}$)**	**Quantity(g)**	**Cost (Rs)**
CuO	6510	540	76	5	3111
Al_2O_3	3880	729	42.3	25	2000
TiO_2	4175	692	8.5	100	12859
SnO_2	2220	745	36	25	1500
ZnO	5610	494	29	100	1500
Fe_3O_4	4950	640	7	25	1750
Ag	10500	230	424	5	12917
Au	19300	129	315	1	35029
CNT	1350	3900	3000-6000	250	19521

Table 2.11 Hybrid- nanofluids on hydro-thermal performance

Fluid Base	**Nanoparticles**	**Concentration**	**Remarks**	**References**
Distilled Water	Al2O3, CuO, SiO2 and ZnO	1-5 %	The volume fraction of particles increases, viscosity also increases. However, as temperature rises, viscosity decreases. Nanoparticles' shape	(Alawi et al. 2018)

			significantly influences thermal conductivity (k) and viscosity.	
Water	TiO2	0.2 %	Models have been used to analyze the thermophysical properties, including viscosity, specific heat, and thermal conductivity. It was found that at very low concentrations, these properties have minimal impact on the heat transfer coefficient of nanofluids.	
Water	Zn and Fe2O4	0.02-0.5 %	The heat transfer coefficient and thermal conductivity increased by 42.99% and 11.8%, respectively, at a 0.5 weight concentration of Zn ferrite nanofluids.	(Gupta, Singh, and Said 2020)
Deionized Water and EG	Al2O3 and CuO	0.05-0.75 %	Deionized water (DW) is used as the host fluid to decrease viscosity while enhancing electrical conductivity.	(Giwa et al. 2021)
Water	ZnFe2O4, MnFe2O4, NiFe2O4	-	Ternary nanoparticle-based heat transfer liquids offer better thermal dispersion in	(Goud et al. 2022)

	fins than mono nanofluids, with their temperature gradient affected by the wetting parameter of the ternary hybrid nanofluid.	

Given these devices' minimal dimensions of microchannels, fluid flow is typically laminar, meaning that mixing occurs primarily through molecular diffusion rather than turbulence. This reliance on diffusion alone often results in insufficient mixing rates due to the inherently low diffusion coefficients of nanoparticles in the fluid.

Researchers and engineers are actively developing innovative micro-mixing strategies to address these limitations. These include chaotic advection, passive and active micromixers, and external forces like electric or magnetic fields to enhance nanoparticle dispersion. Advancements in microfluidic technology and nanofluid engineering continue to drive improvements in mixing efficiency, ultimately leading to better performance in biomedical diagnostics, targeted drug therapies, and next-generation cooling systems for electronic devices.

2.4 Summary of Literature Review

A set of characteristic nondimensional numbers determines the working conditions of passive and active micromixers. These numbers include the Re, the Pe, the Sr, the Fr, and the Kn. The molecular-diffusion process is responsible for mixing, which takes place because viscous effects predominate on the microscale. Because of this, passive micromixers require either substantial channel lengths or intricate design, which results in a significant pressure loss along the mixer. The ratio, represented as $\eta/\Delta p$, must be found between the mixing index and the pressure drop. The residence time (tr) of a rapid flow, also known as a high Reynolds number flow, is relatively brief. To fulfill the requirements, the disturbance frequency must be increased for active micromixers, while for passive micromixers, the channel length must be extended or the characteristic length reduced. When viscoelastic fluids are mixed in microchannels, the viscous and elastic effects impact the mixing process. It has been

discovered that more acute and smaller geometries might increase the instability of chaotic flow, ultimately resulting in more outstanding mixing effectiveness. The dimensionless Deborah number is utilized to quantify the mixing of viscoelastic fluid streams. This number is the ratio of the forces generated by elastic and viscous forces. By increasing the Deborah number, the elastic force can reduce the flow instability at the contact.

During numerical simulations, numerical diffusion errors significantly influence the accuracy of quantifying the mixing index. These errors arise due to the inherent approximations in discretization schemes and can lead to artificial smearing of scalar fields, reducing the precision of mixing measurements. As a result, the computed mixing index may not accurately reflect the accurate physical mixing process but be affected by the extent of numerical diffusion. This dependency underscores the importance of selecting appropriate numerical methods and resolution strategies to minimize diffusion artefacts and ensure reliable simulation outcomes. The formation of spurious diffusion in numerical simulations is highly impacted by the types of grid and discretization methods considered. In order to acquire a correct mixing index, information regarding the numerical diffusion error must be submitted. This is especially true for three-dimensional micromixers. During the numerical research of micromixers, the time-dependent method is another significant issue that has to be addressed. When assessing the mixing performance of micromixers, most numerical simulations have relied on steady-state approaches, with limited consideration given to time-dependent schemes. The mixing period is a key characteristic parameter of micromixers; hence, time-dependent simulations are necessary, mainly to confirm the findings of experiments.

Several different manufacturing methods and various materials have been utilized to produce micromixers. The evaluation of the mixing process or particle separation for biomedical devices is an everyday use of soft lithography in university microfluidic labs nowadays. This technique makes use of polydimethylsiloxane (PDMS). PDMS is combined with carbon nanotubes or solid nanoparticles to achieve a range of thermal and electrical conductivities. During the molding process, nanoparticles can be dispersed throughout the polydimethyl sulfide (PDMS) to adjust the hydrophobic-hydrophilic characteristics of the material. The 3D printing technique is inexpensive

for fabricating micromixers compared to moulding. Since the fabrication process is machine-controlled, this technology is more efficient, cost-effective, and faster than traditional lithography, making it a viable option for commercial applications. However, while 3D printing provides speed and affordability, PDMS-based products still achieve higher resolution and finer structural details, making them preferable for applications requiring precision (Gale et al. 2018). In addition, the technology of 3D printing is currently struggling to overcome the issue of fabricating chips made of many materials.

2.5 Research Gaps

Numerous researchers have explored various micromixer geometries, including T-junction microchannels, O-type micromixers, H-type micromixers, spiral micromixers, curved microchannels, square wave microchannels, zigzag microchannels, teardrop micromixers, chain-1 micromixers, Y-junction micromixers, multi-wave micromixers, tree-shaped micromixers, and more. The primary objectives of these studies are to achieve an optimal mixing index and minimize pressure drop across a range of Reynolds numbers.

Additionally, numerical analyses have examined the influence of several parameters, such as fluid properties, inlet velocities, microchannel cross-sectional dimensions, diffusion coefficients, and mixing angles, on mixing performance. Various studies have also plotted relationships such as Reynolds number vs. inlet velocity, Peclet number vs. mean inlet velocity, mixing length vs. inlet velocity, and mass fraction distributions at different sections of the mixing channel.

Obstacle-based passive micromixers have also been proposed, incorporating structural elements such as cylindrical, square, rectangular, and triangular obstacles and microchannels with patterned grooves. Simulation results indicate that mixing efficiency improves with an increased number of obstacles.

Despite extensive research, several gaps remain in the literature:

i. Limited studies have focused on T-micromixers with bent and twist mixing channels and offset insertions in T-mixers with bend geometries.

ii. Research on helical-spiral microchannels is relatively scarce.

iii. Limited studies on the influence of nanofluid in the micromixer performance

2.6 Research Objectives

The objectives of the research are described below:

i. Numerical analysis of mixing in different microchannel models (such as twist and bend, helical spiral micromixer models).

ii. Study of parameters that affect mixing, like inlet velocity and mixing angle (in TBM and HSTM).

iii. Comparative study of Newtonian and non-Newtonian fluid in micromixer.

iv. To investigate mixing index variation with nanoparticles.

Chapter 3 METHODOLOGY

This chapter establishes the fundamental principles governing fluid flow and mixing in 3D micromixers, focusing on both Newtonian and non-Newtonian fluids. The study begins with the selection of micromixer geometries, including T-shaped, serpentine, and herringbone designs, followed by defining channel dimensions, inlet/outlet configurations, and boundary conditions. A structured meshing approach is employed, with a grid independence study to ensure numerical accuracy. The governing equations, including the Navier-Stokes and continuity equations, are implemented to describe fluid flow, while viscosity models such as Power-law and Carreau are used to characterize non-Newtonian fluid behaviour. Mixing performance is evaluated using key metrics like the mixing index and pressure drop.

Computational Fluid Dynamics (CFD) simulations are conducted using an appropriate solver, applying numerical discretization methods and varying Reynolds numbers to study flow characteristics. Validation of the numerical results is performed by comparing with experimental data or benchmark studies. To optimize micromixer performance, multiple strategies are employed. Geometric optimization involves refining channel structures to enhance mixing while minimizing energy losses. Multi-objective optimization techniques, such as Moth flame optimization and Response Surface Methodology, are utilized to maximize mixing efficiency while reducing energy consumption. Additionally, the influence of nanofluids is analyzed by varying nanoparticle concentration and size to optimize fluid properties for enhanced mixing without significantly increasing viscosity.

Finally, a detailed performance evaluation is conducted by comparing different micromixer designs based on mixing efficiency and energy consumption. Sensitivity analysis examines the effects of design parameters, fluid rheology, and operating conditions on micromixer performance. A trade-off analysis between mixing efficiency, pressure drop, and power consumption helps identify the most effective micromixer configuration. This methodological framework ensures a systematic approach to computational analysis while integrating optimization techniques to improve micromixer efficiency.

3.1 Transport Phenomena

Micromixer transport processes may be analytically characterized at two fundamental levels: the molecule and continuum levels. These levels relate to many conventional length scales. The continuum model is well-suited for describing most transport phenomena in micromixers with length scales ranging from micrometers to centimeters, which align with typical practical applications. In contrast, molecular models characterize transport phenomena at minor length scales, specifically between one nanometer and one micrometer. Micromixers operating within this nanometer-to-micrometer range are referred to as "nanomixers."

Fluids are treated as continuous mediums at the continuum level, with their properties defined smoothly across space. This concept considers fluid qualities such as viscosity, density, and conductivity of material properties. Mass, energy conservation and momentum equations characterize transport phenomena. The governing equations in micromixer analysis are expressed as partial differential equations (PDEs), which must be solved to determine critical physical fields such as velocity, concentration, and temperature distributions. These equations describe the fundamental transport processes within the micromixer, including fluid flow, mass transfer, and heat transfer.

Innovation in miniaturization technology has significantly decreased the dimensions of microdevices. As nanotechnology advances, scientists and engineers are

increasingly confronting phenomena at the molecular scale. At this size, transport phenomena are dictated by molecule structures and intermolecular forces.

3.1.1 Molecular level

The Chapman-Enskog theory is derived from the Boltzmann equation and provides a means of calculating macroscopic transport coefficients based on microscopic molecular interactions. It assumes that gas molecules undergo elastic collisions and that their motion can be described statistically. This theory bridges the gap between kinetic theory and classical fluid mechanics, making it a powerful tool for analyzing transport phenomena in microscale and nanoscale systems.

To account for molecular interactions, particularly between nonpolar molecules, the Lennard-Jones (LJ) potential is commonly used. This empirical model describes the intermolecular forces governing the behaviour of gases and liquids. The Lennard-Jones potential (φ_{ij}) is mathematically expressed as:

$$\varphi_{ij}(r) = 4\varepsilon\left[C_{ij}\left(\frac{\sigma}{r}\right)^{12} - d_{ij}\left(\frac{\sigma}{r}\right)^{6}\right], \tag{3.1}$$

In this equation, σ signifies the molecular diameter, whereas r indicates the span separating the two interacting molecules. The parameter ε corresponds to the characteristic energy associated with the maximum attractive interaction between the molecules. The term $(\sigma/r)^{12}$ accounts for the repulsive potential due to electron cloud overlap at short distances. In contrast, the term $(\sigma/r)^{6}$ represents the attractive potential, primarily governed by van der Waals forces. The coefficients c_{ij} and d_{ij} depend on the types of molecules and are often assumed to have a value of 1. Table 3.1 describes the properties of certain common gases.

Table 3.1 Characteristic Energies with Diameters of Gases by Lennard-Jones

Gas	**Energy (ε/κ_B)**	**Diameter σ (nm)**
Air	97.00	0.3620
N_2	91.50	0.3680

CO_2	190.00	0.4000
O_2	113.00	0.3430
Ar	124.00	0.3420

Boltzmann constant: κ_B=1.38*10^-23 J/K

The characteristics of time define by the Lennard-Jones model:

$$\tau = \sigma\sqrt{(M / \varepsilon)} \tag{3.2}$$

In this context, M represents the molar mass, while the characteristic time corresponds to the oscillation period between molecular attraction and repulsion. Additionally, this model facilitates the calculation of the dynamic viscosity of a pure monatomic gas. The force (F_{ij}) between the molecules may be determined from the Lennard-Jones potential as follows:

$$F_{ij} = -\frac{d\varphi_{ij}(r)}{dr} = \frac{48\varepsilon}{\sigma}\left[c_{ij}\left(\frac{\sigma}{r}\right)^{13} - d_{ij}\left(\frac{\sigma}{r}\right)^{7}\right] \tag{3.3}$$

The Knudsen number (Kn) represents the ratio of the mean free path to the characteristic length of a device, like the channel diameter, serving as an essential dimensionless parameter. Since the Knudsen number links the device's length scale to the interactions between fluid molecules, it is instrumental in selecting the appropriate model for describing transport phenomena.

$$Kn = \frac{\lambda}{L} \tag{3.4}$$

i. Kn<10−3*Kn*<10−3, the fluid can be treated as a continuous medium.

ii. 10−3<*Kn*<10−1, an adjusted boundary conditions continuum model is suitable.

iii. Kn>10−1, a free molecular flow model most accurately represents the fluid.

Molecular dynamics is a computational technique used to simulate the motion of individual molecules. Newton's second law of motion governs the interactions between molecules. A spherical particle with mass mmm is the most straightforward representation of a molecule. The pairwise interactions between molecules are typically described using the Lennard-Jones force. The motion of a given molecule is dictated by Newton's second law, which provides a fundamental framework for analyzing molecular behaviour in dynamic systems:

$$m\frac{dr_i}{dt} = \sum_{j=1\neq 1}^{N} f_{ij} \tag{3.5}$$

N denotes the total quantity of molecules in the modelled system. The essential steps of a molecular dynamics (MD) simulation are as follows:

i. Defining the initial conditions and geometric parameters,
ii. Calculating the interaction forces (Equation 3.3), and
iii. Integrating the equations of motion (Equation 3.5).

Due to its deterministic nature, MD simulations are highly demanding in terms of computational resources. A statistical approach can significantly reduce resource requirements.

Direct Simulation Monte Carlo (DSMC) is an analytical technique for molecular-level modelling. DSMC uses molecules aggregated and represented singular particles. While the motion of the particles is simulated in a deterministic manner, the statistical definitions of the interactions between molecules inside each particle are used. The core steps of the Direct Simulation Monte Carlo (DSMC) method include:

i. Modelling the movement of particles,
ii. Identifying and indexing particles,
iii. Simulating collisions between particles, and
iv. Sampling macroscopic properties for analysis.

3.1.2 Continuum Level

Fundamental conservation equations, which regulate the behaviour of mass, momentum, and energy inside a fluid system, are used to describe transport phenomena at the continuum scale. These equations govern the phenomenon of transport. The complexity of turbulent flow modelling is avoided in micromixers, where fluid flow is predominantly laminar due to the small length scales and low Reynolds numbers. This simplification is advantageous, as turbulence is inherently chaotic and cannot be solved analytically, requiring complex numerical or empirical approaches.

In laminar flow conditions, transport processes are primarily driven by molecular diffusion and convection, allowing for a more straightforward mathematical treatment. The three fundamental conservation equations that describe transport phenomena in micromixers are:

i. Conservation of mass: Ensures that mass is conserved within the fluid domain, meaning that the net mass flux into a control volume equals the mass accumulation rate.
ii. Conservation of momentum: Describe the motion of the fluid by relating the forces acting on the fluid elements to their acceleration. These equations account for viscous effects, pressure gradients, and external forces, making them essential for predicting velocity profiles and flow patterns.
iii. Conservation of energy: Governs thermal energy transport within the fluid, incorporating heat conduction, convection, and, in some cases, heat generation. This equation is crucial when temperature variations influence fluid properties or mixing efficiency.

By solving these equations, the primary variables are obtained: the velocity field (v), pressure field (p), and temperature field (T). Fluid properties such as density,

viscosity, thermal conductivity, and enthalpy, which are functions of the thermodynamic state (defined by pressure and temperature), can be determined from these variables and subsequently integrated into the conservation equations.

3.1.2.1 *Conservation of mass*

The general continuity equation is

$$\frac{D\rho}{Dt} + \rho \mathrm{div}\nabla = 0 \tag{3.6}$$

where ∇ is the nabla operator and $\frac{D}{Dt}$ is the total derivative operator, which is defined as:

$$\frac{D}{Dt} = \frac{\partial}{\partial t} + u\frac{\partial}{\partial x} + v\frac{\partial}{\partial y} + w\frac{\partial}{\partial z} = \frac{\partial}{\partial t} + (v.\nabla \tag{3.7}$$

Where $v = (u,\ v, w)$ is the velocity vector.

3.1.2.2 *Conservation of momentum*

Newton's second law governs momentum conservation:

$$\rho\frac{Dv}{Dt} = f = f_{body} + f_{surface} \tag{3.8}$$

At the microscale, surface forces—such as electrostatic, viscous, and surface stress—play a dominant role, significantly outweighing bulk forces like gravity. When gravity is the only bulk force present, and surface forces result from pressure gradients and viscous effects under the assumption of constant viscosity and density, the Navier–Stokes equation can be calculated from the conservation equation. This formulation provides a fundamental framework for describing fluid motion in microscale systems, where surface interactions dictate flow behaviour more than inertial or gravitational effects.

$$\rho\frac{Dv}{Dt} = \rho g - \nabla p + \mu\nabla^2 v \tag{3.9}$$

P and μ represent the fluid's density and dynamic viscosity, respectively. In micromixers, pressure-driven flow in a straight microchannel is commonly encountered. Table 3.2 shows the solution for the microchannel's velocity and mean velocity distribution. The continuity equation is automatically satisfied for fully developed flow in the axial x-direction with v = w = 0 and ∂u/∂x=0. Under these conditions, the Navier–Stokes equation (3.10) simplifies to its two-dimensional form:

$$\frac{\partial^2 \mathrm{u}}{\partial \mathrm{y}^2} + \frac{\partial^2 \mathrm{u}}{\partial \mathrm{z}^2} = \frac{1}{\mu}\frac{\mathrm{dp}}{\mathrm{dx}} \tag{3.10}$$

Table 3.2 Analytical Solution for Velocity Profile in the Microchannel

Channel Type	**Solution**
Circle	$\mathrm{u}^*(\mathrm{r}) = 2(1 - \frac{\mathrm{r}^2}{\mathrm{r}_0^2})$ $\bar{\mathrm{u}} = \frac{1}{8\mu}(-\frac{\mathrm{dp}}{\mathrm{dx}})\mathrm{r}^2$
Ellipse	$\mathrm{u}^*(\mathrm{y},\mathrm{z}) = 2\left(1 - \frac{\mathrm{y}^2}{\mathrm{a}^2} - \frac{\mathrm{z}^2}{\mathrm{b}^2}\right)$ $\bar{\mathrm{u}} = \frac{1}{4\mu}(-\frac{\mathrm{dp}}{\mathrm{dx}})\frac{\mathrm{a}^2\mathrm{b}^2}{\mathrm{a}^2 + \mathrm{b}^2}$
Rectangle	$u^*(y,z) = \frac{48}{\pi^3}\sum_{n=1}^{\infty}(-1)^{n-1}\left[\left\{1 - \frac{\cosh((2n-1)\pi z/2a)}{\cosh((2n-1)\pi b/2a)}\right\}\right] \times \frac{\cos(2n-1)\pi y/2a}{(2n-1)^3} / \left\{1 - \frac{192a}{\pi^5 b}\sum_{n=1}^{\infty}\frac{\tanh((2n-1)\pi b/2a)}{(2n-1)^5}\right\}$ $\bar{u} = \frac{a^2}{3\mu}\left(-\frac{dp}{dx}\right)\left\{1 - \frac{192a}{\pi^5 b}\sum_{n=1}^{\infty}\frac{tanh((2n-1)\pi b/2a}{(2n-1)^5}\right\}$

3.1.2.3 *Conservation of energy*

The first law of thermodynamics governs energy conservation:

$$\mathrm{dQ} + \mathrm{dW} = \mathrm{dE}_{\mathrm{total}} \tag{3.11}$$

The energy equation can then be expressed in terms of the temperature T as:

$$\rho C_p \frac{DT}{Dt} = \beta T \frac{Dp}{Dt} + \text{div}(k\nabla T) + \Phi \tag{3.12}$$

For a Newtonian fluid, the dissipation function arises due to viscous stress (Φ):

$$\begin{aligned}\Phi = \mu \Big[& 2\left(\frac{\delta u}{\delta x}\right)^2 + 2\left(\frac{\delta v}{\delta y}\right)^2 + 2\left(\frac{\delta w}{\delta z}\right)^2 + \left(\frac{\delta v}{\delta x} + \frac{\delta u}{\delta y}\right)^2 \\ & + \left(\frac{\delta w}{\delta y} + \frac{\delta v}{\delta z}\right)^2 + \left(\frac{\delta w}{\delta y} + \frac{\delta u}{\delta z}\right)^2 \\ & + \left(\frac{\delta u}{\delta z} + \frac{\delta w}{\delta x}\right)^2 \Big] + \frac{2}{3}\mu\left(\frac{\delta u}{\delta x} + \frac{\delta v}{\delta y} + \frac{\delta w}{\delta z}\right)^2\end{aligned} \tag{3.13}$$

The general energy conservation equation simplifies to the heat-convection equation under the assumptions of constant thermal conductivity, incompressible flow, and negligible variations in kinetic energy. This reduction occurs because, in the absence of significant kinetic energy changes, the dominant mechanisms governing heat transfer are conduction and convection rather than energy exchanges due to velocity fluctuations.

$$\rho c_p \frac{DT}{Dt} = k\nabla^2 T \tag{3.14}$$

3.1.2.4 *Conservation of species*

The conservation of species leads to the derivation of the diffusion-convection equation:

$$\frac{Dc}{Dt} = D\nabla^2 c + r_g \tag{3.15}$$

Let c be the species' (solute) concentration; D be the species' diffusion coefficient inside the carrier fluid (solvent); and r_g be the species' generating rate per unit volume. This formulation assumes that the diffusion coefficient is uniform and isotropic, meaning that molecular diffusion occurs equally in all directions without spatial dependence. This equation is fundamental in microfluidics, micromixers, and lab-on-a-chip applications, where precise control over species transport and mixing is critical for achieving uniform concentration distributions and optimizing reaction kinetics.

3.2 Molecular Diffusion

3.2.1 Brownian motion and random walk

A particle's path as it moves through a series of steps, each done in a random direction, is called a random walk. Three key criteria must be followed to create a practical, simple, random walk.:

i. The particle begins from a designated initial position.

ii. Each step covers an equal distance, and

iii. The direction between consecutive points is chosen randomly.

Following these guidelines, a simple application may imitate a particle's random walk. In the case of a one-dimensional random walk along a line, the particle randomly chooses between two possible directions at each step. The distance covered in each step is considered to be s. The square location x(n) at step n may be expressed as:

$$x(n)^2 = \sum_{i=1}^{n} s_i^2 = ns^2 \propto Dt \tag{3.16}$$

Here, S_i denotes random step.

The Brownian motion of particles in a liquid result from continuous and random collisions with surrounding liquid molecules. These molecular interactions create an instantaneous imbalance of forces acting on the particle, causing it to undergo erratic movement. This stochastic motion is a fundamental phenomenon in microscale and nanoscale transport processes, playing a crucial role in diffusion-driven mixing, colloidal stability, and particle transport in fluids.

3.2.2 Stokes-Einstein model of diffusion

The time-dependent motion of a Brownian particle can be described using a force equilibrium equation, in which the random or stochastic force exerted by surrounding liquid molecules is a key contributing factor. This equation accounts for the interplay

between random thermal forces and systematic forces acting on the particle, providing a comprehensive mathematical framework for modelling its trajectory over time. This formulation is known as the Langevin equation, which serves as a fundamental tool in statistical physics for describing the dynamics of particles subject to both deterministic and random forces:

$$m\frac{dv}{dt} = \beta v + F(t) \tag{3.17}$$

where m is the particle's mass, β friction coefficient and F(t) represents the liquid molecules random force. At small timescales, inertial effects dominate the Langevin equation. Stokes' law for drag on a spherical particle with radius σ_p can determine the friction coefficient.

$$\beta = 3\pi\mu\sigma_p \tag{3.18}$$

3.2.3 Diffusion coefficient

3.2.3.1 *Diffusion coefficient in gases*

Using kinetic theory, the diffusion coefficient between two gases i and j, expressed in meters squared per second, can be determined (Cussler 2009):

$$D = D_{ij} = D_{ji} = \frac{1.86 \times 10^{-23} T^{2/3} \sqrt{\frac{1}{M_i} + \frac{1}{M_j}}}{p\sigma_{ij}^2 \Omega} \tag{3.19}$$

M represents the gas molar weights, T temperature, and p pressure. The collision diameter σ_{ij} is calculated as the mean of the diameters of the two gas molecules σ_i and σ_j:

$$\sigma_{ij} = \frac{\sigma_i + \sigma_j}{2} \tag{3.20}$$

3.2.3.2 *Diffusion coefficient in liquids*

Diffusion coefficients in gases are typically 10^{-5} m2/s, whereas in liquids, they are much smaller, around 10^{-9} m2/s. For large molecules, diffusion coefficients can be as low as 10^{-11} m^2/s. The Stokes-Einstein equation can estimate the diffusion coefficient (D_{ij}) of molecule I in a solvent with viscosity η_j.

$$D_{ij} = \frac{k_B T}{3\pi\mu_j\sigma_i} \tag{3.21}$$

Here, σ_i represents the diameter of molecule i. In this equation, the numerator corresponds to the molecule's kinetic energy, while the denominator accounts for the frictional force acting on it.

3.3 Chaotic Advection

A phenomenon known as chaotic advection occurs when a fundamental Eulerian velocity field causes a chaotic distribution of a Lagrangian marker, such as a tracer particle. This phenomenon is referred to as chaotic advection. The term "advection" refers to the movement of species across fluids, and chaos can occur even under laminar flow situations. The generation of chaotic advection can happen in a two-dimensional flow through the presence of time-dependent disturbances, or it can occur in a three-dimensional flow without such perturbations.

It is essential to distinguish chaotic advection from turbulence. In chaotic advection without disturbances, the velocity components at a specific point in space remain constant over time, whereas turbulence features random velocity components. In steady chaotic advection, streamlines cross, causing particles to change paths, leading to exponential particle divergence and enhanced mixing of solvent and solute. In time-periodic systems, chaotic behaviour occurs when streamlines intersect at two consecutive intervals.

In these equations, x denotes the intensity of convection, y signifies the temperature variance among descending and ascending currents, and z reflects the deviation of the vertical temperature profile from linearity.

3.3.1 Chaotic advection examples

3.3.1.1 *Lorentz's convection flow*

Lorenz developed a simplified set of equations to describe convection rolls in the atmosphere.

$$\begin{cases} {}^{dx}/_{dt} = Pr(y - x) \\ {}^{dy}/_{dt} = x\left(\frac{Ra}{Ra_c} - z\right) - y \\ {}^{dz}/_{dt} = xy - \beta z \end{cases} \tag{3.22}$$

3.3.1.2 *Dean flow in curved pipes*

Dean was the first to calculate the flow field within a curved pipe; a more detailed study can be found in (Ozen et al. 2006). Gratton later provided a detailed derivation (Zahn and Reddy 2006). In this model, the pipe has a diameter σ, and the coordinate system is defined using cylindrical coordinates. Here, s represents the coordinate along the centerline of the toroid, and q denotes the curvature. The metric for this coordinate system is expressed as follows:

$$(dq)^2 = (1 + \frac{r}{R}\sin\theta)^2(ds)^2 + (ds)^2 + (r)^2(d\theta)^2 \tag{3.23}$$

Assuming laminar flow, changes in s are considered negligible. The velocity components u, v, and w correspond to the directions s, r, and θ, respectively. In this coordinate system, the continuity equation (Equation 3.11) and Navier–Stokes equations (Equation 3.14) are reformulated as:

$$\frac{\partial v}{\partial r} + \frac{1}{r}\frac{\partial w}{\partial \theta} + \frac{v}{r} + \frac{v\sin\theta + w\cos\theta}{R + r\sin\theta} = 0 \tag{3.24}$$

To achieve adequate flow in a micromixer, it is essential to inject both the solute and the solvent from the right and left sides of the cross-section or the outer and inner

sides of the curved channel. This configuration captures the fluid particle paths on both channel sides. On the contrary, if the solute and the solvent are put in the channel's top and bottom halves, respectively, their routes will limit them to the channel's designated parts, prohibiting advective mixing. Regardless of whether they are introduced on the exterior or the inside of the curved channel, the trajectories display elliptic and homoclinic properties, demonstrating that they are stable. While longitudinal transport is advective, it remains orderly, indicating that the pathways do not intersect simultaneously. Because of this, it is impossible to generate chaotic advection using the Dean flow that was initially developed.

This ratio is often close to unity in practical channel designs, making the secondary flows more pronounced. The Dean number characterises the flow, which depends on the Re.

$$De = Re\sqrt{\frac{a}{R}} \tag{3.25}$$

The Dean number assesses the balance of centrifugal and inertial forces. A significant Dean number, De_{cr}=150, indicates a change in the secondary flow pattern. De<150 detects just two counter-rotating vortices, as previously described. However, with higher Dean numbers (De>150), centrifugal force takes over, forming two more vortices along the outer channel wall.

3.3.1.3 *Flow in helical pipes*

In helical pipes, the flow experiences a rotational motion across the entire cross-section as it moves along the central axis of the pipe, a phenomenon commonly denoted by q. This rotational effect arises due to the helical geometry, which introduces curvature and torsion into the system. When the torsion τ of the helical pipe remains constant, the angular rotation at a specific location s along the pipe's length can be mathematically expressed as τs.

Additionally, in a well-defined helical structure, the curvature κ, which describes the rate of change of the flow direction along the pipe, is given by (Germano 1982):

$$(dq)^2 = [1 - krsin(\theta + \tau s)](ds)^2 + (dr)^2 + r^2(d\theta)^2 \quad (2.26)$$

In this system of coordinates, the flow has a second-degree dependency on the torsion parameter τ. As a result, the velocity field solution for helical pipes is expressed as follows:

$$\begin{cases} \frac{dx}{dt} = hcos(\lambda s) + \frac{h'}{r} yxsin(\lambda s) + \frac{h'}{r} y^2 cos(\lambda s), \\ \frac{dy}{dt} = -\left[hsin(\lambda s) + \frac{h'}{r} xycos(\lambda s) + \frac{h'}{r} x^2 sin(\lambda s)\right] \\ \frac{ds}{dt} = 1 - r^2 \end{cases} \quad (3.27)$$

Here, torsion and curvature are combined in the geometry parameter.

3.3.1.4 *Flow in twisted pipes*

In a straight channel, fluid motion is typically confined to a single dimension, meaning that the flow primarily follows the channel's longitudinal axis with little to no movement in the transverse direction. However, when the channel is curved, the introduction of curvature induces additional velocity components in directions perpendicular to the main flow, resulting in a three-dimensional flow structure. This means that fluid motion is influenced both along the longitudinal axis and within the transverse cross-sectional plane, leading to the development of complex secondary flows.

$$\begin{cases} \Delta^2 u = \frac{1}{r}\left(\frac{\partial \psi}{\delta r}\frac{\partial u}{\delta \theta} - \frac{\partial \psi}{\delta \theta}\frac{\partial w}{\delta r}\right. \\ \Delta^2 \psi = \frac{1}{r}\left(\frac{\delta \psi}{\delta r}\frac{\delta}{\delta \theta} - \frac{\delta \psi}{\delta \theta}\frac{\delta}{\delta r}\right)\Delta^2 \psi + 2De^2 u\left(\frac{sin\theta}{r}\frac{\delta u}{\delta \theta} - cos\theta\frac{\delta u}{\delta r}\right) \end{cases} \quad (3.28)$$

3.4 Flow Computational Analysis

3.4.1 Mixing Eulerian method

The established assumptions formulate the simplified governing equations for flow dynamics in micromixers.

i. The surfaces are uniform and maintain a constant temperature.

ii. The fluid flow exhibits characteristics of being incompressible and follows Newtonian principles.

iii. The diffusion coefficient remains constant for both mixing fluids.

iv. The tension on the wall surface is minimal.

The continuity and Navier–Stokes equations are expressed as follows with the analysis of mixing with diffusion-advection model for the concentration species:

$$\frac{\partial U_i}{\partial x_i} = 0 \tag{3.29}$$

$$\rho\left(\frac{\delta U_i}{\delta t} + U_j\frac{\delta U_i}{\delta x_j}\right) = -\frac{\delta p}{\delta x_i} + \mu\frac{\delta}{\delta x_j}\left[\left(\frac{\delta U_i}{\delta x_j} + \frac{\delta U_j}{\delta x_i}\right)\right] \tag{3.30}$$

$$\frac{\delta C}{\delta t} + U_j\frac{\delta c}{\delta x_j} = D\frac{\delta^2 C}{\delta^2 x_j} \tag{3.31}$$

A common approach to evaluate micromixer performance is introducing a small quantity of dye into one of the fluids, which facilitates the visualization and quantification of the mixing process. The dye mass fraction, represented as C, is a key parameter in this analysis. In the underlying mixing model, the dyed and undyed fluids are assumed to have the same viscosity (μ) and density (ρ), assuming that variations in dye concentration do not affect these properties.

The transport of the dye within the fluid is governed by an advection-diffusion equation, which describes the passive movement of the solute due to fluid velocity and molecular diffusion. To ensure accurate representation of experimental conditions, appropriate boundary conditions are applied: one inlet introduces a pure fluid (e.g., water) with a dye mass fraction of 0, while the second inlet supplies a dyed solution (e.g., water with a dissolved dye) with a mass fraction of both fluids enter at

uniform velocities. A condition of zero static pressure is upheld at the outlet, while a no-slip boundary condition is applied at the channel walls.

The study of three-dimensional under constant viscosity and density laminar mixing has been extensively investigated and validated for various micromixer designs. However, when mixing involves fluids with differing densities and viscosities, a multi-component model may be utilized to predict local fluid properties based on mass fractions more accurately. This approach is particularly relevant for systems such as water-ethanol mixtures, where variations in density and viscosity significantly influence mixing behaviour.

This modelling approach determines how viscosity (μ) and density (ρ) depend on species concentration. Rather than relying on linear relationships between species concentration and fluid properties, they obtained functional approximations for density and viscosity by fitting experimental data. They found that linear dependence worked well for density. A combination of glycerol and water was used in the research conducted by Wu et al. to explore mixing in a planar passive micromixer. Utilizing a linear connection derived from the mass fractions of glycerol and water, the density of the mixture was calculated. Conversely, the viscosity and diffusion coefficients were assessed by applying nonlinear relationships based on the mass percentage of glycerol. Contrast with experimental results, which showed that the nonlinear approach provided enhanced accuracy, positioning it as a more practical option for simulating viscous mixing than the linear method. In summary, it is crucial to accurately represent the relationship between fluid properties—like density, viscosity, and diffusion coefficients—and concentration in numerical models to ensure precise predictions of species concentration.

Various studies have employed tetrahedral and hexahedral grids to explore flow and mixing dynamics in micromixers. Conducting a grid-sensitivity test is essential for determining appropriate grid cell sizes and dispersion, which is crucial for achieving precise predictions. This is true regardless of the grid system that is used. It is possible to obtain grid convergence for the velocity field; nevertheless, inconsistencies in the concentration field may still occur due to numerical (or false) diffusion, mainly when the Peclet numbers are high. Using a grid of poor quality might result in false

diffusion, leading to an overestimation of mixing. In a micromixer that Chen and Meiners had constructed, Liu experimented to determine the impact of false diffusion on tetrahedral and hexahedral grid materials. Based on the findings of the investigation, it was shown that tetrahedral cells exhibited a significantly higher level of erroneous diffusion compared to hexahedral cells, with the difference being approximately one order of magnitude. When doing mixing analysis, Liu suggested eliminating tetrahedral cells since hexahedral grids need fewer cells and greatly minimize the required computer work.

The governing equations are converted into algebraic equations through a finite-volume approach, with the discretization method chosen to influence the accuracy of the numerical solution. Further information on discretization techniques and solution strategies can be found in the studies by Patankar, Ferziger, and Perić. Liu demonstrated that higher-order discretization schemes have reduced susceptibility to numerical diffusion in the context of scalar mixing precision. The conventional upwind differencing method can generate considerable discretization errors in intricate flow calculations, but higher-order upwind techniques (second and third-order accurate) mitigate numerical diffusion. (Kim, Kim, and Kim 2018) conducted flow and mixing investigations in various micromixers, employing a high-resolution method to discretize the advection terms in the governing equations. This approach reduced numerical discretization errors through an automated correction process.

3.4.2 Mixing Lagrangian method

Numerical diffusion causes discretization errors that affect the numerical solution of the advection-diffusion equation about the concentration field. Many researchers have employed Lagrangian particle tracking to address this issue by studying mixing in various micromixers.

In the Lagrangian approach, many tracer particles are introduced at the micromixer’s inlet and individually tracked as they move through the flow field of the continuous phase. This method provides a particle-based perspective of fluid motion, enabling detailed insights into mixing efficiency, dispersion patterns, and transport phenomena within the micromixer. This formulation ensures that the particle's trajectory is

determined solely by the local velocity of the fluid, making it an effective technique for analyzing advection-dominated transport in microscale flows.

$$\frac{dx_p}{dt} = V_p \tag{3.32}$$

Bertsch et al employed particle tracking to provide a quantitative assessment of mixing alongside experimental data. Numerical research of mixing in a microchannel with patterned grooves was carried out by Wang et al. who utilized a particle tracking technique that was founded on a fourth-order adaptive Runge-Kutta integration scheme. To investigate the phenomena of chaotic advection, Poincaré maps were developed and analyzed on. The flow field for the continuous phase in a micromixer was computed using numerical simulations, which Aubin and colleagues carried out. Using a fourth-order Runge-Kutta scheme with an adjustable step size, they could monitor 2,480 equally dispersed particles and positioned on the right side of the mixer intake. To analyze mixing, the data collected from particle tracking were utilized. This study looked at the spatial arrangement of particulate in a descriptive plane, the maximum striation thickness, and the residence time profiles.

3.4.3 Quantification of micromixers

3.4.3.1 *Direct statistical approach*

The distribution of intensity values within an image, represented by its histogram H(I), provides a quantitative measure for evaluating the degree of mixing in a micromixer. This approach leverages image processing techniques to analyze the spatial variation in concentration, offering a non-intrusive and effective method for assessing mixing efficiency. The standardized concentration is regarded as equivalent to the standardized intensity values.

$$c = I = \frac{I - I_{min}}{i_{max} - I_{min}} \tag{3.33}$$

The normalized deviation of the intensity value or concentrations can quantify homogeneity.

$$\sigma = \sqrt{\frac{1}{N}\sum_{i=1}^{N}(c_i - \bar{c})^2} \tag{3.34}$$

The mean concentration can normalize this standard deviation to compute the mixing index:

$$MI = \sqrt{\frac{1}{N}\sum_{i=1}^{N}\left(\frac{c_i - \bar{c}}{c}\right)^2} = \sqrt{\frac{1}{N}\sum_{i=1}^{N}\left(\frac{I_i - \bar{I}}{I}\right)^2} \tag{3.35}$$

The mixing index thus ranges from 0 to 1.

$$\eta_{mixing} = 1 - MI = 1 - \sqrt{\frac{1}{N}\sum_{i=1}^{N}\left(\frac{I_i - \bar{I}}{I}\right)^2} \tag{3.36}$$

3.4.3.2 *Indirect methods*

Indirect approaches determine the extent of mixing by examining chemical reaction byproducts or changes in fluorescence intensity caused by pH differences in the combined fluids.

3.5 Methodology for Newtonian Fluid

This work correlates with Wang (Wang et al. 2012) (Dundi, Raju, and Chandramohan 2021), we improve geometry using ML tools (Moth Flame Optimization (MFO)) for determining a global minimum. Thus, by applying this ML technique, we can determine the best geometrical parameter to attain the maximum mixing index (φ) and minimum pressure drops (ΔP).

A hybrid T-geometry micromixer with the dimensions of channel length 3000µm, width 100 µm and depth 200 µm (Figure 3.1 & 3.2) was proposed for this work. A hybrid T-model with different twist and bend angle combinations with Re was designed for the analysis. Numerous simulations were done for twists and bend

angles, varying from 1 to 4 and 30^0, 50^0 and 70^0, respectively and Reynold numbers 10 to 550. All findings support the improved mixing in these mixers. Optimizing micromixers with twist and bend was accomplished by using CFD and MFO. This main objective is to study the impact of the twist and bend angle of the micromixer with various Re, on η and ΔP. The investigation aimed to understand how these two factors affect the overall performance of the mixing process and determine their significance in optimizing the design and operation of mixing systems. As found in (Prakash, Zunaid, and Samsher 2021; Sinha and Zunaid 2022), η increases with twist and bend angle in a monotonic manner. Additionally, the results showed that both ΔP and mixing energy costs increase with increasing twist and bend values as the Reynolds number increases. This work uses ML tools to optimise the micromixer model, especially using ANN and MFO algorithms. All simulations were carried out using the finite volume analysis within the Ansys fluent 2022 software, designed for incompressible and stationary fluid flow analysis. The use of this software allowed for a detailed and accurate representation of the fluid flow behaviour and the impact of various parameters on the η. Flow is governed by Newtonian fluid law with constant properties and is solved using equations 3.37 and 3.38. In the simulation, the velocity at inlets 1 and 2 was set to be equal, but the mass concentrations of solute C were different. Inlet 1 had a concentration of C = 1 mol/m^3, while inlet 2 was free of solute with a concentration of C = 0 mol/m^3, and the channel wall had a no-slip condition. This setup was chosen to investigate the mixing behaviour of a uniform laminar flow with solute concentrations (equation 3.39) at the inputs.

$$\vec{\nabla}.\vec{u} = 0, \tag{3.37}$$

$$\rho \frac{D\vec{u}}{Dt} = \vec{\nabla}\rho + \mu\nabla^2\vec{u}, \tag{3.38}$$

$$\frac{DC}{Dt} = \gamma\nabla^2 C \tag{3.39}$$

The variables $\vec{u}$, C and p define the velocity, concentration, and pressure, respectively, of fluid. Similarly, μ, γ, and ρ represent the fluid diffusion coefficient, viscosity, and density. These parameters play an important role in fluid mechanics and describe fluid's movement, behaviour and interaction in a system.

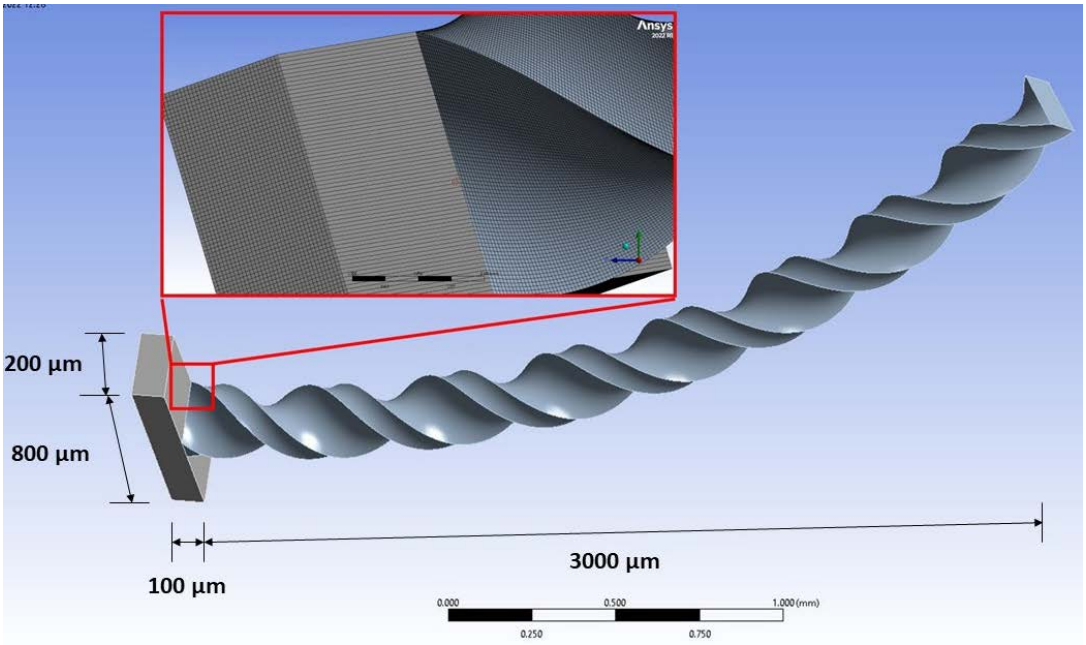

Figure 3.1 Dimension of the Proposed Hybrid with twists and bend Passive mixer

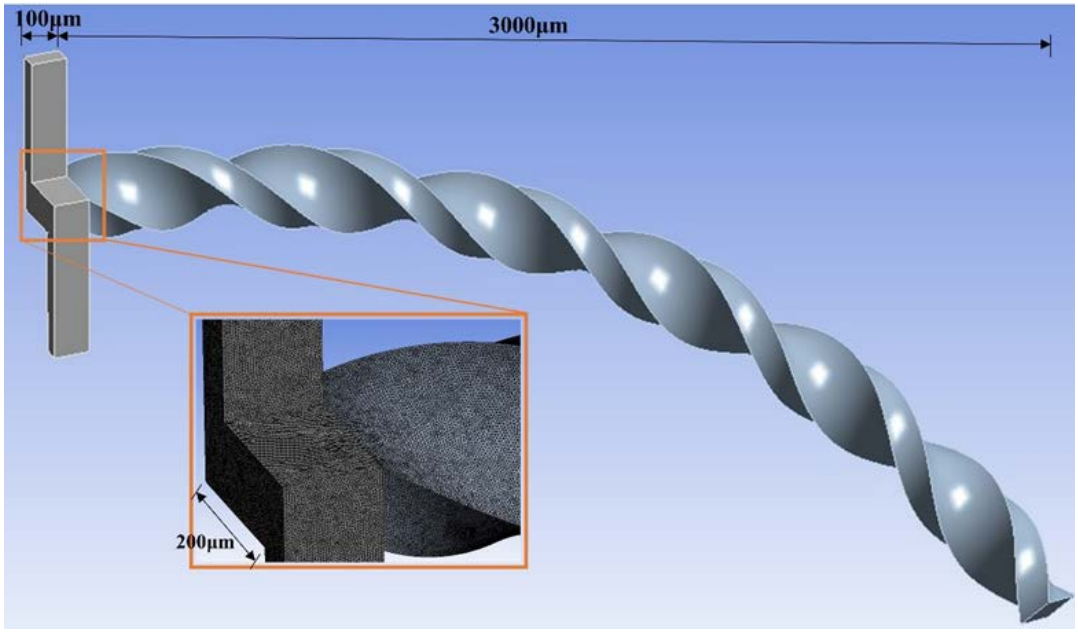

Figure 3.2 Offset Twists and Bend Passive Micromixer

The input and output boundary conditions were gauze pressure and coupled with pressure-velocity methods with a pressure-based solver using the SIMPLEC algorithm. The viscosity, coefficient of diffusion, and density are $\mu = 1*10^{-03}$ Pa·s, $D = 2*10^{-09}$ m ^{2} /s, respectively and $\rho = 998.2$ kg/m^3.

3.6 Methodology for non-Newtonian Fluid

A helical spiral micromixer with an axial channel length of 3000 μm, base diameter of 300 μm, and inlet cross-section of 100* 100 μm (shown in Figure 3.3) was proposed for this work. Their non-Newtonian nature makes modelling the fluids used in hydraulic fracturing and remediation considerably more difficult. The non-linear shear stress-strain relationship in non-Newtonian fluids is characterized by

$$\tau = \mu(\dot{\gamma})\dot{\gamma} \tag{3.40}$$

$$\dot{\gamma} = [\nabla u + (\nabla u)^T] \tag{3.41}$$

and the dynamic viscosity, or μ, depends on the shear rate ($\dot{\gamma} = \sqrt{\dot{\gamma}:\dot{\gamma}}$). Research on the flow characteristics of non-Newtonian fluids within micromixers predominantly centers on power-law fluids. The behaviour of certain fluids can be adequately characterized by the power law model within a limited range of shear rates. However, the majority of non-Newtonian fluids exhibit more intricate behaviour that is more accurately represented by alternative models, such as the Cross model, which is defined as follows Equation 3.42:

$$\mu = \frac{\mu_0 - \mu_\infty}{1 + (k\dot{\gamma})^n} + \mu_\infty \tag{3.42}$$

where k and n are fluid-specific parameters, μ_0 zero-shear viscosity, and μ_∞ infinite shear viscosity. Across a spectrum of shear rates, cross-model fluids exhibit behaviour akin to power-law fluids; outside this spectrum, they transition to regions of constant viscosity. The majority of biochemical fluids exhibit non-Newtonian characteristics. The non-Newtonian fluid does not adhere to the Newtonian law governing the relationship between stress and strain rate. Figure 3.4 shows how the Cross-model fluids and power law fluids differ. Few research studies have used Cross-model rheology, particularly in 3D systems, because the rheological model's increased complexity makes flow modelling in porous medium systems more complex.

This study employs the C-Y model for blood, taking into account the shear-thinning effect, as expressed below equation 3.43 (Chen and Chen 2024):

$$\mu(\dot{\gamma}) = \mu_{\infty} + (\mu_0 - \mu_{\infty})[1 + (\lambda\dot{\gamma})^a]^{(n-1)/a} \quad (3.43)$$

where μ_{∞}, and μ_0 indicates infinite and zero shear-rate viscosity; a, n, and λ are constant parameters (Abraham, Behr, and Heinkenschloss 2005) gives.

The ANSYS Fluent 2022 R1 program was utilized to solve the mathematical framework based on finite volume. The pressure-velocity coupling scheme COUPLED, the pressure interpolation equations of types PRESTO (Pressure Staggering Option), and the momentum interpolation equations QUICK (Quadratic Upstream Interpolation for Convective Kinematics) were employed. The convergence requirements were 10^{-06} for mass, 10^{-08} for momentum, and 10^{-10} for species concentration.

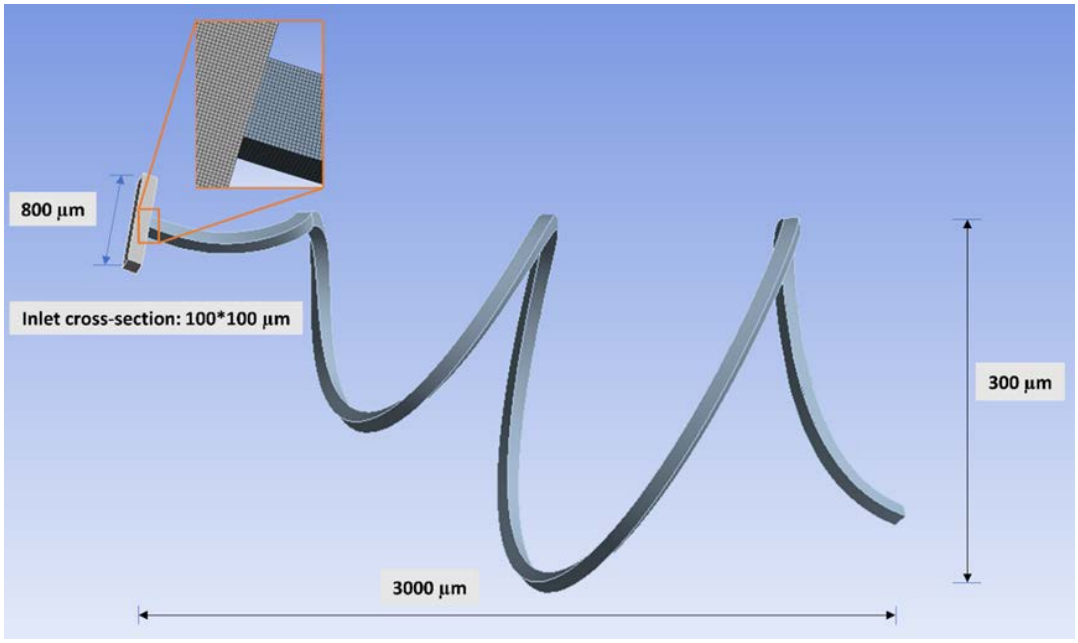

Figure 3.3 Details of the proposed spirally helical micromixer model with mesh of 3.2M tetrahedron elements

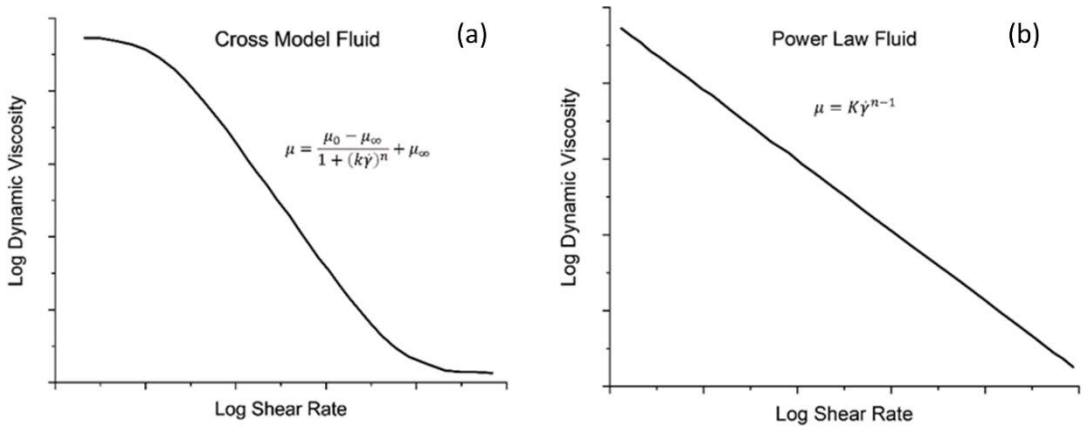

Figure 3.4 Comparison of (a) cross-flow model vs (b) power-law model

Using the modified Cross model, one can set the C-Y model easily

$$f = \left(1 + \left(\frac{A\alpha_T\dot{\gamma}}{\tau^*}\right)^{1-n}\right) \tag{3.44}$$

The Carreau-Yasuda model is continuous for all $\gamma \dot{\geq} 0$. The parameters $\alpha, n\ and\ \lambda$control how the fluid behaves in the non-Newtonian regime between these asymptotic viscosities. The persistence of this model at low shear rates facilitates simpler integration into numerical modeling frameworks.

Here, variable values are taken as follows $\mu_0 = 0.1600\ Pa.s$, $\mu_\infty = 0.0035\ Pa.s$, $\lambda = 8.2\ s$, $a = 0.64$, and $n = 0.218$ from (Abraham et al. 2005).

The concentration distribution governing equation is defined as follows:

$$u.\nabla c = D\nabla^2 c \tag{3.45}$$

Here c denotes the concentration of species, D is the diffusion coefficient ($1 * 10^{-10} m^2/s$). The conditions of boundary for domain of the micromixer model system are as follows:

$$\begin{cases} u = u_0, & at\ inlet \\ u = 0, & at\ wall \\ p = 0, & at\ outlet \\ c = c_0, & at\ inlet \end{cases} \tag{3.46}$$

The concentration distribution levels along the length of the primary channel can serve to evaluate the extent of fluid blending within micromixers. In the mixing process, mixing performance can calculated from the following equation:

$$\eta = 1 - \sqrt{\frac{\sigma^2}{\sigma_{max}^2}} \tag{3.47}$$

$$\sigma^2 = \int_{\Gamma_{outlet}} (c - c_{mean})^2 d\Gamma \tag{3.48}$$

$$\sigma_{max}^2 = \int_{\Gamma_{outlet}} (1 - c_{mean})^2 d\Gamma \tag{3.49}$$

The equations that control the system are resolved by incorporating them into the commercially available finite element analysis software Ansys Fluent. The CFD and Transport of Diluted Species modules compute the fluid flow and concentration issues. In this study, all fields representing state variables, specifically u, p, and c, are discretized employing parametric finite elements. The governing equations are analyzed using the FEM. The objective function and constraints are subsequently resolved.

The design parameter ‘Mixing energy cost’ was defined by (Ortega-Casanova 2017) as follows in equation 3.50.

$$MeC = \frac{\Delta P}{\eta} \tag{3.50}$$

Minimizing the MeC improves both the mixing rate and pressure differential at a constant flow rate. This paper also examines the system's performance in terms of η, ΔP, and MeC.

These steps are repeated until the specified criterion for the objective function value is achieved while also fulfilling the constraints:

$$\left|\frac{J^N - J^{N-1}}{J^N}\right| < \in \tag{3.51}$$

Here, the exponent N denotes the count of iterations performed during the optimization process, and ∈=1e-10 for this study. Should the criteria be met, the process concludes; otherwise, it persists. The design factor is modified through a method that utilizes the progression of equilibrium points.

The Batchelor scale can further assess the reliability of the mesh dependence analysis. The size of a fluid droplet is influenced by the duration required for energy dissipation in an eddy of scale χ (Maionchi, Ainstein, dos Santos, and Maurcio Bezerra de Souza Júnior 2022). Using the Batchelor scale, we may forecast the minimal scale of the concentration field and estimate the finest concentration structures using the equation 3.52.

$$\lambda_B = \frac{\chi}{\sqrt{Sc}} \tag{3.52}$$

χ, λ_B, and Sc represent the Kolmogorov length scale, the finest concentration structure, and the Schmidt number. In this study on viscous flow, the microchannel diameter of 100 µm can be used to approximate χ. Based on these parameters, the value of λ_B is 0.6174 µm. The grid of 2,751,890 cells has a maximum edge length of 0.0714 µm, accurately predicting concentration distribution.

3.7 Methodology for Nanofluid

Figure 3.2 shows the schematics of the proposed micromixer model for the investigation. The proposed model has dimensions of 100, 200, and 3000 µm as depth, width, and axial distance, respectively, with the oddest dimension of 50 µm. The governing equations' assumptions are 3D fluid flow, laminar and incompressible, steady and irrotational, and thermos-physical properties that are temperature-dependent for nanofluid.

The finite volume mathematical framework was solved using ANSYS Fluent 2022 R1. The pressure-velocity coupling technique COUPLED, pressure interpolation

equations PRESTO (Pressure Staggering Option), and momentum interpolation equations QUICK were used. The convergence criteria were 10^{-06} mass, 10^{-08} momentum, and 10^{-10} species concentration.

The thermos-physical properties of nanofluids have been determined using the following equations (Bezaatpour and Goharkhah 2020; Islami, Dastvareh, and Gharraei 2013):

$$\rho_{nf} = (1 - \emptyset)\rho_f + \emptyset\rho_{np} \tag{3.53}$$

$$(\rho C_p)_{nf} = (1 - \emptyset)\left(\rho C_p\right)_f + \emptyset(\rho C_p)_{np} \tag{3.54}$$

$$\mu_{nf} = \mu_f(1 + 2.5\emptyset) \tag{3.55}$$

Here, the indices *f*, *np*, and *nf* represent the base fluid, nanoparticle, and nanofluid, respectively. Additionally, the thermal conductivity is determined using the following equation.

$$k_{nf} = k_{static} + k_{brownian} \tag{3.56}$$

$$k_{static} = k_f\left[\frac{\left(k_{np} + 2k_f\right) - 1\emptyset(k_f - k_{np})}{\left(k_{np} + 2k_f\right) + \emptyset(k_f - k_{np})}\right] \tag{3.57}$$

$$k_{brownian} = 5 * 10^4\, \beta\emptyset\rho_f C_{p,f}\sqrt{\frac{kT}{\rho_{np}D_{np}}}\, g(\emptyset, T) \tag{3.58}$$

Here, $k = 1.38 * 10^{-23}\, J/K$ and β is a liquid fraction with the particle g(T, ∅) is model function as below;

$$g = (-6.04\emptyset + 0.4705)T + 1.722.3\emptyset - 134.63 \tag{3.59}$$

The ferrous oxide nanoparticles, with a diameter of 15 nm, are assumed to have a density of ρ = 4950 kg/m³. Additionally, their thermal conductivity and specific heat are considered k = 7 W/m·K and Cp = 640 J/kg·K, respectively.

3.7.1 Governing equations

i. Navier-Stokes Equation (Incompressible Flow)

$$\rho_{nf}\left(\frac{\delta u}{\delta t}+u.\nabla u\right)=-\nabla P+\mu_{nf}\nabla^2 u \tag{3.60}$$

ii. Energy Equation

$$\rho_{nf}C_{p,nf}\left(\frac{\delta T}{\delta t}+u.\nabla \mathrm{T}\right)=k_{nf}\nabla^2 T \tag{3.60}$$

iii. Transport Model

$$\frac{\partial \varphi}{\delta t}+u.\nabla\varphi=\nabla.(D_B\nabla\varphi+D_T\nabla T) \tag{3.61}$$

iv. Diffusion Coefficient

$$D_B=\frac{k_B T}{3\pi\mu_{nf}d_p} \tag{3.62}$$

3.8 Design Optimization of Micromixers

The shape of a passive micromixer's flow pathways significantly impacts mixing performance. As a result, it is crucial to identify the optimal configuration that maximizes mixing efficiency. However, in some micromixers, improving mixing performance can lead to an increase in pressure drop. Therefore, exploring different configurations that balance the mixing index and pressure drop is essential. Numerical optimization methods, combined with CFD models for flow and mixing, have proven effective for the design of micromixers. This encompasses single- and multi-objective optimization techniques for shape optimization.

3.8.1 Micromixers Optimization Technique

In passive micromixers, shape modifications can significantly influence the flow and mixing kinetics within the channel, affecting device performance. Many studies have investigated the influence of geometry and flow factors on mixing performance, creating viable micromixer designs. More advanced methods like design optimization have created more efficient designs. Various approaches to micromixer design include parametric studies, layout optimization through variational optimization, and systematic optimization approaches.

Aubin et al. investigated the influence of geometrical factors on an SHM employing particle tracing and CFD. They tested three design stipulations: groove depth, width and the number of grooves per cycle, quantifying mixing through maximum striation thickness and residence time for different parameter combinations. Their study provided insights into the secondary flow behaviour within the microchannel. Furthermore, the study examined the mixing performance of three types of grooved micromixers—SHM, slanted groove, and barrier-embedded micromixers—employing the "coloured particle tracking method" for qualitative and quantitative evaluations.

(Hossain et al. 2010) employed a variational optimization approach to design passive micromixers by solving a layout optimization problem. They used Navier–Stokes and convection-diffusion equations as constraints, with mixing performance as the objective function. Their numerical results demonstrated the success of the layout optimization method in achieving efficient mixing, and experiments confirmed its effectiveness in the conceptual design of micromixers.

Numerical optimization techniques, particularly those based on CFD evaluation, have helped design resilient and effective passive micromixers. The optimization objective(s) can include performance metrics like mixing index, pressure loss, and residence time. For micromixers, mixing efficiency and pressure loss are key parameters, with mixing efficiency being crucial for performance and pressure loss affecting pumping power requirements. Optimization might be single- or multi-objective (e.g., optimizing mixing efficiency while reducing pressure loss).

Given that optimization procedures often require numerous evaluations of objective functions, conventional methods can be computationally expensive. To address this, surrogate models build a functional link between the inputs and outputs, resulting in a credible approximation of the simulation paradigm. Surrogate-based optimization has been widely applied in various fields, including aerospace, to reduce computational costs.

Unlike single-objective, multi-objective incorporates many competing design goals. There are two primary methods for addressing a multi-objective optimization issue. The first way integrates numerous objectives into a single objective function by giving weights to each target, which are determined by the designer's preferences. A micromixer with a Tesla structure was modified and optimized using weighted average surrogate models. In this approach, the mixing index and pressure drop were linearly combined using a weighting factor to create a single objective variable (Hossain et al. 2010).

The second method utilizes multi-objective evolutionary algorithms (MOEAs) to produce multiple barter solutions for different objectives. Recent developments in MOEAs include the implementation of Pareto algorithms, Pareto archived evolutionary techniques, and elitist, non-dominated sorting genetic algorithms. Multi-objective problems produce a set of solutions, known as Pareto-optimal solutions, which allow designers to analyze the trade-offs between different design choices.

The authors (Hossain et al. 2010) used multi-objective genetic algorithms (MOGA) for the geometry optimization of SHMs, with mixing degree and pressure drop as the objective functions. This research aimed to construct a Pareto-optimal front, which optimized the trade-off between most excellent mixing efficiency and least pressure loss. Another piece of research was carried out by Cortes-Quiroz and colleagues, in which they sought to achieve Pareto-optimal designs by doing multi-objective optimization on a passive micromixer that had fin-shaped baffles and was placed in a T-channel.

Additionally, Afzal and Kim carried out multi-objective optimizations of several different micromixers. These included a SAR micromixer, a Sigma micromixer with convergent-divergent sinusoidal walls, and an SHM. RSA and RBNN are two

surrogate models that approximate the goal functions: the mixing efficacy and the non-dimensional pressure drop. After that, these surrogate models were put into MOGA to produce the Pareto-optimal front. It illustrates the barter between the mixing performance and the pressure drop. By the criteria that are unique to them, designers can select a solution along the Pareto-optimal front. Mixing effectiveness was the method that Afzal and Kim utilized to choose the optimum design from among the accessible Pareto-optimal options.

3.8.2 Surrogate Model vs Convention- Based Optimization

Researchers have utilized various techniques to optimize systems with specific inputs and responses. One of the easiest methods is a parametric study, which systematically analyses the effect of particular design parameters on the system's behaviour while keeping all other factors constant. However, a more advanced and comprehensive approach involves applying design of experiments (DOE) methodologies. DOE techniques allow for the simultaneous variation of multiple parameters to assess their collective impact on system performance, leading to more efficient optimization. Standard DOE methods include factorial designs, which systematically evaluate interactions between parameters, and Latin hypercube sampling, which ensures a well-distributed exploration of the input space for improved statistical accuracy. These approaches enable researchers to gain deeper insights into system dynamics and optimize performance more effectively.

While these approaches can help identify acceptable or feasible designs, finding the optimal design remains crucial. Using appropriate algorithms, optimization makes it possible to thoroughly investigate the whole design space to maximize or decrease a system's response. This procedure may be carried out using gradient-based methods, which are helpful for restricted and unconstrained optimization, or heuristic approaches, such as particle swarm optimization, which are helpful for complicated, nonlinear, or high-dimensional search spaces. Both of these methods are effective for solving optimization problems effectively. By selecting the appropriate optimization technique, engineers and researchers can enhance system performance, improve efficiency, and achieve desired outcomes more effectively.

Two optimization strategies: conventional and surrogate-based optimization. When evaluating the objective function(s) for fluid and thermal system optimizations, one of the most important steps is analyzing the underlying physical processes by employing the Navier–Stokes equations and the transport equations for heat and mass transfer while applying the proper boundary conditions. The traditional and advanced optimization methodologies use this analysis as a vital component. The manner in which the numerical model interacts with the optimization algorithm is the fundamental factor that differentiates these two methodological approaches. Because the numerical model is directly integrated with the algorithm in traditional optimization, it is necessary to do multiple simulations for each design iteration. This may be a time-consuming and computationally costly process. A significant disadvantage of this approach is the high computational cost associated with running the model repeatedly throughout the optimization process.

The use of surrogate modelling helps to alleviate this problem by lowering the amount of computer resources required and by providing a trustworthy approximation of the simulation data. A final surrogate model is generated by employing a suitable process that comprises training, testing, and validation, primarily when neural networks are utilized. This method is based on the results of the CFD simulation. Once validated, the surrogate model is used as a fitness function in the optimization algorithm, enabling faster and more efficient identification of the optimal design. To ensure the best results, the effectiveness of the surrogate model is evaluated in terms of its ability to explore the design space globally and exploit it locally before being coupled with the optimizer. Surrogate-based optimization has become widely used in the design optimization of micromixers.

3.8.3 Design of Experiment (DOE)

Investigation of the design variable space is accomplished through the use of Design of Experiments (DOE) methodologies. It is done to optimize the quantity of information obtained by determining the relationship between the multiple components that impact a process and the outcome of that process. In the optimisation process, the DOE techniques are utilized to generate design points, which are subsequently used in creating a surrogate model. When it comes to fitting different

models, having a sample blueprint that is adequately built is quite necessary. Latin hypercube sampling, often known as LHS, is a type of stratified sampling that can be applied to a wide range of variables. It is one of the DOE methods that is utilized the most commonly.

3.8.4 Latin Hypercube Sampling (LHS)

LHS is a stratified variant of Monte Carlo sampling. The sampling zone is systematically partitioned by segmenting the range of each x component. We will exclusively examine the scenario in which the parts of x are independent or may be converted into an independent basis. Furthermore, generating samples for coupled components with a Gaussian distribution is readily attainable. As previously outlined, LHS functions to produce a sample size N from the variables $x1$, $x2$, $x3$, ..., xn. The range of each variable is divided into N non-overlapping intervals with equal probability size $1/N$. A value is randomly picked from each interval according to the probability density inside that interval. The N values acquired for $x1$ are randomly matched with the N values of $x2$. N pairings are randomly paired with the N values of $x3$ to create N-triplets, and this process continues until a collection of N-tuples is established. This collection of N-tuples constitutes the Latin hypercube sample. Therefore, for specified values of N and n, there are $(N!)$ $n-1$ potential interval combinations for an LHS. A 10-run Latin Hypercube Sampling (LHS) for three normalized variables (range [0, 1]) utilizing a uniform probability density function is presented below. The values separated at equal probabilities are 0, ..., 0.8, 1.

3.8.5 Surrogate Modelling

In optimising thermo-fluid, numerous numerical analyses are needed to assess objective function(s). Still, each simulation can be time-consuming due to the complexity of the non-linear governing differential equations. To reduce this burden, surrogate modelling is used to create approximation models that closely replicate the behaviour of the simulation model. Surrogate modelling's key advantages are its computing efficiency in assessing the goal function(s) and its correctness in reflecting the design space features. Both of these advantages are associated with surrogate

modelling. In the following discussion, the mathematical formulas for a variety of surrogate models are presented.

3.8.5.1 *Response surface approximation (RSM)*

A mathematical model, often a polynomial equation, is used in RSM. This model is used to characterize the connection between the input variables and the response variable(s) that are of interest (Equation 3.63). The model is fitted to experimental data from a series of designed experiments. A factorial design is often utilized in the execution of these studies. In this design, many combinations of input variables are evaluated to assess the influence that these combinations have on the response variable.

$$Y = b_o + \sum_{i=1}^{3} b_i x_i + \sum_{i=1}^{3} b_i x_i^2 + \sum_{i=1 j=1}^{3} b_i x_i x_j \tag{3.63}$$

$$d_n = \begin{bmatrix} 0 & n < L_n \\ \dfrac{n - L_n}{G_n - L_n} & L_n < n < G_n \\ 1 & n > G_n \end{bmatrix} \tag{3.64}$$

$$d_n = \begin{bmatrix} 0 & n > H_n \\ \dfrac{n - H_n}{G_n - H_n} & G_n < n < H_n \\ 1 & n < G_n \end{bmatrix} \tag{3.65}$$

$$\text{Desirability} = [\pi(\mathrm{d_n w_n})]^{\frac{1}{\mathrm{w}}} \tag{3.66}$$

Here, n, G_n, L_n, H_n, and r_n the forecast value, the target value, the lower suitable value, the higher suitable value, and the desirability function weight when it comes to the nth output, respectively. The variable w_n is used to denote the significance of the nth output, and the value of W is equal to the sum of w_n. The value of the desirability factor can range from 0 to 1, with 1 indicating the ideal choice that is desired the most and 0 indicating the one that is desired the least.

RSM aims to determine the optimal input variables for maximising or minimising the output variable(s) within a specified range. ANOVA was used to assess the relevance

of each input variable's role in influencing output responses and the model's dependability. From the 3D response surface plot, the interaction influence of input parameters on output was observed.

Using RSM in conjunction with a desirability function, one may locate the best possible answer for a response with several objectives. According to the framework of the desirability approach, the solution that is considered to be the best alternative is the one that holds the highest combined desire factor. The equation (3.64) is used to determine the individual desirability (dn) for an output parameter that is intended to maximize the output, whereas the equation (3.65) is utilized to minimize the output. The combined desirability is determined as described in Equation (3.66).

The simulation results are statistically analysed using ANOVA, a method based on the principle of general variance, employed to assess differences among all the findings in a sample. Using ANOVA is quite helpful and illuminating when comparing data across many categories. The p-value, F-value, R^2, Adj R^2, and Pred R^2 values in the ANOVA test, which represent the variance of the data from the mean, are indications of the validity and quality of the results.

3.8.5.2 *Artificial neural network (ANN)*

An analytical tool called ANN is used to validate the correlation between input and output variables and verify the data's predictive regression. The multilayer perceptron (MLP) neural network architecture and the backpropagation technique are used in this ANN study. MATLAB R2020a is used for coding and execution. MLP planning, as shown in Figure 3.5, is in the format of A-H1-H2-Z, where A and Z indicate the input and output layers, and H1 and H2 are hidden layers. For each output, a network is built to train the DOE findings. Each hidden layer neuron in the network ranges from 1 to 10, and many neuron combinations are used during training. Then, the neuronal pairings with the lowest RMSE are chosen. The best neuron combination discovered is then utilised to build a new network for each output. Mean square error (MSE) was used as the performance function, while Levenberg Marquardt (trainlm) was used as the training function. The hidden layer uses the Tan-sigmoid, and the output layer is

handled by Log-sigmoid functions of transfer, respectively. From datasets, train network 70%, test 15%, and the rest to validate was used.

3.8.5.3 *Moth flame optimization (MFO)*

The MFO algorithm was modelled after moths' navigational strategy (Mirjalili 2015). Moths have a highly efficient mechanism for flying at night that maintains their orientation relative to the moon and makes them move long distances in a straight line. Solutions proposed for the MFO method are moths and the variables in the space. The moths may change their location vectors and fly in 1-D, 2-D, 3-D, or multidimensional space. The population-based nature of the MFO method requires the pair of moths to be described in a matrix (equation (3.67)) as mentioned below:

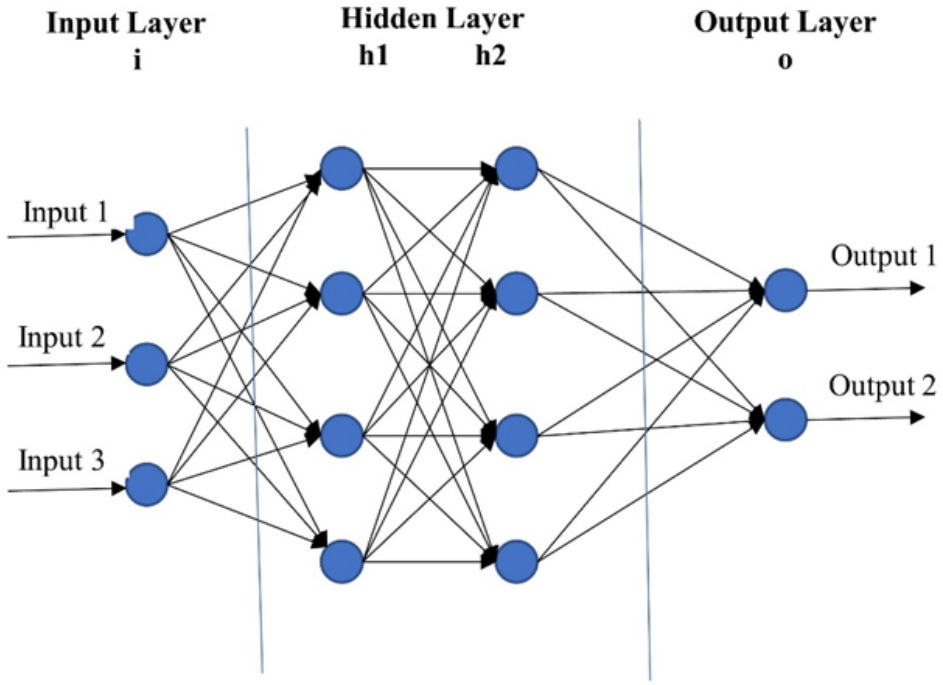

Figure 3.5 ANN Schematic

$$M = \begin{bmatrix} m_{1,1} & \cdots & m_{1,d} \\ \vdots & \ddots & \vdots \\ m_{n,1} & \cdots & m_{n,d} \end{bmatrix} \tag{3.67}$$

$$S(M_i, F_j) = D_i . e^{bt} cos(2\pi t) + F_j \tag{3.68}$$

Here, n is the moth number, d is the variable, S is the spiral function, M_i and F_j are ith moth and jth flame and D is the distance of i^{th} moth and j^{th} flame; equation (3.68) shows the spiral moth path simulations, as depicted in Figure 3.7 (a). The variable t indicates the adjacent position of the moth to the flame ($t = -1$ is proximate and $t = 1$ is farthest), displayed in Figure 3.7 (b).

By increasing moths, the probability of finding the global minimum is higher. However, it has been shown that 30 is an appropriate number of months for resolving optimisation issues.

3.8.5.4 *Harris hawk optimization (HHO)*

HHO is a metaheuristic optimization algorithm inspired by the hunting behaviour of Harris's hawks, a species of raptors. The algorithm mimics these birds' cooperative hunting strategy to search for and capture Prey.

In HHO, the optimization problem is represented as a population of hawks. Every Hawk symbolises a prospective solution to the problem, and its location within the search space corresponds to the values of the decision variables. The Hawks collaborate and share information to improve the overall search process. Given that HHO is a population-based, gradient-free optimization method, any optimization issue may be addressed with it with the correct formulation. All of the HHO stages are depicted in Figure 5.4. They are discussed in the following sections (Heidari et al. 2019).

i. Exploration phase

Here, hawks explore and trail prey using their instinct. The Harris hawks in HHO huddle at isolated spots and use one of two methods to watch for Prey to appear.

$$X(t+1) = \begin{cases} X_{random}(t) - r_1 |X_{random}(t) - 2r_2 X(t)| & q \leq 0.5 \\ X_{prey}(t) - X_m(t) - r_3\big(Lb + r_4(Ub - Lb)\big) & q < 0.5 \end{cases} \quad (3.69)$$

X(t+1) denote the Hawks position vector for iteration. X_{prey} denotes prey location, X(t) symbolises hawks' current location, and r_1, r_2, r_3, r_4, and q are arbitrary numbers between [0,1], which changes with iteration. Ub and Lb symbolise variables of upper and lower bonds. $X_{random}(t)$ is the arbitrarily chosen Hawk's location and X_m is the average current location of the hawks' population.

$$X_m(t) = \frac{1}{N}\sum_{i=1}^{N} X_j(t) \tag{3.70}$$

$X_i(t)$ is every hawk location in iteration, and N is the total hawk.

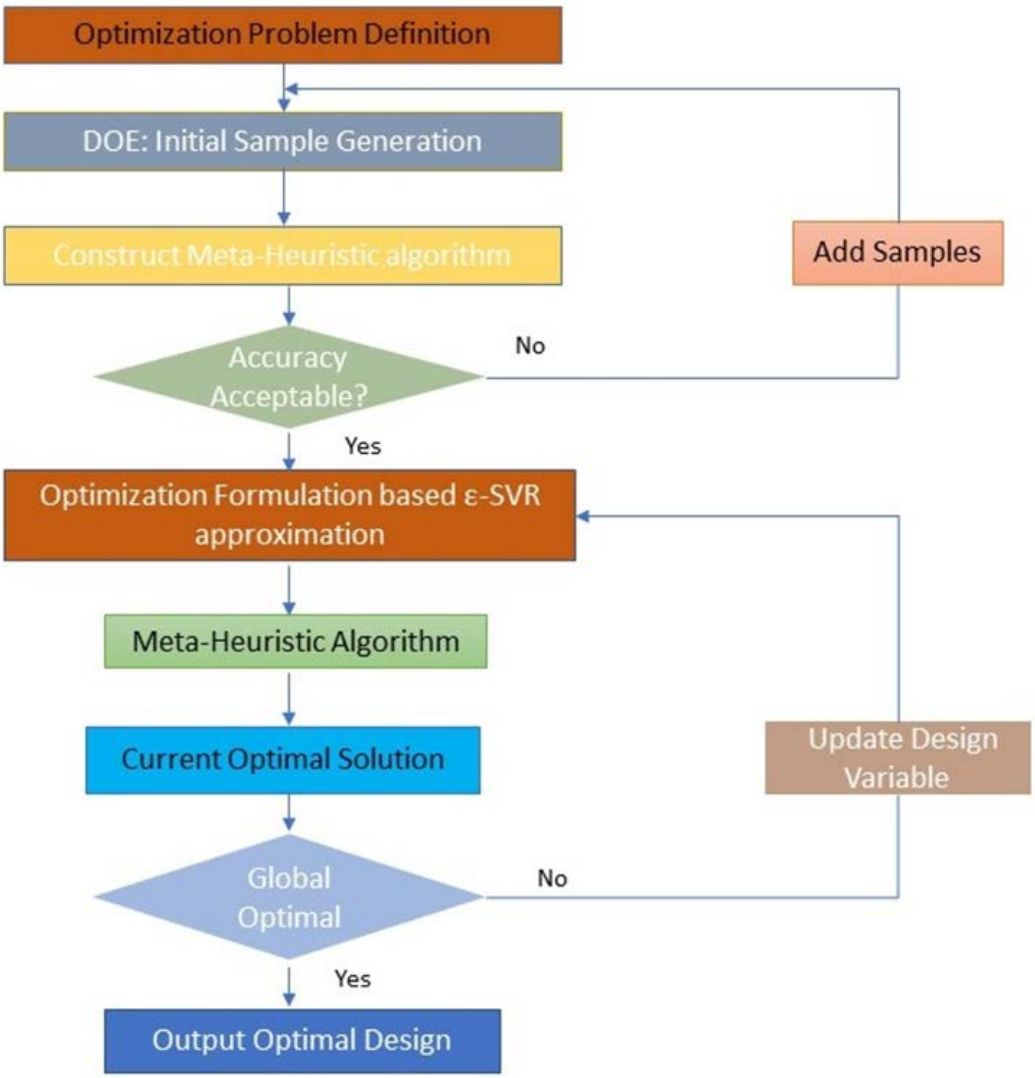

Figure 3.6 Optimization Flow Chart

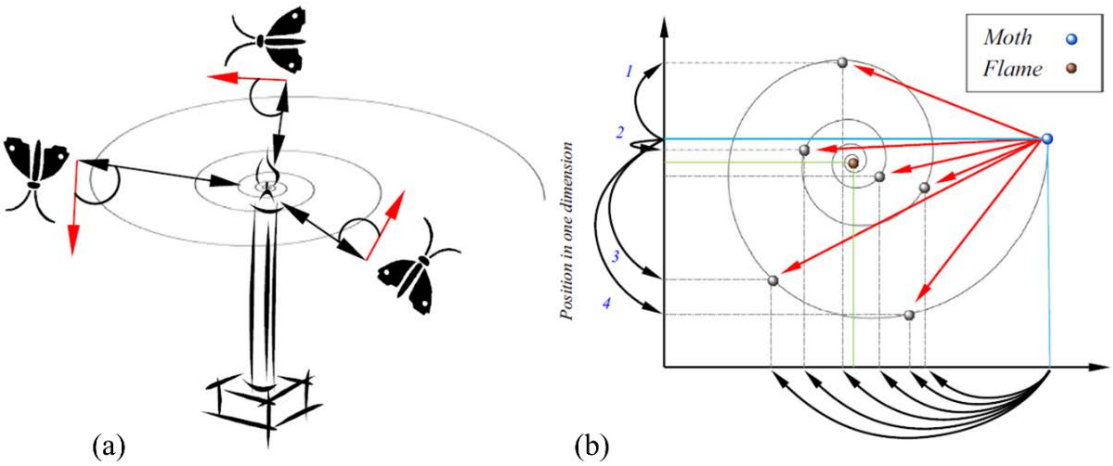

Figure 3.7 (a) Moth mechanism on the flame (b) Possible logarithmic spiral path of the moth with flame (Mirjalili 2015)

The transformation from exploration to exploitation

The HHO technique exploits Prey's behaviour to escape. Hence, the energy of Prey diminishes. The energy of Prey is represented by equation 3.71 to illustrate this step:

$$E = 2E_o(1 - \frac{t}{T}) \tag{3.71}$$

E denotes the energy of Prey fleeing, and E_o is the initial energy state.

ii. Exploitation phase

When Hawk attacks Prey, they try to escape, and the probability of fleeing is $|r| < 0.5$, getting caught $|r| \geq 0.5$.

iii. Soft besiege

Here $r \geq 0.5$ and $|E| \geq 0.5$, Prey jumps arbitrarily here and there to flee. This action can be explained in the following equations 3.72 and 3.73.

$$X(t+1) = \Delta X(t) - E\left[JE_{prey}(t) - X(t)\right] \tag{3.72}$$

$$\Delta X(t) = X_{prey}(t) - E[\Delta X(t)] \quad (3.73)$$

Equation 5.10 and Equation 5.11 depict the exploits of this model. ΔX(t) indicates the distinction between the prey location and the current location of iteration t.

iv. Hard besiege

Here $r \geq 0.5$ and $|E| < 0.5$, Prey wear out and its present location is depicted in equation 3.74.

$$X(t+1) = X_{prey}(t) - E[\Delta X(t)] \quad (3.74)$$

v. Soft besiege with progressive dive

In this stage, $|E| \geq 0.5$ and $r < 0.5$, Prey has sufficient energy to flee. Hawks' movement is described by equation 3.75

$$Y = X_{prey}(t) - E\left|X_{prey}(t) - X(t)\right| \quad (3.75)$$

vi. Hard besiege with progressive dives.

Here $|E| < 0.5$ and $r < 0.5$ prey not able to prey, hawk ambush and kill the Prey. For this challenging besiege, conditions are described in equations 3.76, 3.77 and 3.78

$$X(t+1) = \begin{cases} Y & if\ F(Y) < F(t) \\ Z & if\ F(Z) < F(t) \end{cases} \quad (3.76)$$

$$Y = X_{prey}(t) - E\left|X_{prey}(t) - X_m(t)\right| \quad (3.77)$$

$$Z = Y + S * Lf \quad (3.78)$$

3.9 Multi-Objective Optimization

A multi-objective optimization issue is one in which numerous objectives are optimized at the same time. Figure 3.6 shows the flow chart for multi-objective optimization. This instance illustrates this approach in the following equation 3.79:

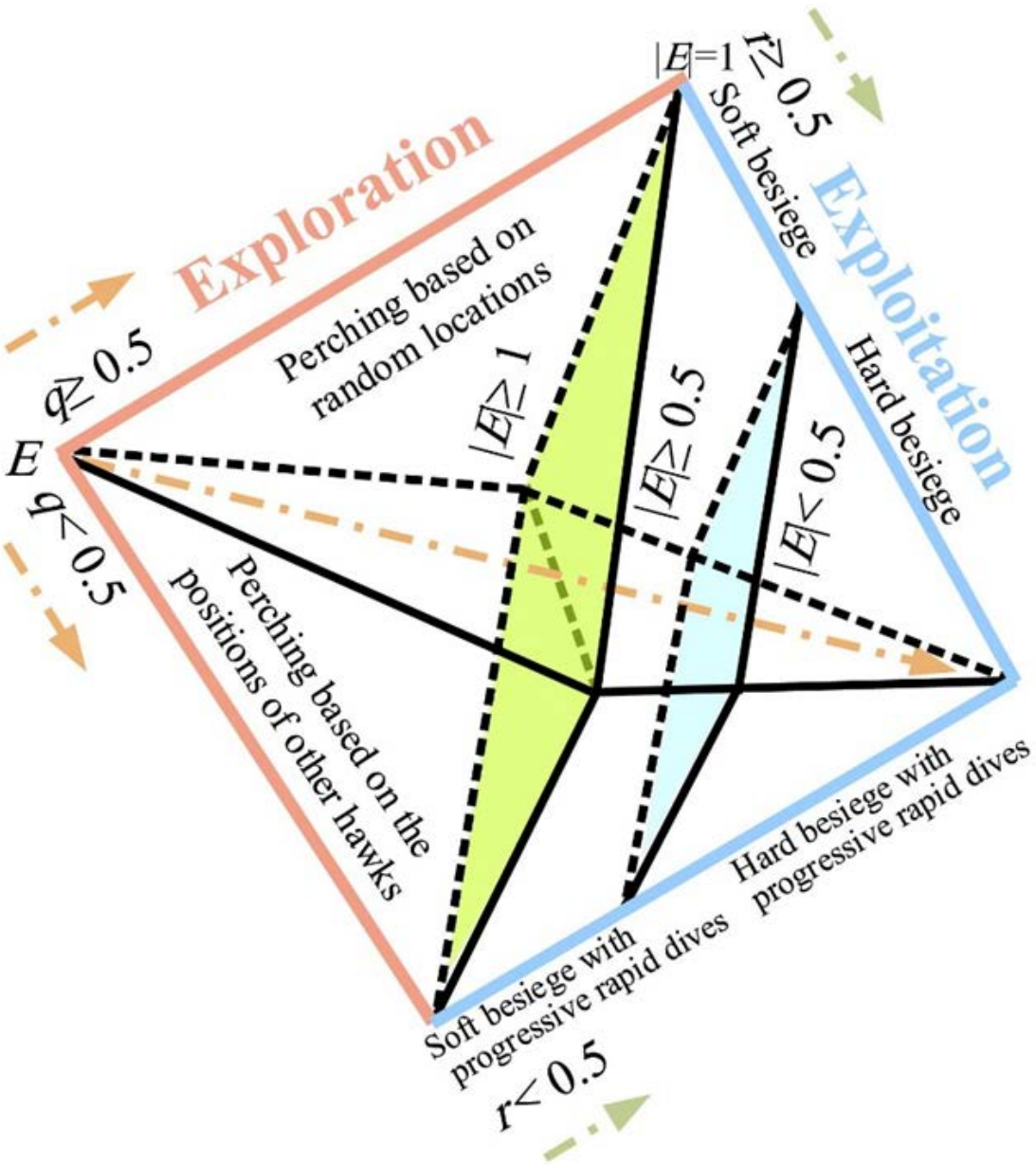

Figure 3.8 Various Stages of HHO (Heidari et al. 2019)

$$\begin{cases} Max: \eta = fn_1(Re, Bend.Twist) \\ Min: \Delta P = fn_2(Re.Bend, Twist) \\ Subject: \\ 0.05 \leq Re \leq 450 \\ 30^{\circ} \leq Bend \leq 70^{\circ} \\ 1 \leq Twist \leq 4 \end{cases} \quad (3.79)$$

The term "Pareto-optimal solutions" refers to the various solutions that are generated by a problem that has several objectives. Within the context of a multi-objective optimization problem, solutions can be categorized as either dominated or non-dominated, depending on whether or not they are viable sets of solutions. When determining dominance, the following requirements are considered: a design x1 is considered superior to another design x2 if it is superior to x2 in all goals and is superior to x2 in at least one objective. The Pareto-optimal set is comprised of all designs that are not dominated by any other design. The Pareto-optimal set's representation in functional space is called the Pareto-optimal front. It illustrates the trade-offs among conflicting objectives, allowing analysis of the compromises between designs. Since each solution in the Pareto-optimal set is globally optimal, none is superior to the others across all objectives. Therefore, selecting a Pareto-optimal solution that meets specific requirements depends on the designer's judgment.

Optimization of the micromixer is derived from meta-heuristic algorithms that were selected and coded in MATLAB software: Response Surface Methodology (RSM) and Haris Hawk Optimization (HHO), whose steps are shown in Figure 3.8 as a flowchart.

3.10 Summary of Methodology

This chapter presents the computational framework and offers an in-depth analysis of numerical methods for studying flow and mixing in micromixers. The flow and mixing analyses are carried out using the Eulerian and Lagrangian approaches, discussing each approach's relative advantages, disadvantages, and suitability for different mixing scenarios. The chapter also covers various aspects of numerical schemes, including discretization errors and grid requirements. Since many studies rely on commercial CFD software, relevant details about mixing problems are provided in these packages. The chapter concludes by discussing the technique for

characterizing mixing using concentration data from a computational grid, laying the foundation for evaluating the performance of different micromixer designs. The chapter is divided into three sections: Section 3.4.1 covers the Eulerian approach, including mixing models, boundary conditions, and the numerical methods used to solve the governing equations; Section 3.4.2 presents the Lagrangian approach; and the final section discusses methods for quantifying mixing.

Multi-objective evolutionary algorithms (MOEA) aim to find the best trade-offs between conflicting objectives. However, real-world optimization problems (e.g., in engineering, finance, and AI) often involve expensive simulations or experiments. Surrogate modelling helps make MOEA more efficient by approximating complex functions.

Chapter 4 RESULTS AND DISCUSSION

The mechanics of molecular diffusion and advection are two of the most crucial mass transport mechanisms, as discussed in Chapter 3. It is via advection that mixing is improved in fluid flows with low Reynolds numbers. Advection occurs typically in the primary flow direction in most passive micromixers that rely on molecular diffusion. This means that the transverse transport of chemicals completely depends on molecular diffusion. Advection that follows a three-dimensional trajectory, on the other hand, has the potential to create secondary transversal transport and make mixing far more effective. The fundamental design principle for generating advection involves altering the channel geometry to stretch, fold, and disrupt laminar flow. As noted, these processes are chaotic. Chaos requires that streamlines intersect at different times, a phenomenon observed in time-periodic or spatially periodic flows. The former can be achieved through boundary motion, while the latter arises from periodic variations in geometry. Chaotic advection has been observed across various Reynolds numbers depending on the geometrical configuration. As a result, micromixer designs utilizing chaotic advection are classified based on their operating Reynolds number ranges. A Reynolds number (Re) above 100 is considered high, while the intermediate range falls between 10 and 100, and Re below 10 is classified as low. The following section focuses on various passive micromixers studied in my work that rely on chaotic advection.

4.1 Validation and Grid Sensitivity Test

4.1.1 Newtonian Fluid

As observed in Figure 4.1, the computationally generated findings displayed high levels of accuracy to the experimental data (Figure 4.1 shows graphically whereas Figure 4.3 displays comparison at outlet ‘mass fraction’). A micromixer's estimated mixing performance is mesh-dependent. So, grid convergence research was carried out to identify the ideal mesh. The scale of the finest concentration formations can be roughly calculated using $\lambda_c = \lambda_v/\sqrt{Sc}$, where λ_v the most minor velocity structures' length scale (Rahmannezhad and Mirbozorgi 2019). The velocity length scale, which represents the smallest distance over which velocity variations occur, could be

estimated using the parameter λ_v. This approximation provides a convenient way of quantifying the length scale of velocity variations in the system. Given the value of Sc, approximately 890, λ_c, which is about 6.7 μm. This estimation was based on the relationship between Sc and λ_c, and provides a quantitative measure of the most miniature length scale at which concentration variations occur in the system. The mesh used for the simulations was designed with a grid size of approximately five μm, smaller than the estimated concentration length scale, λ_c. This was done to ensure high accuracy and resolution in the simulations. The mesh contained 1556088 nodes, allowing for an adequate system representation. A coarser mesh with 3254784 nodes and a refined mesh with a grid of 2060740 nodes were employed for mesh analysis, as shown in Figure 4.3. All of them were used in simulations, producing results for the first two nearly identical meshes.

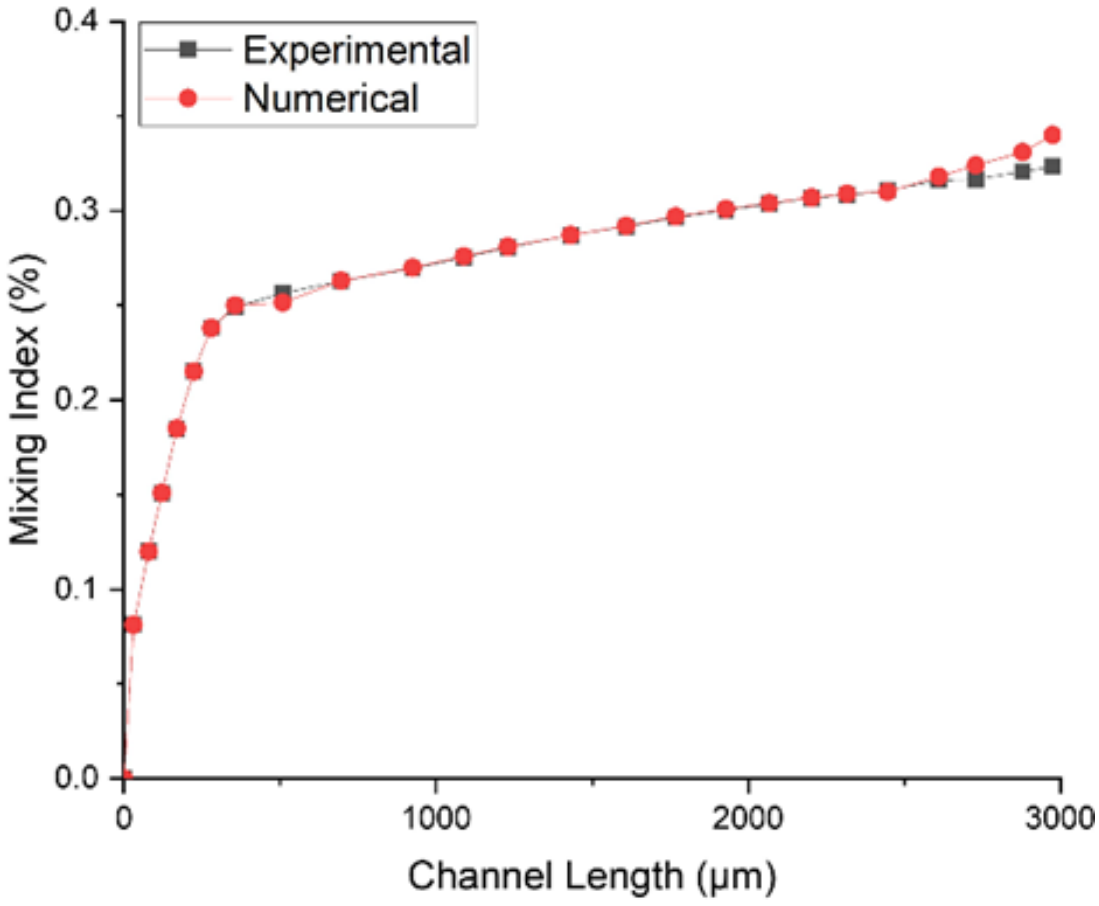

Figure 4.1 Validation of TBM with numerical and experimental (Dundi et al. 2021)

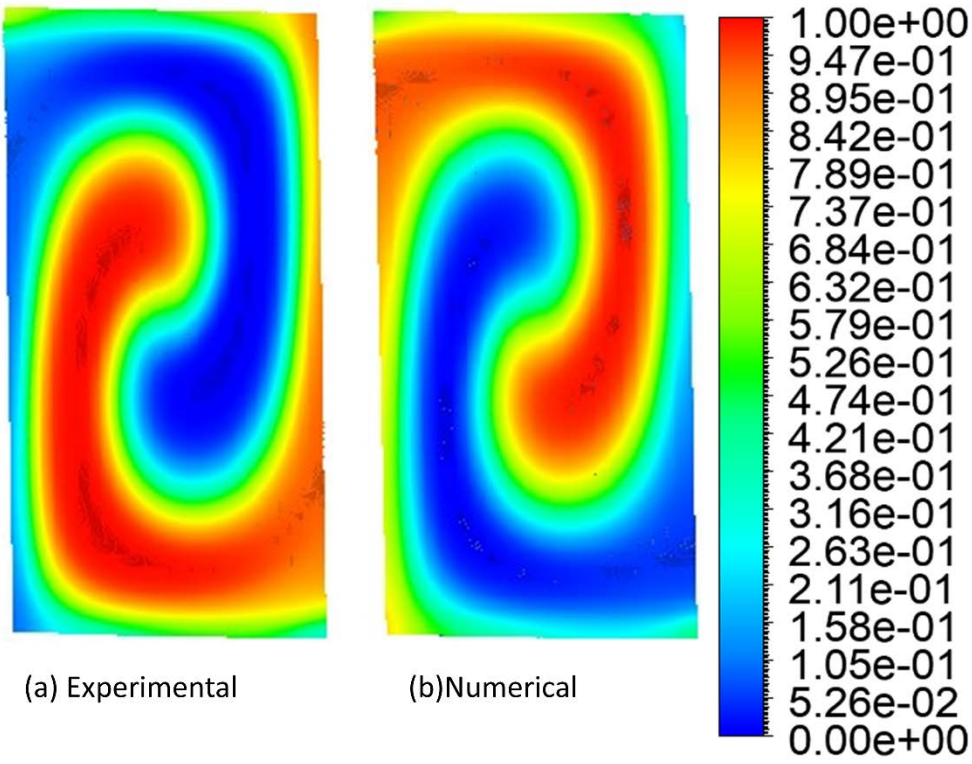

Figure 4.2 The mass fraction at the outlet for a) Experimental and b) Numerical

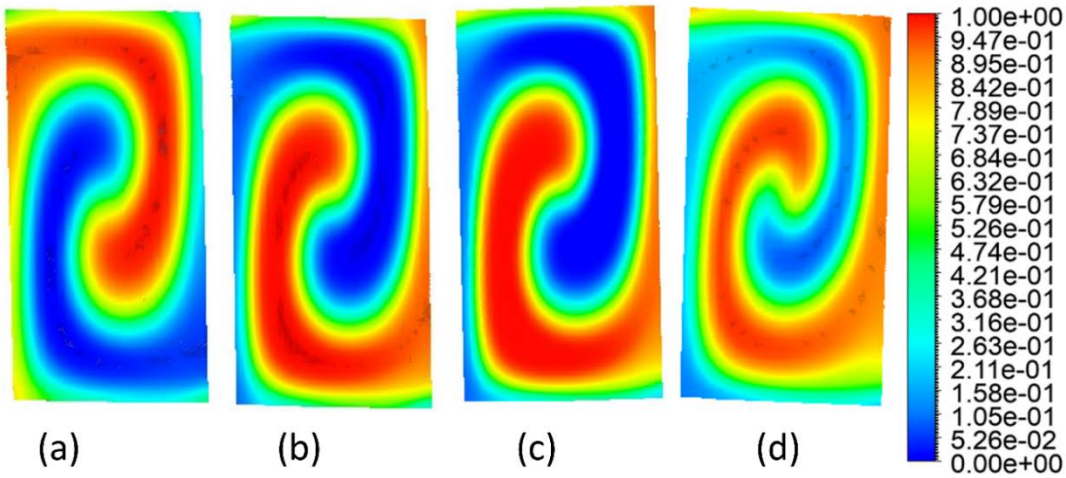

Figure 4.3 The mass fraction at the outlet for different numbers of elements (a) 1000688, (b) 1556088, (c) 2060740, and (d) 3254784.

4.1.2 Non-Newtonian

The validation is based on the earlier findings of (Afzal and Kim 2014) using the identical governing parameters and mixing unit model. This study first establishes the

mixing quality for Newtonian fluid to evaluate the earlier work objectively. Figure 3.4 illustrates the HSTM micromixer schematic. The primary mixing unit, the design domain, is housed in the micromixer. Two inlets supplying a different 1 mol/m^3 concentration or 0 mol/m^3 allow fluid flow into the micromixer. The primary goal is to increase mixing efficiency in the design domain by modifying the flow channel's geometry. At the outflow, the combined fluid is finally received.

It observes the consistency between the results in Figure 4.5. There is a more significant difference in the low-concentration zone. The numerical simulation expected a value near 0.15. Numerous factors, like the numerical mesh, discretization methods, or experimental technique, may be responsible for this discrepancy. The studies of Mainochi et al. and Rahmannezhad and Mirbozorgi also discussed this distinction. It is significant to remember that more mixing is indicated by a flatter profile, which has a more negligible concentration difference (lower standard deviation). The global numerical result agrees well with the experimental findings. For Wang et al. and the current work, the results for mixing percentage were 39.1% and 41.7%, respectively.

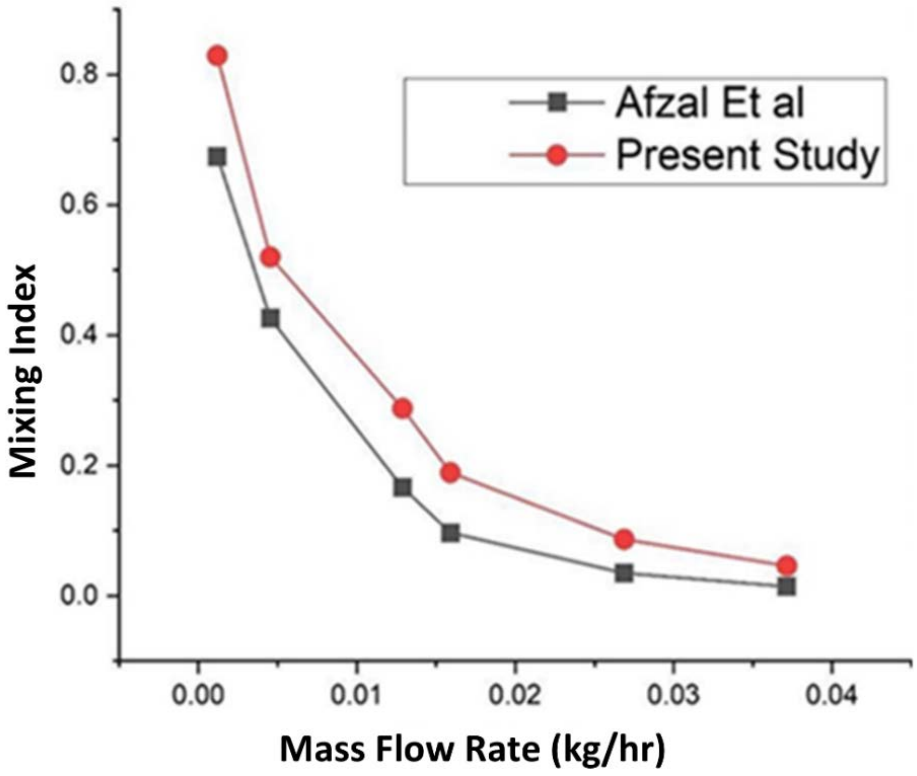

Figure 4.4 Verification of present study with (Afzal and Kim 2014).

To effectively arrange the mesh and capture the flow around the barriers, a prism (inflation) structure was also included. The value chosen for the element size is based on the value used in the Batchelor's Scale methodology-based studies by (Maionchi, Ainstein, dos Santos, and Maurício Bezerra de Souza Júnior 2022; Rahmannezhad and Mirbozorgi 2019). Applying this technique results in an element size value estimate of no more than 6 μm for the works under consideration.

Therefore, the current study employed the value of 2.75 μm as a reference for estimating the mesh element size and applied the GCI approach from this value to suit the specifications of the mentioned research. The pressure differential (ΔP) between the micromixer's inlets and outlet and the mixing percentage (η) values in the outlet portion were subjected to the GCI test. Given that the most significant value obtained in the test (GCIΔP) was 0.701%, demonstrating that the impact of mesh on this variable is minor, it is evident that ΔP is not much affected by mesh refinements. On the other hand, the effect of mesh on η is considerably more significant, amounting to 4.216%. This impact, connected to the techniques used to determine the pressure drop and mixing %, has been noted in earlier research in the literature (Maionchi, Ainstein, dos Santos, and Maurício Bezerra de Souza Júnior 2022). The pressure drop is computed as the area average of a primal variable, the pressure. The meshes may be converged for this variable as they are very well adjusted. However, more points often yield more dispersed findings since the mixing % is determined using the data set's mean and standard deviation. As a result, the solution is more widely dispersed, and a more refined mesh contains more components, which affects how the mixing percentage is determined.

4.2 Numerical Analysis of Twist and Bend Mixing Channel (TBM)

Figure 4.4 shows three TBM simulation cases in Ansys fluent 2022 R1, with 240 total cases (shown in table 4.1 for twist 1 and similarly for twist 2, 3 and 4)) formed with this combination. The training of a neural network was carried out using the TensorFlow library and the findings from the simulations. The global optimization procedure may be carried out using new configurations (changing twist and bend angle) predicted by this NN. This train NN can predict the values of $\Delta P + 1/\eta$ and η

as output variables, using Re, twist angle and bend angle as input variables. This allows the NN to understand the relationship between these variables and produce accurate predictions based on the input data it was trained on. This NN has two hidden layers: [8 3] for the target and [7 4] for target 2 neurons using the 'relu' activation function. The training process involved fitting the data to a specific functional form, representing the relationship between the input and output variables. This application form is used to make predictions based on new inputs and can provide a valuable tool for understanding the underlying relationships in the data. It captures the underlying relationship between the variables and provides a mathematical representation, allowing predictions based on input values. The optimization was carried out with a suitable neural network model to maximise φ and minimize ΔP+1/η. The MFO was used for the multi-objective functions. The entire optimization process is depicted in a flow chart in Figure 3.6. The numerical analysis shows the mass fraction, pressure and velocity profiles in Figures 4.6, 4.7 and 4.8.

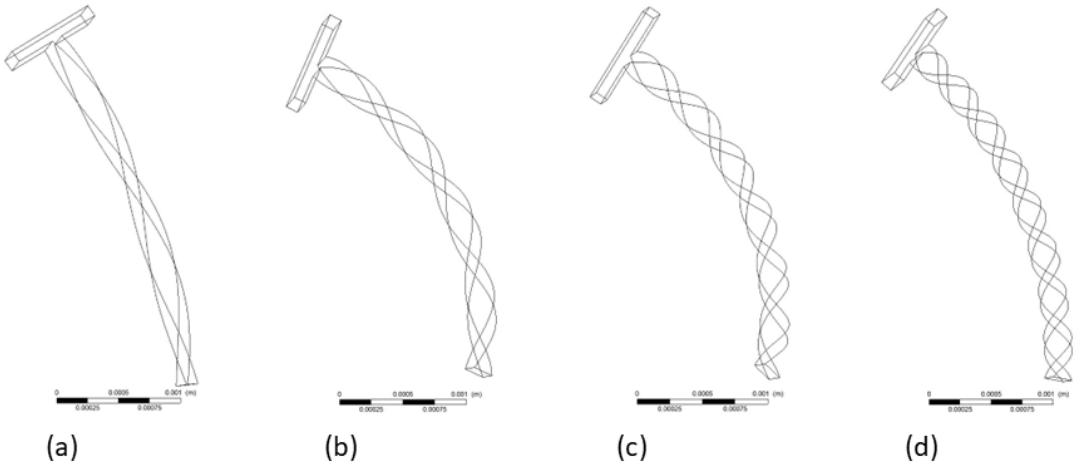

Figure 4.5 Proposed model of hybrid with twists and bend Passive mixer (TBM) with (a) 30^0 bend & 1 twist (b) 70◦ bend & 2 twists (c) 70◦ bend & 3 twists and (d) 50◦ bend & 4 twists

Table 4.1 DOE for Twist 1

Bend	**Re**	**Bend**	**Re**	**Bend**	**Re**
30°	10	50°	10	70°	10

30°	50	50°	50	70°	50
30°	100	50°	100	70°	100
30°	150	50°	150	70°	150
30°	200	50°	200	70°	200
30°	300	50°	300	70°	300
30°	350	50°	350	70°	350
30°	400	50°	400	70°	400
30°	450	50°	450	70°	450
30°	500	50°	500	70°	500

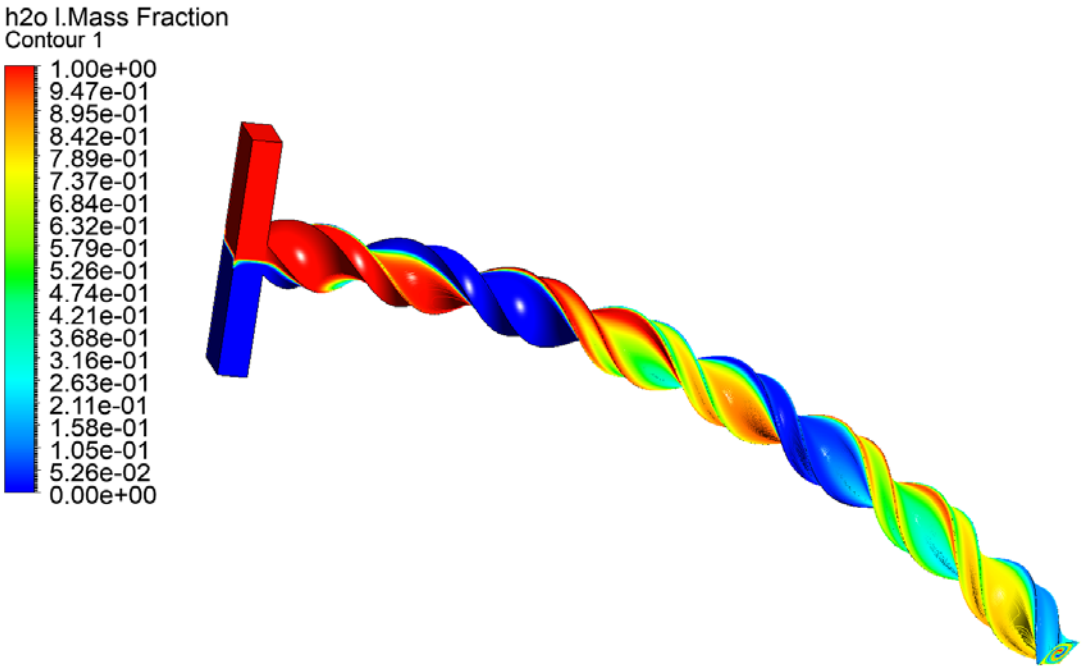

Figure 4.6 Mass Fraction of water and dye of TBM at bend 50^0, twist four and Re 10

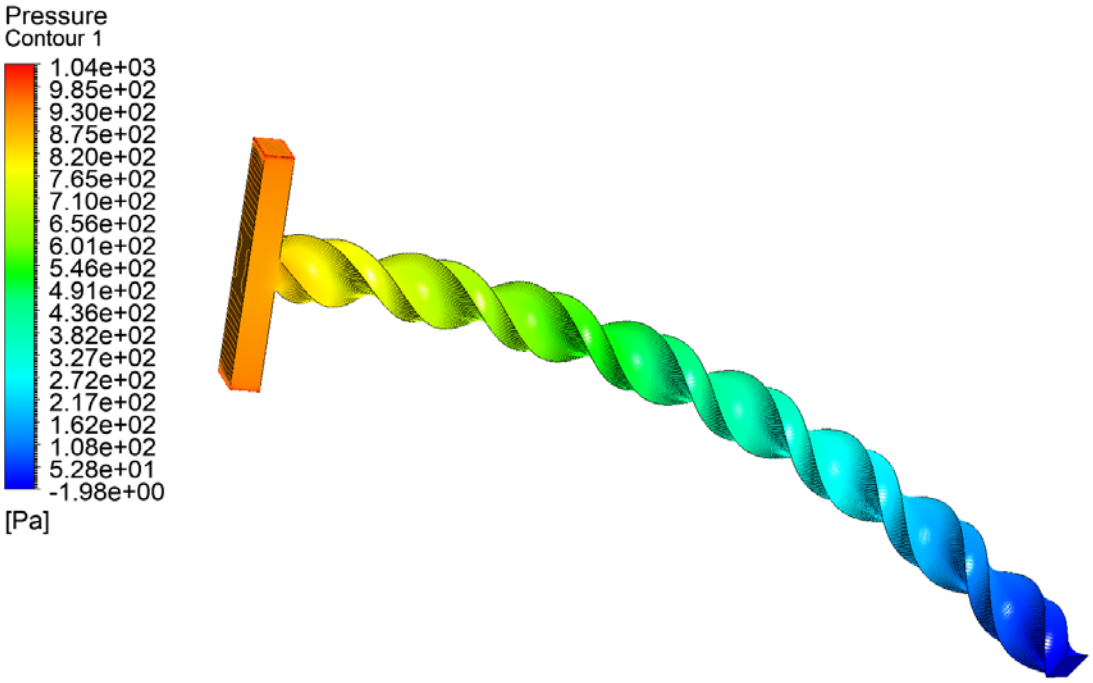

Figure 4.7 Pressure contour of TBM at bend 30^0, twist four and Re 10

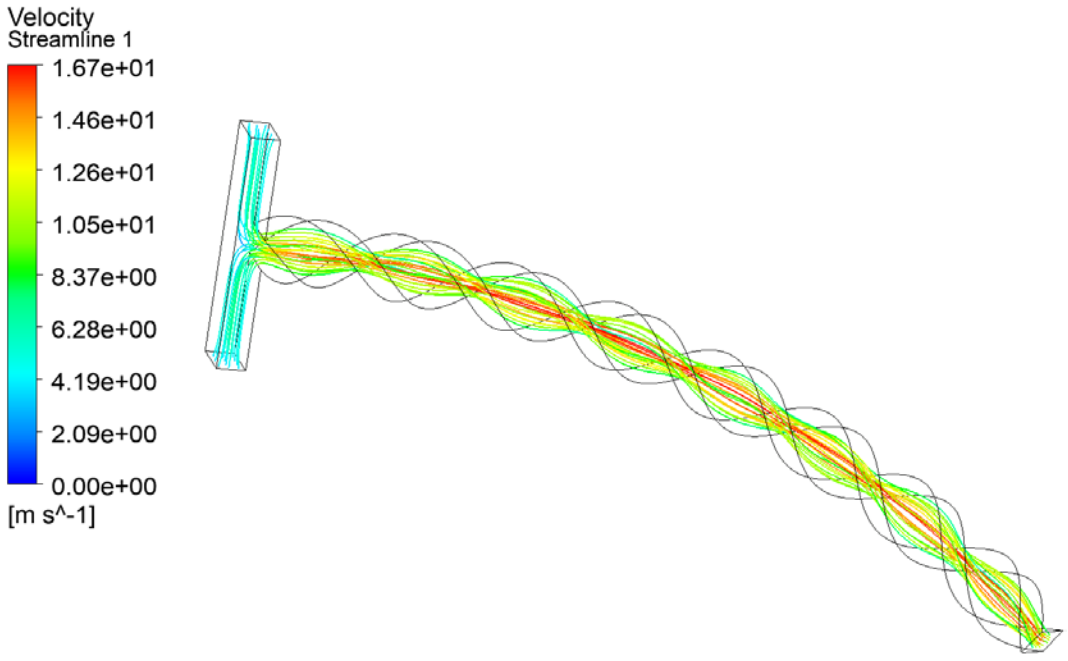

Figure 4.8 Velocity contour from inlet 1 of TBM at bend 50◦, twist four and Re 10

The outcomes demonstrate that the simulated findings and the experimental outcomes are consistent. Furthermore, a comparison is drawn for the transverse velocity, cap region, and flow lines. The computationally generated findings once more displayed

high accuracy in the experimental data. Using equation 3.36, the mixing efficiency (η) was calculated to be 31.5% based on experimental data from (Dundi et al. 2021) and 34.5% based on numerical data obtained in this study. Despite the inherent limitations and disparity in methodology betwixt experiments and simulations, the results obtained from both approaches can be considered to be in reasonably good agreement. The results suggest that the simulations accurately reflect the behaviour and key features of the system and agree with experimental observations, demonstrating the robustness and consistency of the results.

4.2.1 Simulation results

TBM model micromixer simulation results were used to calculate both σ, ΔP and η. These results provide valuable insights into the performance of the micromixer and its ability to mix the solute effectively. These values were then compared to those reported in the literature, and the results showed good agreement and consistency with the expected values. This indicates that the simulations accurately capture the system's behaviour and that the values obtained align with previous studies and system understanding. Interestingly, with twist and bend, η, ΔP, and ΔP+1/η tend to increase, owing to chaotic diffusion. Figures 4.9 and 4.10 depict the correlation of ΔP and script η vs Re for bend and twist, respectively., that is being optimized.

4.2.2 Artificial Neural Network (ANN)

The results in Figures 4. 8 and 4.9 served as the input data for training ANN, creating a predictive model. This model allows for the estimation of the ΔP, η, and ΔP + 1/η, based on a given geometry. This model leverages the relationships revealed in the results to make predictions, providing a valuable tool for understanding the behaviour of the system The data obtained from the simulations were organized and prepared for use in the neural network by including the twist and bend angle as input variables and η and ΔP as output variables. The data was divided into three sets for the training process, with 70% used for training, 15% for testing, and 15% for validation. In addition, the data values were normalized and mapped to a range of 0 to 1. This normalization ensures that all input and output variables have equal influence on the model and are treated equally during training. Table 4.4 shows that the results are

almost the same by varying the weightage of the objective function (η, ΔP). The data architect, trained by ANN, shown in Figures 4.11 (a) and 4.12 (a) for ΔP and η, this data corresponds to better ANN train results with test and validation curves; it is confirmed by error histogram Figure 4.11 (c) and 4.12 (c); training is done until the 4th epoch, with a value of 0.050547 for ΔP, and the 3rd epoch, with values of 0.32049 for η; Figures 4.11 (b) and 4.12 (b) shows validation performance; Figures 4.11 (d) and 4.12 (d) show ANN training state with gradient values of 1.8422e-10 at 3rd epoch and 317.322 at 6th epoch for ΔP and η, respectively.

Creating the neural network (NN) involved defining its architecture, for which an artificial neural network was selected. Monitoring the model for overfitting is crucial, which is a higher training error than a validation error can identify. This can be done by observing the training and validation curves. Once the model is trained, test data can be used to validate the performance of the NN. The results showed a mean square error of less than 3% for the pressure drop prediction and less than 1% for the prediction of η. The results from the simulations performed using Ansys fluent 2022 r1 and the values predicted by the neural network based on twist and bend values.

The evolutionary algorithm is run after the appropriate objective function has been specified. It is crucial to clearly define the parameters for this algorithm, including the population size and the number of iterations, as they play a significant role in determining the algorithm's performance and overall outcome. To find the maxima of the objective function, one only needs to invert the output signal by making it negative.

4.2.2.1 Optimization and validation with simple T-Micromixer

The optimization process started with MFO (Multi-Objective Function Optimization), which enables the definition of multi-objective functions. Three optimization cases were considered, involving maximizing and minimizing (i) η, (ii) ΔP, and (iii) ΔP + 1/η. The objective function used with the neural network model developed was a combination of ΔP and 1/η, represented mathematically as ΔP + 1/η. This function was chosen as the target to optimize for the desired outcome. This objective function was selected based on various factors, such as the nature of the problem being solved,

the available data and resources, and the system or application requirements. This objective function aims to balance two opposing factors, ΔP and 1/η, representing the inverse of the golden ratio, to reach a compromise solution that optimizes performance. This objective function has proven effective in obtaining accurate and reliable results from the developed neural network model. A penalty value is added to the function's output if the relationship between the inputs and outputs is unsatisfied. The penalty should be significantly more significant than those typically achieved at the exit to guarantee that this condition is far from the function's minimum.

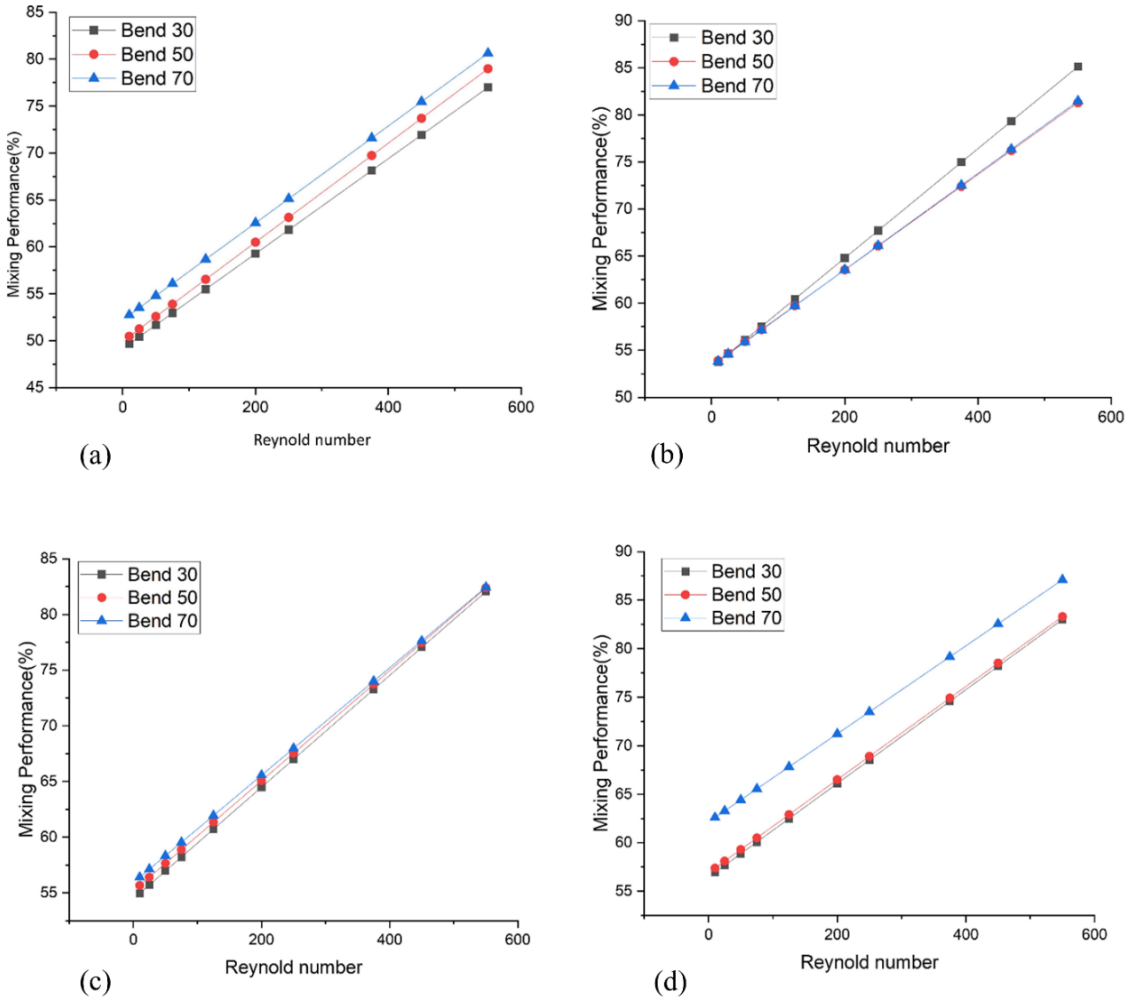

Figure 4.9 Simulation results η vs Re for bend at a) Twist 1 b) Twist 2 c) Twist 3 and d) Twist 4.

Table 4.2 Optimization results with the highest value

Obfn	Maximum	η	ΔP (Pa)	Twist	Bend Angle	Re
η	79.76	79.76	-	3	70°	550
ΔP (Pa)	1043	-	1043	4	70°	550
$\Delta P_s+1/\eta_s$	5.3971	61.551	19.78	4	70°	10

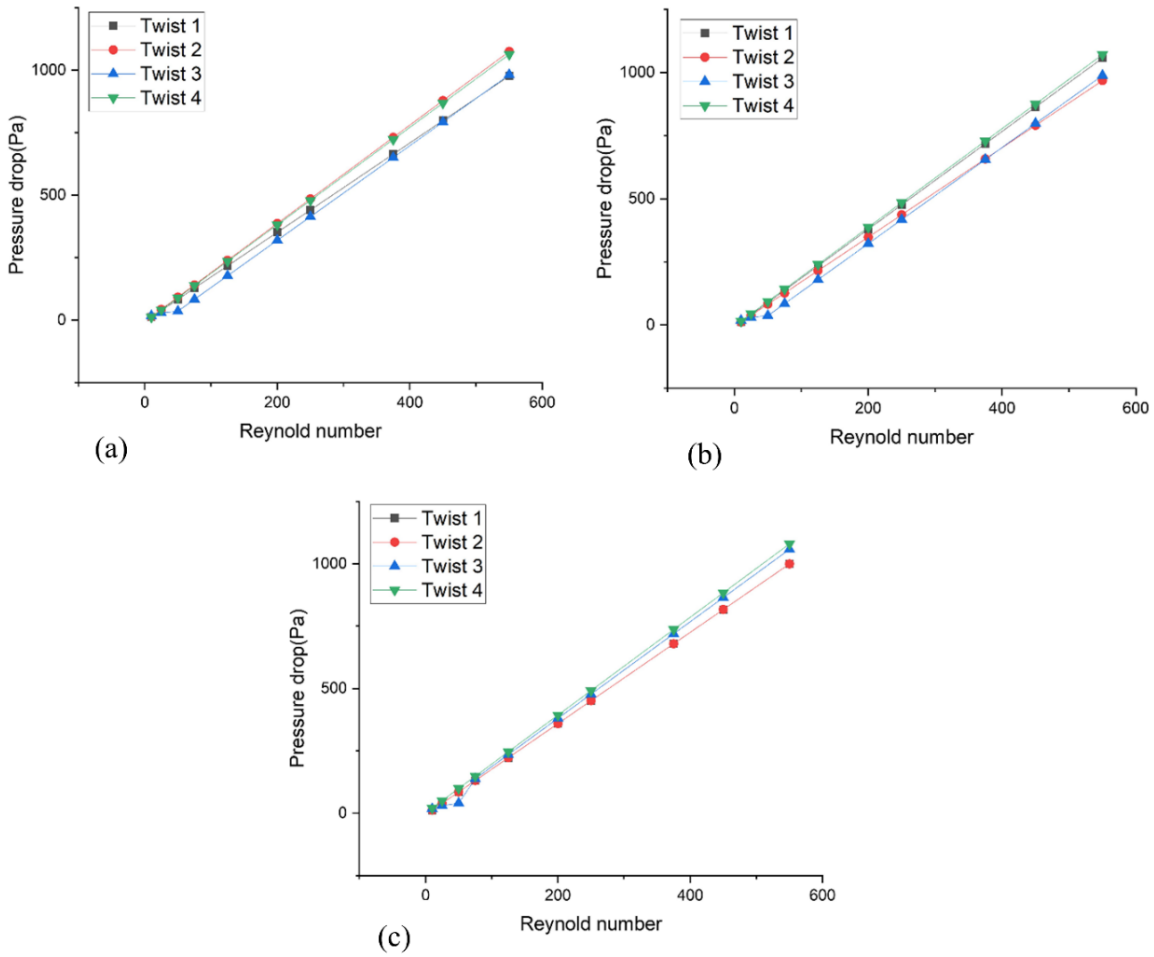

Figure 4.10. Simulation results η vs ΔP for twist at (a) bend 30◦, (b) bend 50◦ and (c) bend 70◦

The optimisation results, including the values of the objective functions and the corresponding twist and bend values, are displayed in Tables 4.2 and 4.3. It was observed that the maximum values for twist and bend are almost identical for all three

objective functions, namely η, ΔP, and ΔP+1/η, with the values being four and 70°. However, it is worth noting that the values for η and ΔP are significantly lower compared to the value of ΔP+1/η, which was found to be 17.9687. This implies that minima of ΔP+1/φ lead to nadir value for both ΔP and η, but not for maxima. Thus, we can apply the objective function to achieve the high value for η and a nadir value of ΔP simultaneously, as the maximum value of ΔP+1/η does not result in nadir values for both ΔP and η.

Table 4.3. Optimization results with the lowest value

Obfn	**Minimum**	**η**	**ΔP (Pa)**	**Twist**	**Bend Angle**	**Re**
η	51.302	51.30	-	1	10°	10
ΔP (Pa)	17.25	-	17.25	2	15°	10
ΔPs+1/ηs	17.96	55.71	17.95	3	15°	15

The optimization process utilized a Multi-objective Function Optimization (MFO) approach, which allowed the definition of multiple objectives. Three different optimization scenarios were considered, each focusing on either maximizing (i) mixing percentage (η), (ii) pressure drop (ΔP), or (iii) ΔP+1/η. For example, ΔP+1/φ was selected as the objective function, and the developed neural network model was used to predict the values of twist and bend as inputs, with the outputs serving as the function's objective. A penalty value was added to the function's output if the desired relationship between inputs and outputs was unmet. The optimization results refer to the application of the objective, either 1/η, ΔP, or ΔP+1/η. It was observed from the results of Figures 4.8 and 4.9 that both η and ΔP increase with the increase in the values of twist and bend.

The aim is to find the twist and bend simultaneously in order of optimized conditions of maximum mixing performance (η), and minimum pressure drop (ΔP) that can't be achieved through the method mentioned earlier. To address this, a multi-objective optimization algorithm based on MFO was used with the help of the Platypus library in Python. The three objective functions (maximizing η, minimizing ΔP, and

minimizing ΔP+1/η) were defined and considered, along with the previously used restriction condition. To determine the range of potential values for the input variables, the restriction on the output of the objective function was updated while also considering the number of objective functions, input variables, and restrictions. Finally, a feasible solution was processed by eliminating odd ones.

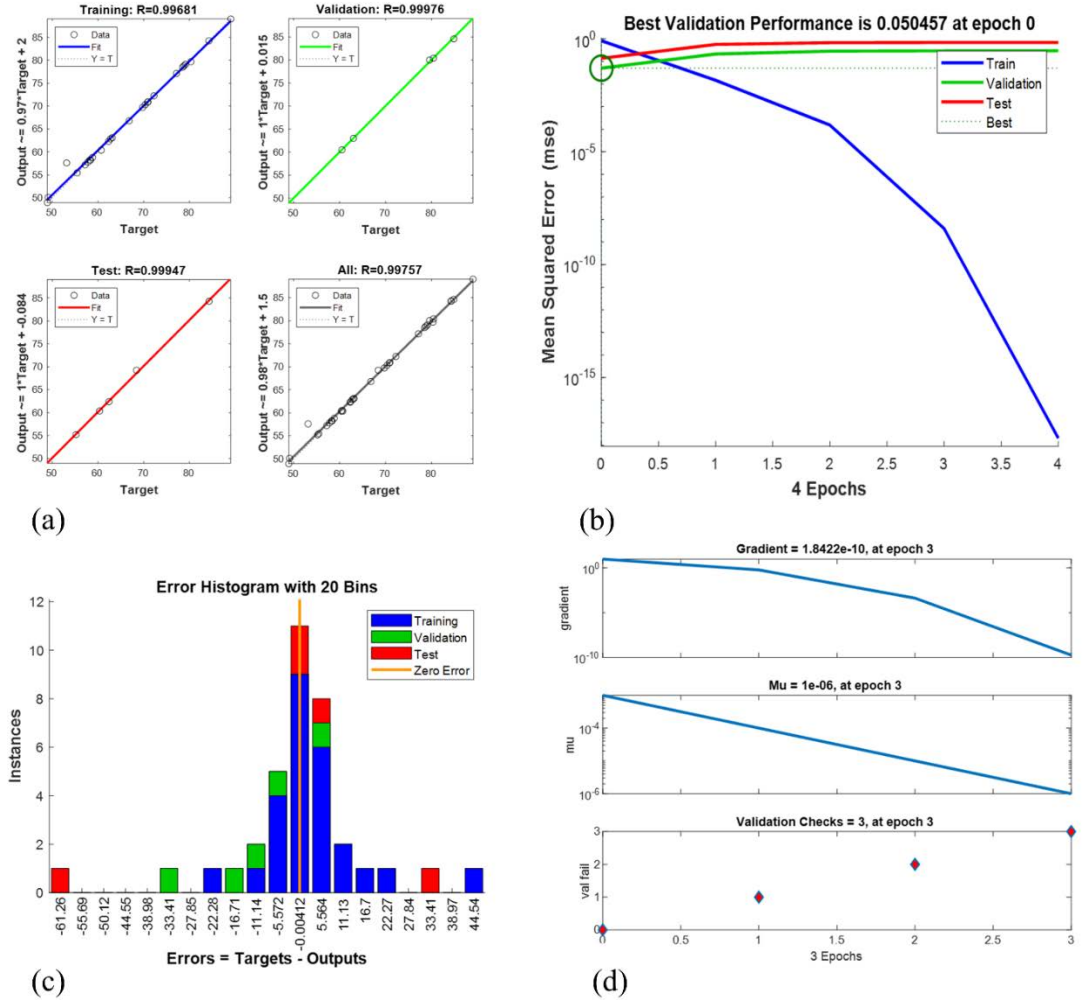

Figure 4.11 ANN Training plots for η: (a) regression Performance for trained ANN (b) variation of error with epochs (c) Error histogram plot (d) training state of ANN.

The correlation between φ max and ΔP max was found. Similarly, the relationship between ΔP min and the lowest value of φ was discovered. In this study, we consider, besides the optimal point obtained from the minimum of ΔP + 1/η, the points with the minimum of ΔP + 1/η and the maximum of η. The twist and bend values corresponding to the minimum ΔP + 1/η were obtained. In this region, ΔP decreases

while η remains high, as previously reported in (Dundi et al. 2021). This optimized geometry aligns with the expected results, with the twist and bend values.

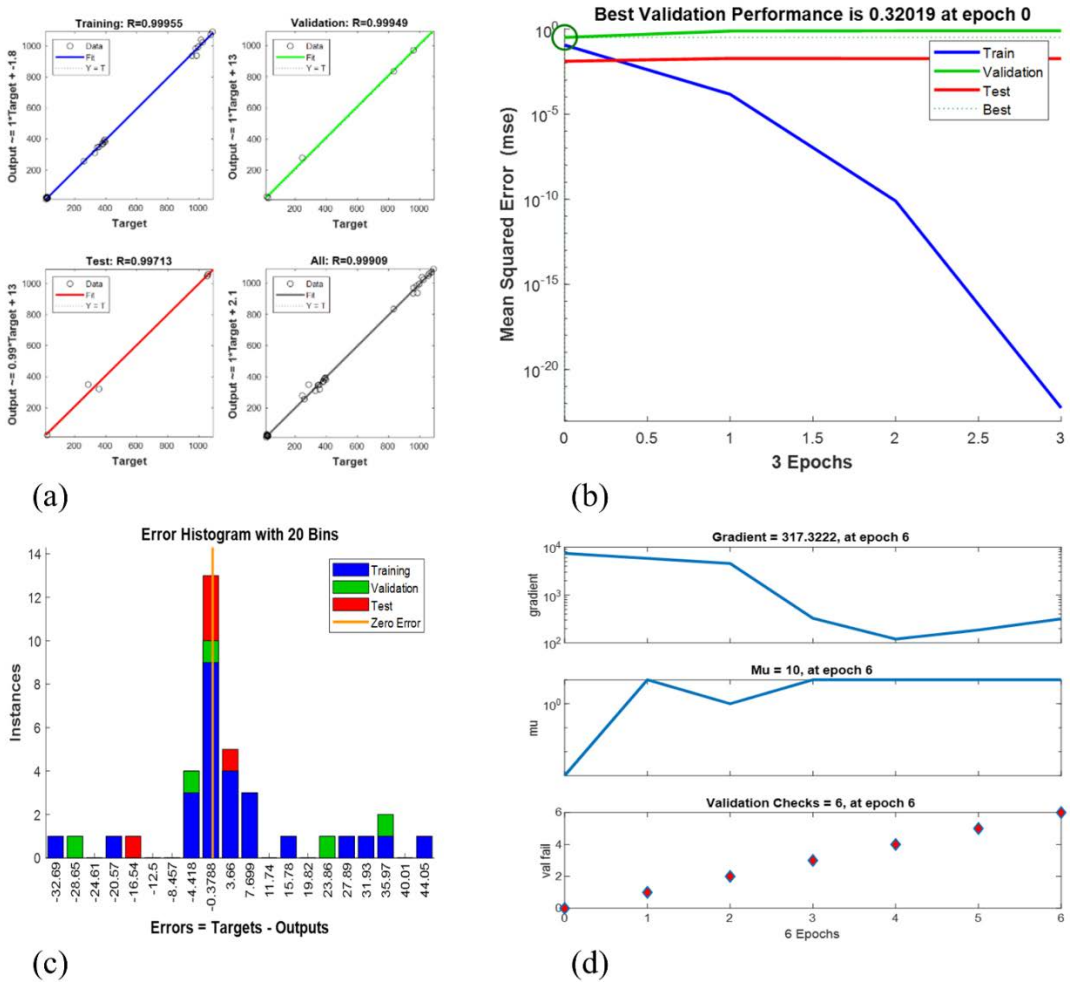

Figure 4.12 ANN Training plots for ΔP: (a) regression Performance for trained ANN (b) variation of error with epochs (c) Error histogram plot (d) training state of ANN.

The results of the optimization showed that the errors for the prediction of η, ΔP, and ΔP+1/η were found to be 0.56%, 2.78%, and 3.63%, respectively, for the optimized case. These results are highly accurate, particularly for the optimized case, where the predicted values of η and ΔP are very close to the actual values. The error in the maximum and minimum cases is as follows:

Table 4.4 Comparing values obtained from optimization and simulation for TBM.

	Twist	**Bend**	**Re**	**η**	**ΔP (Pa)**	**ΔP+1/η**
Simulation	4	70°	10	79.31%	17.426	17.32
Optimal	4	70°	15	79.76%	17.925	17.98

attributed to the limitations of the multi-variable optimization method used. A comparison of best data obtained from simulation and optimization for η and ΔP is summarized in Table 4.4. Table 4.5 shows the influence of the weight function of the objective for the optimized results.

Table 4.5 Optimization results with weightage to output variable for TBM model.

	Weightage					**Optimized Result**	
Cases	η	ΔP	Twist	Bend (^{o})	Re	η (%)	ΔP (Pa)
1	0.5	0.5	4	70°	11.858	61.408	17.952
2	0.4	0.6	4	70°	10	61.2927	17.952
3	0.3	0.7	4	70°	10	61.2927	17.952
4	0.7	0.3	4	70°	16.995	61.7078	17.952
5	0.6	0.4	4	70°	14.320	61.551	17.952

4.3 Numerical Analysis of Offset Twist and Bend Micromixer

In this study, numerical simulations of OMTB micromixers (Figure 4.13) built for Re in the range of 0.05 to 450 at various geometric parameters were carried out.

4.3.1 Effect of Re on η

The most crucial parameter in the microchannel is the velocity with which the fluids were fed, which is considered as the Reynolds number, η at different Reynolds values, which is displayed through the micromixer in Figure 4.14.

Due to the low velocity at Re = 0.05, there is a significant residence time. Only molecular diffusion (N_A) can mix fluid particles. When the molecule diffusion channel is shortened, mixing is greatly accelerated. For Re = 5, the molecular diffusion

process still produces mixing, but because the residence period is shorter than it is for Re = 0.05, molecular diffusion slowed down.

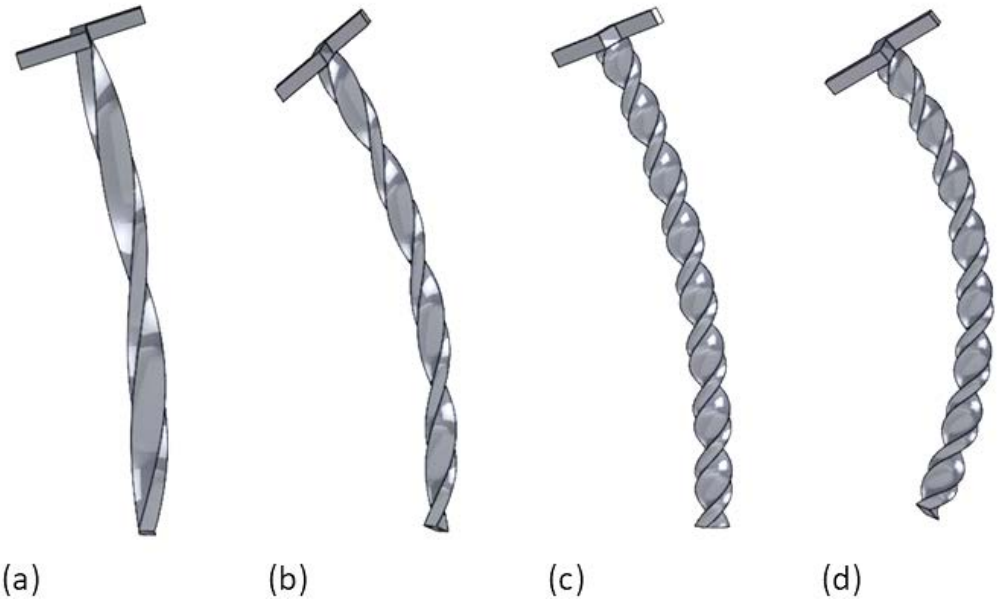

Figure 4.13 Proposed model with different combinations of bend and twist a) 1 twist and 30^0 bend b)2 twists and 50^0 bend c) 3 twist and 30^0 bend d) 4 twist and 70^0 bend

Rapid mixing results from the convection process and inertial force defeating molecular diffusion from Re 5. Re can be increased as much as possible without affecting the mixing rate. Because molecular diffusion is reduced at Re = 1 and mixing is diminished. As a result, the mixing region between the two fluids is smaller, which accounts for the difference between mixing at Re = 0.05 and Re = 5.

While achieving a favourable η at high Reynolds numbers is favourable, the significant ΔP associated with these values is undesirable. Surprisingly, mixing performance for Reynolds numbers of 0.05 and 100 is nearly identical.

4.3.2 Effect of bend and twists on mixing performance

This research aims to determine how a twisted mixing channel with a bend affects an offset T-junction micromixer's performance. Micromixer models that have offsets with varied turns in twist along mixing channels (1 - 4) and bend angles (30° to 70°).

For higher $L_m/D_h = 20$,, the simple T-channel exhibits negligible secondary flow. Still, the channel having the bend and twist exhibits secondary flow that is detectable

and increases with twist and bend. Bends can cause centrifugal forces that push fluids toward the outer edge of the curve, creating secondary flow patterns that enhance mixing across different fluid layers. Conversely, twists can induce rotational or helical flows, which help stretch and fold fluid interfaces, increasing the interfacial area and improving mixing efficiency. These effects are more pronounced in microfluidic environments, where laminar flow dominates, and even slight geometric changes can lead to significant mixing enhancements due to the increased influence of viscous forces over inertial ones.

The analysis of ΔP is of utmost importance as it signifies the pumping energy needed to sustain the flow within the micromixer. A low ΔP is essential for ensuring an efficient micromixer. Figure 4.14 compares ΔP and presents the results for each micromixer at various Re. It is observed that in all the micromixers, the ΔP increases with Re.

Figure 4.16 illustrates the mass fraction along the micromixer. The fluid flow of particles along the micromixer for the offset geometries is depicted in Figure 4.17. The tracking line, however, begins to bend around the micromixer after twisting is included. The impulsiveness intensifies as the bend and twist of mixing channels rise. Figure 4.18 shows the mass fraction at the outlet of OMTB, such as for (a, b and c) for bend 30°, (d, e and f) for 50°, and (g, h and i) for 70°, for twists 2, 3, 4, respectively.

Convective and diffusion mass transfer are the primary mixing mechanisms in the passive micromixer. Diffusion would be the primary factor controlling mixing performance without the secondary flow the twisted mixing channel creates in the micromixer. Convective mass transfer becomes essential for the micromixers with bend and twist because of the increased secondary flow, which eventually leads to more excellent mixing performance.

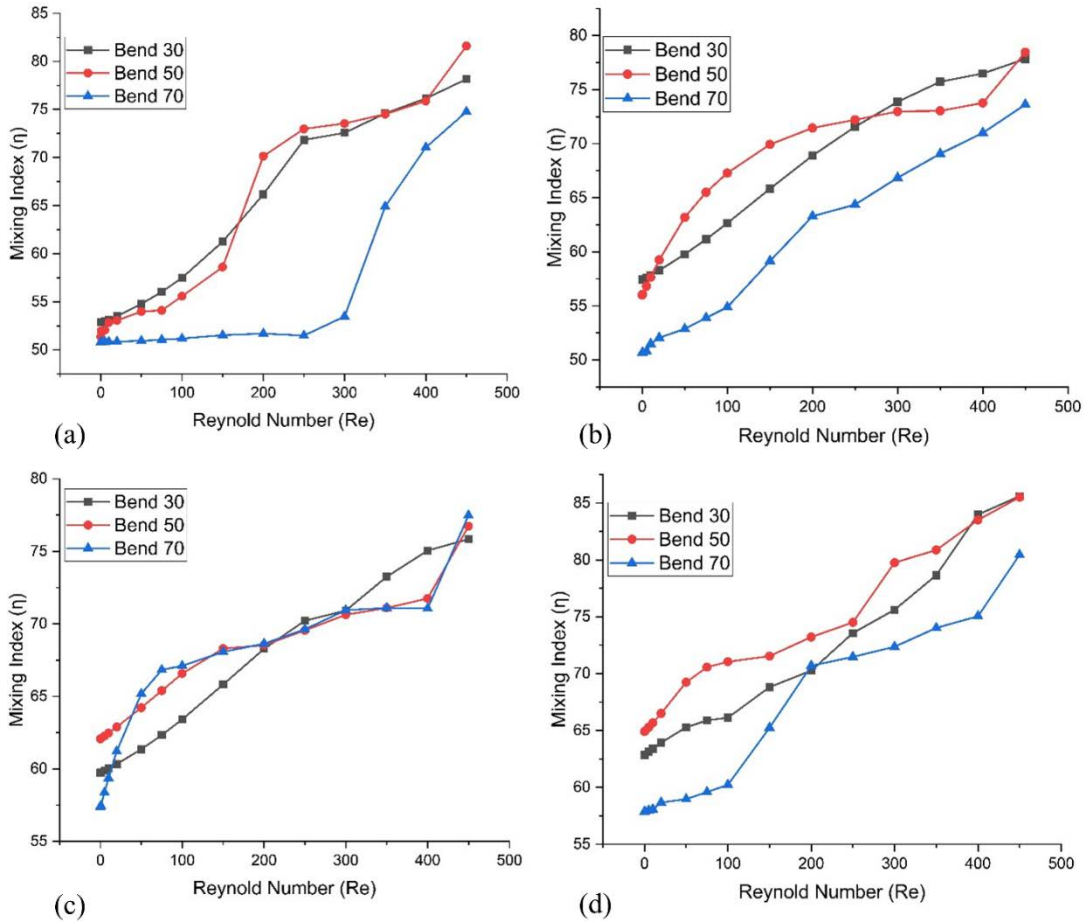

Figure 4.14 η vs Re for Twists (a) 1, (b) 2, (c) 3 and (d) 4.

As demonstrated, micromixers with twisted mixing channels perform better than their counterparts with no twist, especially between Reynolds numbers of 0.05 and 100. The mixing index shows a pronounced improvement in the range of Re from 0.05 to 450. Additionally, the twisting and bending-induced secondary flow is prominent here, mimicking the improved blending of micromixers.

Increased twist in a flow leads to more significant disruptions, resulting in improved mixing rates due to the addition of advective effects to laminar flow. ΔP in the micromixers increase after the introduction of whirling, which also improves mixing. the ΔP and associated η were investigated for the microchannel with twists and bend

channels at the specified Re. The rate of pressure decrease is only minimal despite the significant improvement in the η for Re at its mid-range.

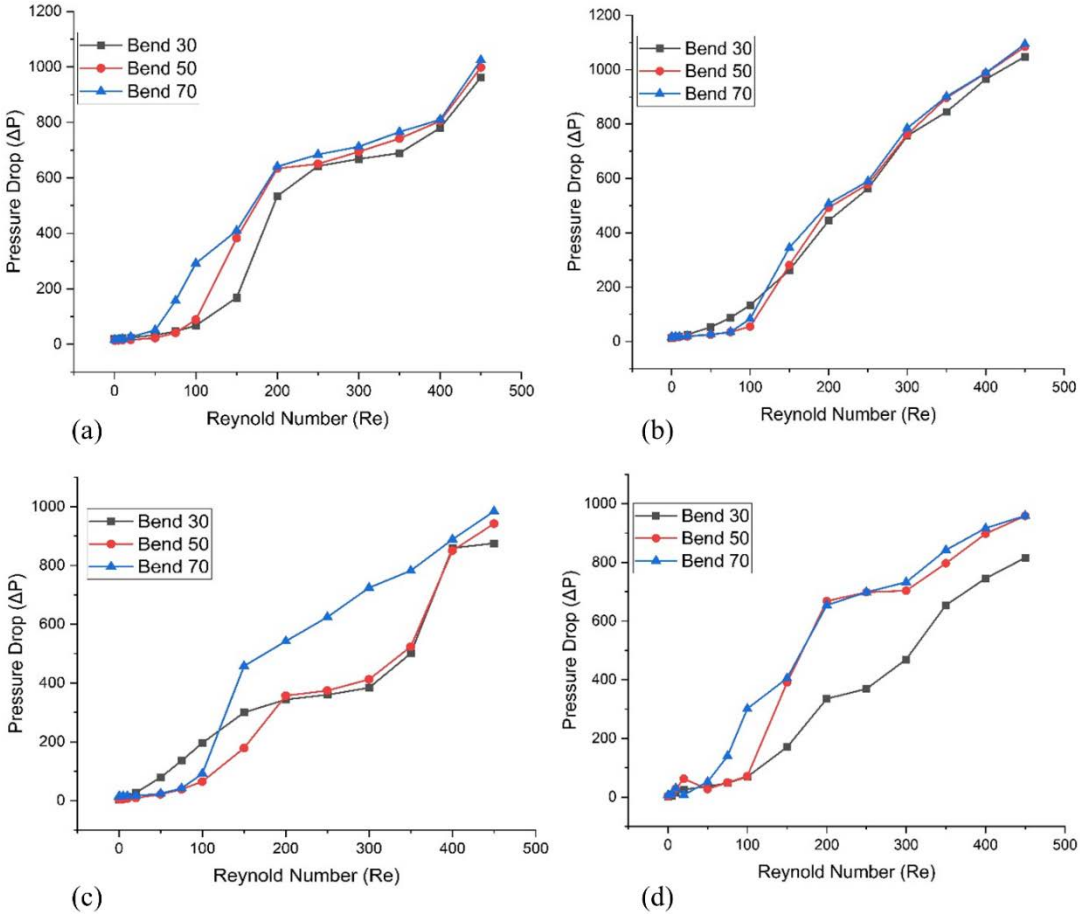

Figure 4.15 Δ*P* vs Re for Twists (a) 1, (b) 2, (c) 3 and (d) 4.

Increased twist in a flow leads to more significant disruptions, resulting in improved mixing rates due to the addition of advective effects to laminar flow. ΔP in the micromixers increase after the introduction of whirling, which also improves mixing. the ΔP and associated η were investigated for the microchannel with twists and bend channels at the specified Re. The rate of pressure decrease is only minimal despite the significant improvement in the η for Re at its mid-range.

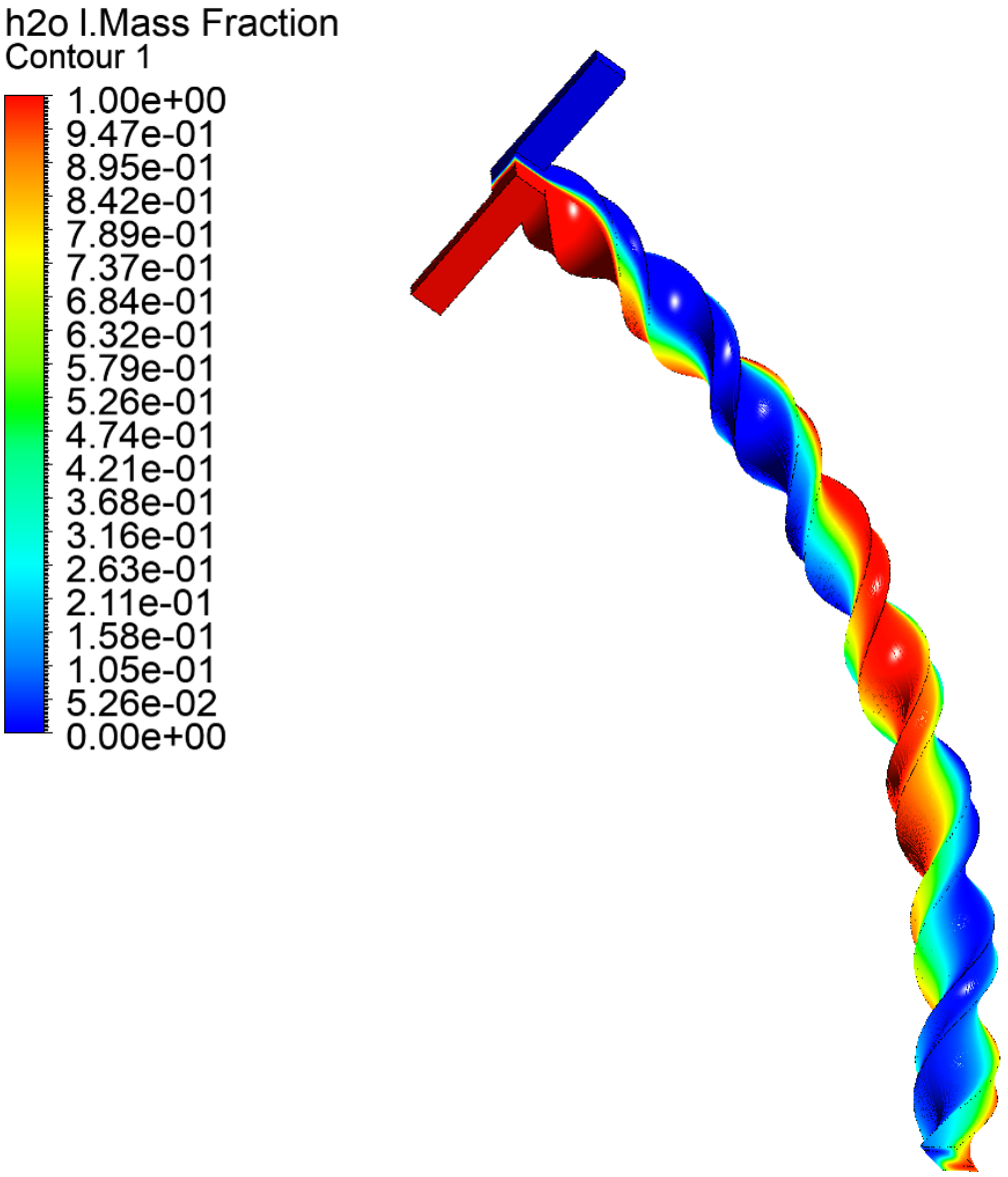

Figure 4.16 Mass fraction contour of OMTB

Consequently, especially for the micromixer with an increased number of twists, a notable enhancement in performance is observed within the intermediate range of Re (betwixt 0.05 and 450). This performance improvement index correlates with the mixing magnification achieved per unit increase in ΔP penalty. As demonstrated, introducing bending and twisting to micromixer channels can sometimes improve the

performance index by more than three times, suggesting the potential of OMTB microchannel applications in the industry.

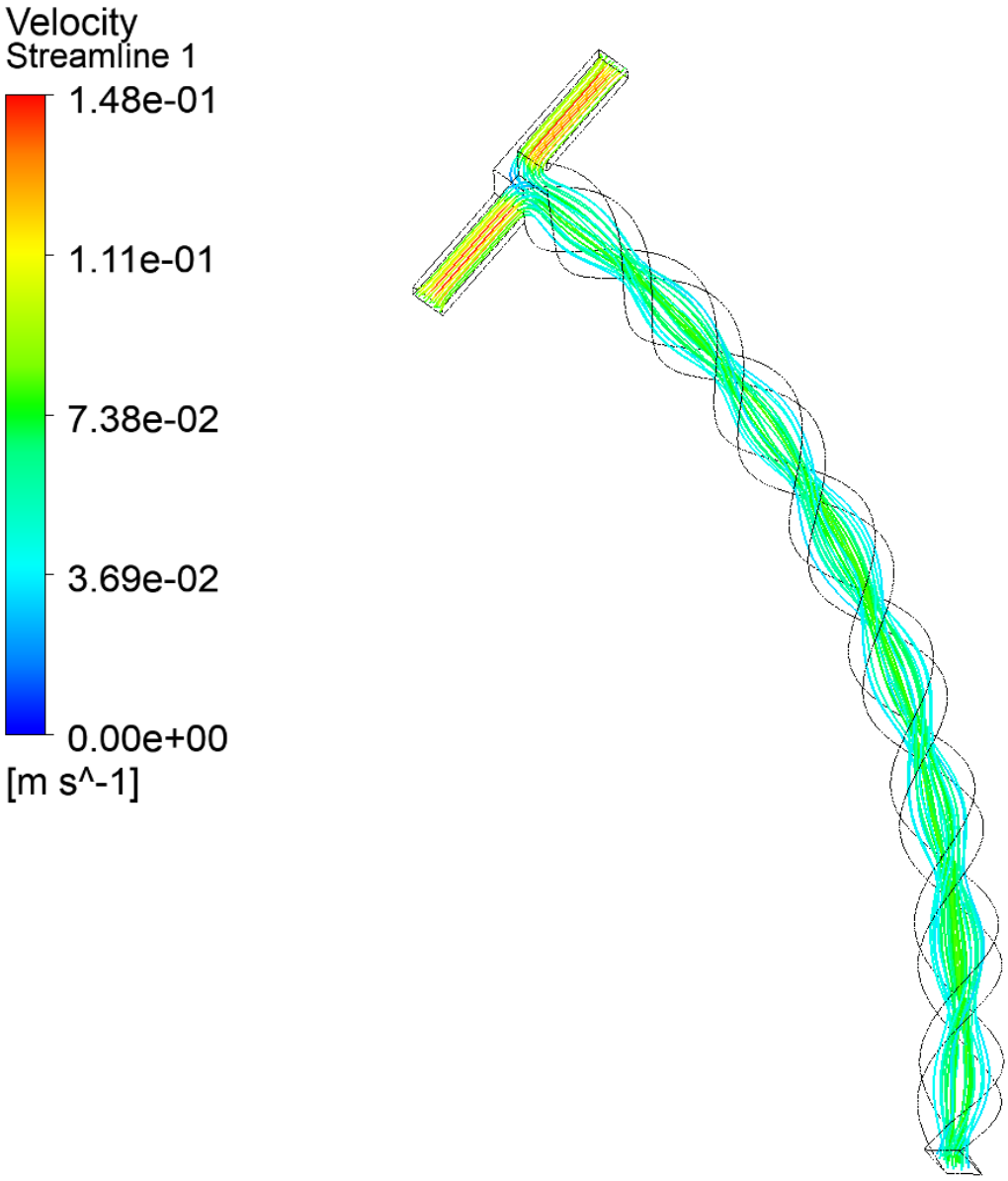

Figure 4.17 Velocity Streamline across OMTB

The results indicate no recirculation downstream due to the low inertia in the flow, with a Reynolds number (Re) of 0.5. The curve occurs due to twists and bends in the streamlines, which causes a change in velocity direction. This phenomenon is crucial for effectively mixing substances, as it facilitates the movement of one material towards another. Table 4.6 compares the TBM micromixer with offset and without

offset and it is clear that with offset mixing efficiency is more and pressure drop is less.

Table 4.6 Comparison of model with and without offset Micromixer model

	Twist	Bend	Re	η	ΔP (Pa)	ΔP/η
No Offset (Mustafa, Zunaid, and Gautam 2023)	4	50°	450	85.512%	998.06	1167.15
With Offset	4	60°	400	87.76%	974.20	1109.86

The concentration profiles at the micromixer's intake suggest that the mixing between the two fluids is adequate close to the channel's inlet, according to the data. Upon reaching the first twist, a minor disruption in the flow ensues, resulting in an augmentation of its viscosity. The intensity of this process increases as the mixture passes through the "mixing unit" (a configuration of barriers), resulting in increasingly pronounced disruptions in the flow. At the second twist, the mixing is more substantial than the first, indicating the impact of the impediments on the species mixing.

Observing the outlet area shows that the central axis interface is green, which signifies a complete mixing process (100%). In contrast to the original region, there are no longer distinct areas consisting solely of one species (red or dark blue). Instead, there is now a gradient of mixed species across the cross-section of the channel.

The disparity between the η and ΔP values acquired at the ideal locations from the response surfaces through simulation is minimal, particularly for η. In contrast, ΔP Although it remains satisfactory, it exhibits more pronounced disparities, even when employing more accurate measurements, as depicted in Figure 4.11. The schematic demonstrates that the channel length of each micromixer design varies according to the increased twists and bends. Thus, the localised pressure dips are more evenly spread.

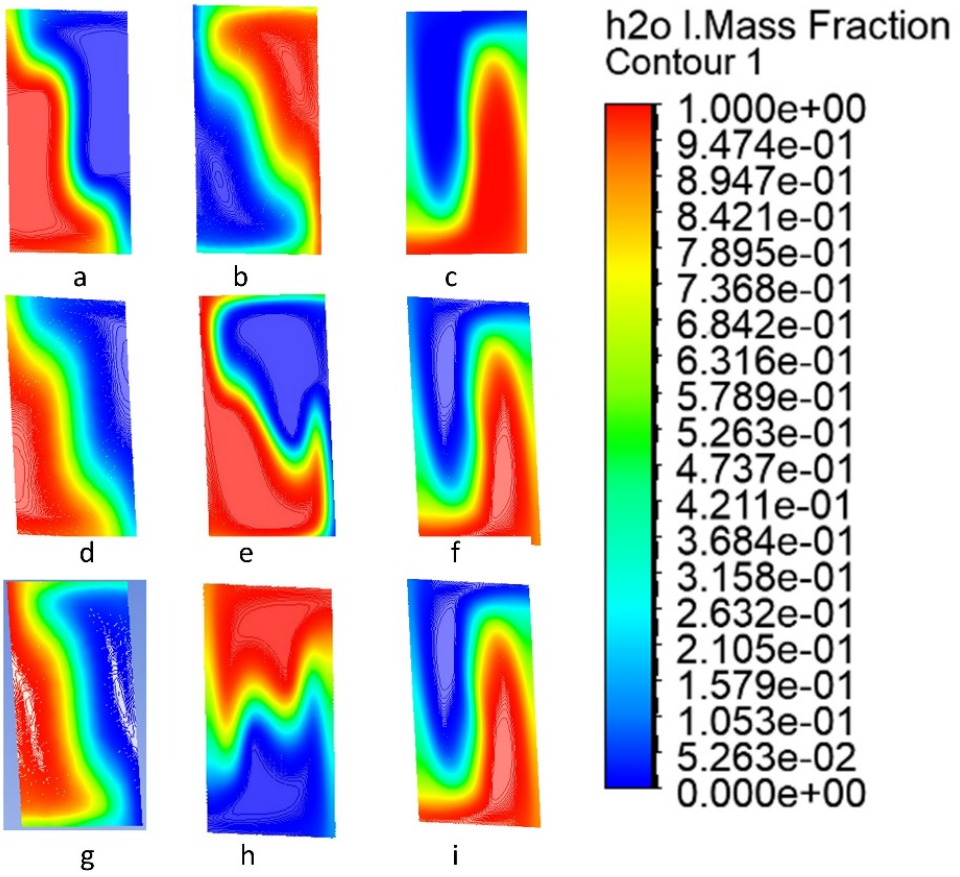

Figure 4.18 Mass fraction contour of OMTB at the outlet

4.3.3 Optimization

The goal is to concurrently determine the twist and bend that will provide the best possible circumstances for optimal mixing performance (η) and minimal pressure drop (ΔP), which cannot be attained using the previously outlined technique. The Python Platypus package implemented a multi-objective optimization technique based on HHO. Along with the previously employed limitation condition, the three-goal functions (maximising η, minimising (ΔP and $^{\Delta P}/_{\eta}$)) were defined and considered. With output limitation from the objective, the number of objectives and constraints are considered to calculate the various input variables. Finally, by removing the strange ones, a workable answer was developed.

4.3.3.1 *RSM modelling*

RSM subsequently helps to equate the impact of variables and their relationships on the outcomes. The upper and lower limits of the input parameters are presented to the RSM, along with the selection parameters shown in Table 4.7. The recursive behaviour between the variables for bend and twists and how they impacted the η and ΔP is shown in Figures 4.19 and 4.20. For all bend and twist values, the η increases with increasing Re. By analysing the charts in Figure 4.14, it can be deduced that a decrease in Re in all values of bend and twist leads to a fall in ΔP and that reducing bends and twists also prevents the pressure drop from growing, which is the optimum situation for micromixers. Figure 4.20 shows the objective desirability with the input variable (twist, bend and Re).

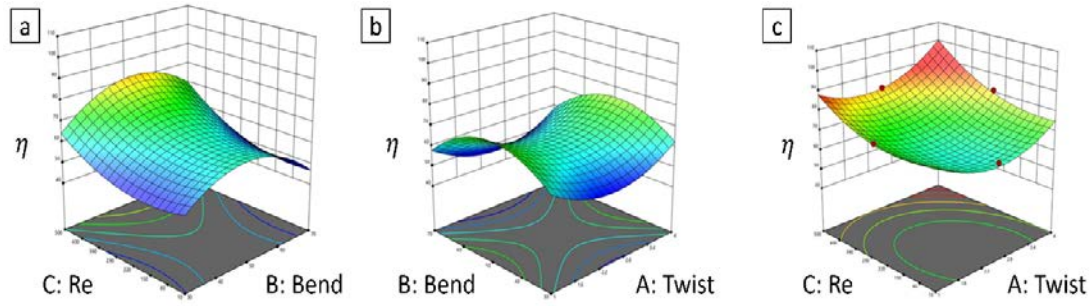

Figure 4.19 Surface response effect for η a) Re & bend b) Bend & twist c) Re & twist

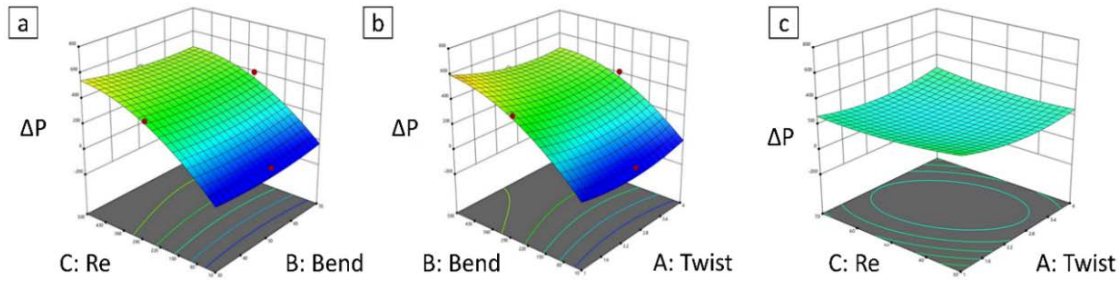

Figure *4.20* Surface response for ΔP a) Re & bend b) Bend & twist c) Re & twist

The ANOVA Table 4.8 model for the output parameter is statistically significant, with P-values less than 0.05 for both the model and the current inputs. All output responses had high R2 and adjusted R2 values, indicating that the model provides data that is very similar to the experimental data. The adj. R2 and Predicted (Pred.) R2 values

were less than 2% for all replies, showing high prediction reliability. The lack of fit is insignificant as the P value is more prominent than 0.05.

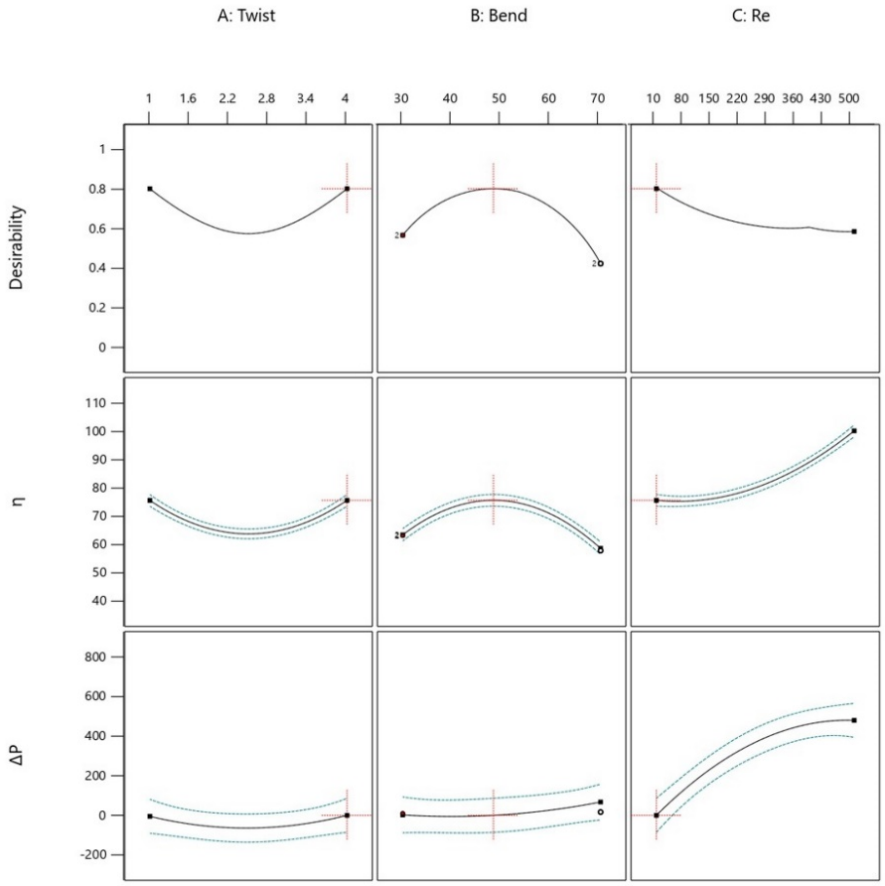

Figure 4.21 All factors desirability of RSM

Table 4.7 DOE with responses

Twists	Bends	Re	η	ΔP
4	70°	10	57.8	16.78301
2.5	70°	255	52.2336	696.8079
2.5	50°	255	55.9549	362.1438
1	30°	450	70.92	1020.14
1	30°	10	58.3499	12.7164
4	70°	450	89.02	528.6035

2.5	50°	255	55.9549	362.1438
1	50°	255	82.2306	447.0021
2.5	50°	10	69.5533	12.71834
4	30°	10	63.12	12.73183
4	50°	255	87.3669	680.9073
1	70°	10	58.36	12.81532
2.5	30°	255	71.2162	402.6061
2.5	50°	450	82.6814	477.5227
1	70°	450	76.3117	532.9106
4	30°	450	80.3	479.4351

Table 4.8 ANOVA F-value and p-value for η and ΔP

Source	**η**		**ΔP**	
	F-value	p-value	F-value	p-value
Model	458.48	< 0.0001	64.91	< 0.0001
A-Twist	245.70	< 0.0001	6.31	< 0.0001
B-Bend	20.59	< 0.0001	1.80	< 0.0001
C-Re	1240.73	< 0.0001	537.55	< 0.0001
AB	14.08	0.1386	2.59	0.1386
AC	7.48	0.0211	7.46	0.0211
BC	164.58	0.3472	0.9728	0.3472
Std. Dev.	0.7160		36.69	
Mean	69.12		316.15	
C.V %	1.04		11.60	

R^2	0.9976	0.9832
Adjusted R^2	0.9954	0.9680
Adequate Precision	78.9605	28.4307

4.3.3.2 *Artificial neural network (ANN)*

The dataset was formed using the simulation results shown in Figures 4.14 and 4.15 for ANN training, creating a prediction model. The twist and bend angles were included as input variables, and η and ΔP were included as output variables to organise and prepare the data collected from the simulations for use in the neural network. The data was split into three sets for the training process, with 70% being utilised for training, testing 15%, and validation 15%. This distribution makes the input and output variables handled similarly during the training process with an equal impact on the model. Figures 4.22 and 4.23 show the linear fitting with R^2 values 0.95529 and 0.97209 for η and ΔP, respectively. Linear fit graphs show the link between observed and expected values. In our case, observed values are taken from simulations, while predicted data are gathered from the HHO response surface. The proximity of our observation sets to this line indicates good accuracy in responding to areas.

4.3.3.3 *HHO modelling*

The HHO optimization process involves five phases: Initial Population, Fitness function, Selection, Crossover, and Mutation. The HHO is responsible for evaluating and choosing the solution based on the objective function derived from the ANN.

With a trained dataset (using ANN), multi-objective function optimization was enabled using HHO. Mainly, three obfn were formulated for optimization, i.e., i) $1/\eta$, ii) ΔP, iii) $1/\eta + \Delta P$ and iv) $\Delta P/\eta$. The performance index (PI), denoted as $\Delta P/\eta$, is a measure that specifically pertains to the cost associated with mixing, also known as the mixing cost (mc). With the availability of data and resources, the system or application requirements were considered while choosing this objective function. The created neural network model has produced accurate and trustworthy results using this

objective function. A penalty value is imposed on the function's output if the link between the inputs and outputs is unmet. The penalty must be much higher than those generally obtained at the exit to ensure this condition is far from the function's minimum. The proper goal function is first provided, and then the evolutionary algorithm is executed. The sample size and the number of iterations for this method must be precisely specified since they substantially impact its overall performance.

There was shown to be a link between max η and ΔP. Similarly, the connection between ΔP min and the smallest value η was found. In this study, in addition to the optimal point determined by the minimum of $^{\Delta P}/_{\eta}$, we also consider the points with a minimum of $^{\Delta P}/_{\eta}$ and a maximum of η. We obtained the twist and bend values that match the minimum of $^{\Delta P}/_{\eta}$. As was previously documented, ΔP declines while η stays high in this location juxtaposes the findings of the present research with other published works. The dotted lines indicate the pressure differential, while the solid lines represent the mixing index. It is essential to mention that (Cortes-Quiroz, Azarbadegan, and Zangeneh 2014; Solehati, Bae, and Sasmito 2014) optimised their

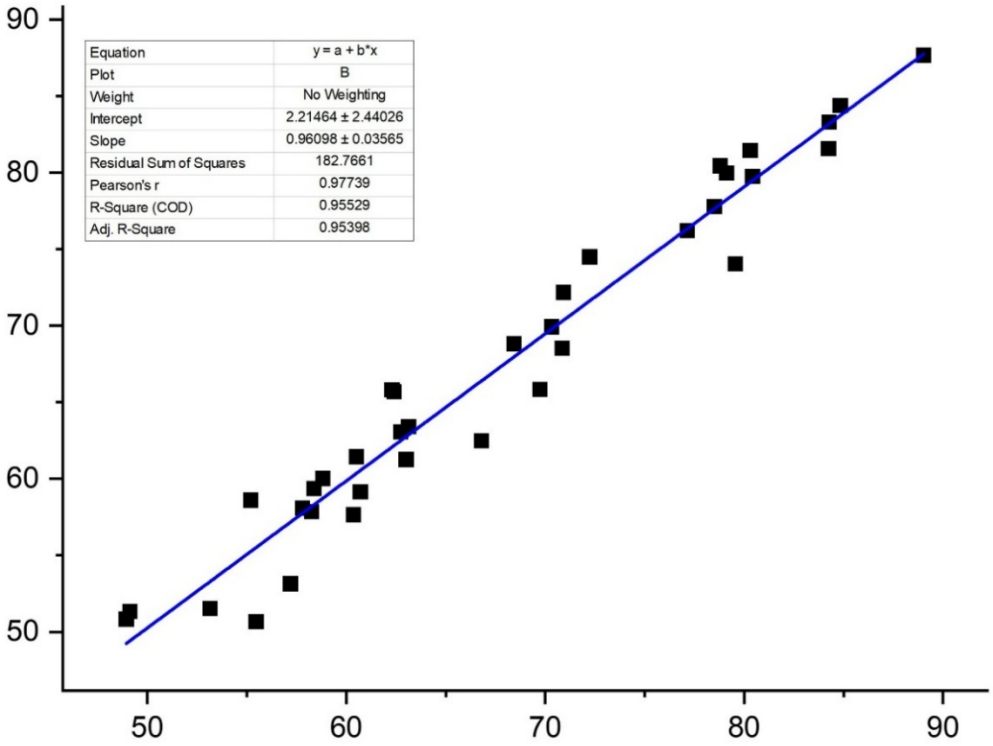

Figure 4.22 Linear fit plot for η.

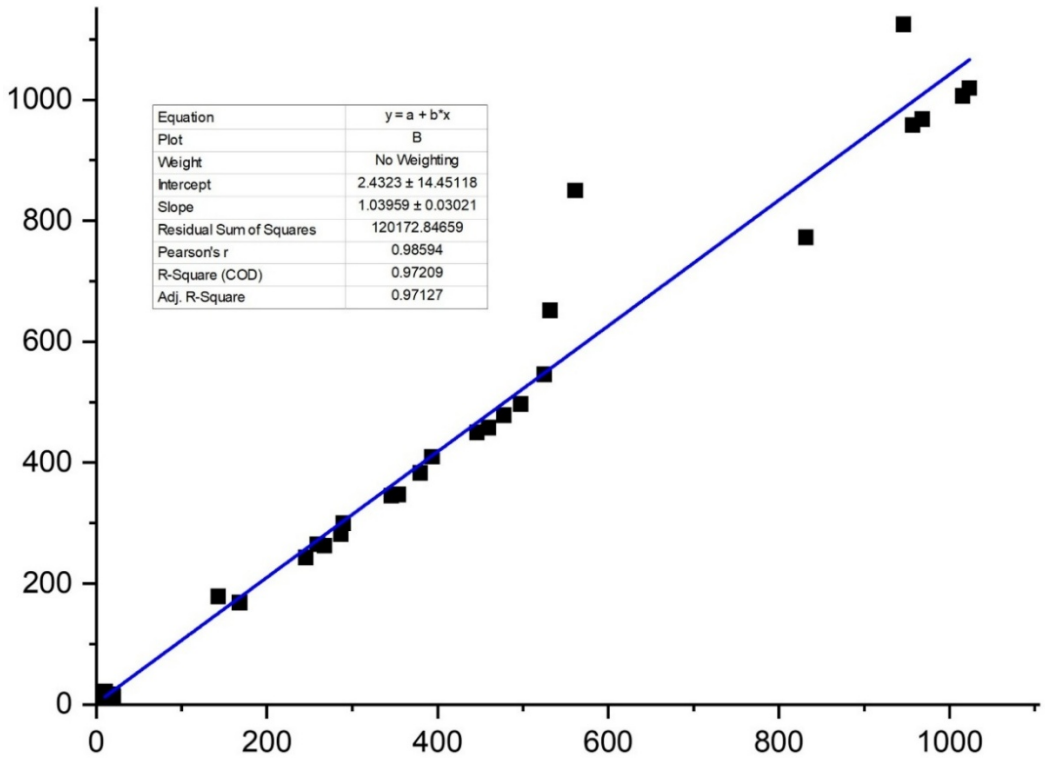

Figure 4.23 Linear fit plot for ΔP.

mixer only for a given Re. The graph illustrates that the present study exhibits a greater η at the Reynolds number than prior published works. The simulations performed better in fitting ΔP than η, suggesting that the mixing performance is more responsive to the formulation. Ultimately, the models achieved satisfactory metrics to determine the extent of the task. The table in Table 4.9 and 4.10 displays the most favourable values of η and their corresponding ΔP.

Table 4.9 The highest value of Optimization results

Obf	**Max**	**η (%)**	**ΔP**	**Twists**	**Bend**	**Re**
η(%)	87.76	87.76	-	4	60°	400
ΔP (Pa)	1094.55	-	1094.55	3	70°	450
$\mathbf{\Delta P/\eta}$	1280.02	85.51	1094.55	3	70°	450

Table 4.10 Lowest value of Optimization value

Obf	Min	η	ΔP	Twists	Bend	Re
η	50.64	50.64	-	2	70°	0.05
ΔP (Pa)	13.28	-	13.28 Pa	3	30°	0.05
$\Delta P/\eta$	26.22	52.86	13.28 Pa	3	30°	0.05

The optimization findings revealed that the optimised case's errors for the prediction of η, ΔP, and $\Delta P/\eta$ were 0.378 %, 1.4%, and 1.9%, respectively. These values are accurate to the actual value. The restrictions of the multi-variable optimization approach utilised may be to blame for the mistake in the maximum and lowest situations. Table 4.11 compares the best results from simulation and optimization for the variables, while Table 4.12 compares the optimized results between RSM and HHO.

Table 4.11 Comparison of Simulation and Optimised Results for OMTB.

	Twists	Bends	Re	η	ΔP (Pa)	ΔP/η
Simulation	4	50°	450	85.512%	998.06	1167.15
Optimal	4	60°	400	87.76%	974.20	1109.86

Table 4.12 Comparison of RSM and HHO Optimality for OMTB

	Twist	Bend	Re	η	ΔP (Pa)	ΔP/η
RSM	4	48°	450	79.31%	998.65	1259.17
HHO	4	60°	400	87.76%	974.20	1109.86

4.4 Numerical Analysis of Spiral Helical Micromixer Using C-Y Model

This study focuses on geometries with three levels of autonomy: base, spiral, and twist (Figure 4.24). Geometries are evaluated using two response variables: mixing percentage (η) and pressure differential (ΔP) measured at the micromixers' output. Generally, the hypotheses fit ΔP better than η, suggesting that the mixing percentage is more susceptible to the model. The models acquired enough metrics to define the

work's scope. Table 4.13 shows the optimal η values and their corresponding ΔP obtained from LHS. The primary channel's standard element size was the foundation for developing the numerical mesh.

The concentration contours in the micromixer's inlet area indicate a minute mixing layer between two fluids at the channel inlet. When it reaches the first spiral, the flow is somewhat disturbed, leading to an increase in thickness. The process becomes more intense when the mixture enters the "mixing unit," causing severe flow disruptions. The concentration layer thickens in the second spiral, indicating more species mixing. Adding spirals to the flow enhances the mixing rate by introducing advective effects to sluggish flows.

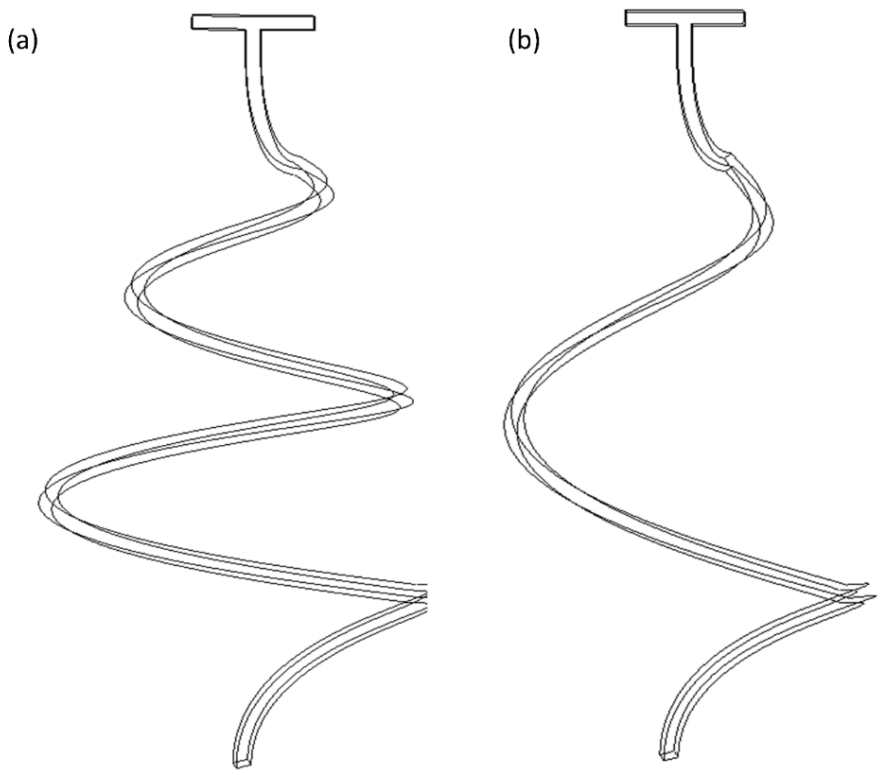

Figure 4.24 Proposed model design of helically spiral micromixer (HSM) with a) Spiral 2 b) Spiral 1.

Figure 4.25 exhibits the streamlines determined by the mass fraction of the species for the HSTM at the minimum blood flow rate examined in this study (≈0.00004 kg/hr).

The visualization shows that the HSTM achieves superior species diffusion because of its longer mixing length, which offers mass diffusion to occur within the stated time. The lengthened mixing length is the singular means of mass transportation, resulting in considerable mixing despite low mass loading.

For the η attained at the outlet, STM attains 34.5%, whereas HSTM achieves a substantially higher 98%. During low mass flow rates, the fluid streams move through the microchannel smoothly without signifying vortex formation. Nevertheless, as the $\dot{m}$ is raised, the fluid streams exit the mixer more rapidly, leading to a decrease in mixing, as demonstrated in Figure 4.27. While both micromixers exhibit a decline in their η with an upsurge in flow rate., HSTM outperforms STM (17.01%) with a higher percentage of 55.4% within a shorter axial distance.

Figure 4.26 illustrates how the η of STM and HSTM is affected by the blood mass flow rate across a wide range of flow rates. For the conventional STM, there is a constant reduction in the mixing efficiency, whereas, for HSTM, the mixing efficiency curve demonstrates a decreasing pattern. As previously mentioned, regarding STM, the high viscous nature of blood at high mass loading cannot sustain secondary flow or swirling motion due to the high viscous forces, resulting in the absence of an engulfment zone, even at higher $\dot{m}$. Because of the intense viscous forces, highly viscous blood cannot generate secondary flow or swirling motion even when carrying a high mass load. This results in the absence of an engulfment zone in STM. The lowest level of mixing achieved in STM is as low as 1.41% at the elevated mass flow rate ($\dot{m}$ = 0.095 kg/hr), whereas the highest mixing achieved (34.5%) at the nadir mass flow rate, owing to enough time is there for diffusion. In contrast, the HSTM outperforms the STM in terms of mixing efficiency at all mass flow rates, with complete mixing of streams (97%) at the nadir mass flow rate of $\dot{m}$ = 0.00004 kg/hr.

The η decreases considerably until the $\dot{m}$ reaches 0.00165 kg/hr. Beyond this point, stronger centrifugal forces drive the intertwining streams toward the helical spiral channel's wall, which increases secondary flow. As a result, the fluid experiences faster stretching, folding, and rotation, with improvement in η. As a result, the η increases significantly from 55.4% at a $\dot{m}$=0.00165 kg/hr to 78.6% at 0.095 kg/hr, demonstrating the benefits of HSTM for blending shear-thinning fluids at both

minima and maxima mass flow rate (mfr), like blood. Figure 4.27 depicts the η of the HSTM at different positions through the direction of the flow axially for different blood $\dot{m}$.

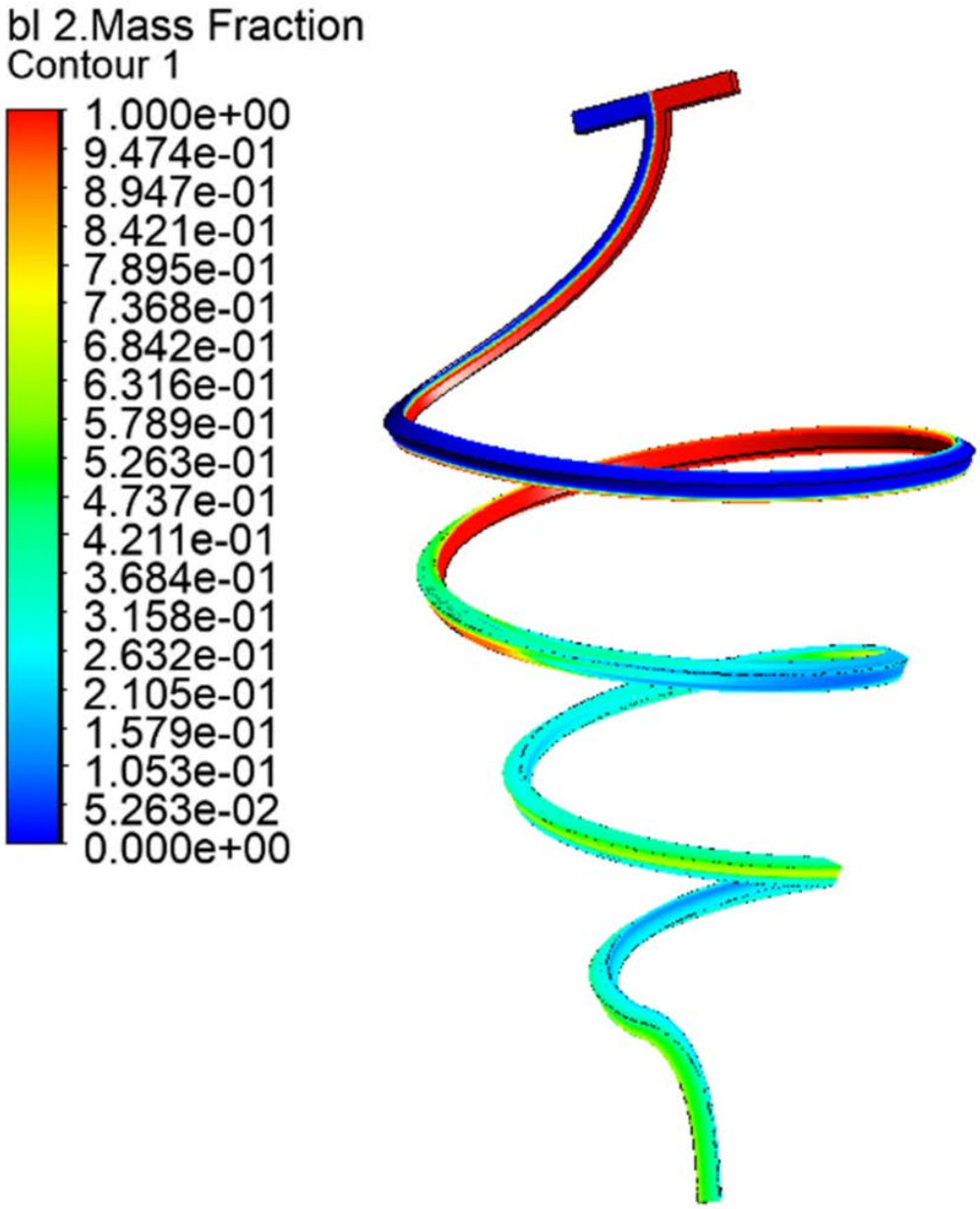

Figure 4.25 Mass fraction of Blood in HSTM

Figure 4.26 depicts a gradual decline in mixing efficiency in conventional STM as the flow of blood $\dot{m}$ rises. This is explained by the fact that very viscous blood cannot

support secondary flow or whirling motion under high mfr due to severe viscous forces.

Table 4.13 Population Design Variable obtained by LHS 1st Generation

Spiral	Re	η	ΔP	MeC
1.5	0.6	76.4004	14267.91	186.7518
1.5	0.6	76.4004	14267.91	186.7518
1	1	79.67148	11105.62	139.3926
1.5	0	60.65619	2631.646	43.38628
1.5	0.09	63.55696	2589.621	40.74488
1.5	0.03	61.64639	2555.353	41.45178
1.5	0.06	62.61323	2538.148	40.53693
2	0.06	71.53906	2430.77	33.97822
2	0.03	70.87201	1968.938	27.7816
1.5	0.03	61.64639	2555.353	41.45178
2	0.06	71.53906	2430.77	33.97822
1	0.03	58.26413	1679.461	28.82495
2	0.09	72.18432	2862.576	39.65648
2	0.09	72.18432	2862.576	39.65648
1.5	0.06	62.61323	2538.148	40.53693
1.5	0	60.65619	2631.646	43.38628
1.5	0.03	61.64639	2555.353	41.45178
1.5	0.03	61.64639	2555.353	41.45178
1	0.09	60.30039	2355.81	39.0679
1.5	0.09	63.55696	2589.621	40.74488
2	0.06	71.53906	2430.77	33.97822
1	0.03	58.26413	1679.461	28.82495

1.5	0.06	62.61323	2538.148	40.53693
1	0.03	58.26413	1679.461	28.82495
1.5	0.03	61.64639	2555.353	41.45178
1	0.06	59.29582	2017.383	34.02236
2	0.03	70.87201	1968.938	27.7816
1.5	0.06	62.61323	2538.148	40.53693
1	0.09	60.30039	2355.81	39.0679
1.5	0.06	62.61323	2538.148	40.53693

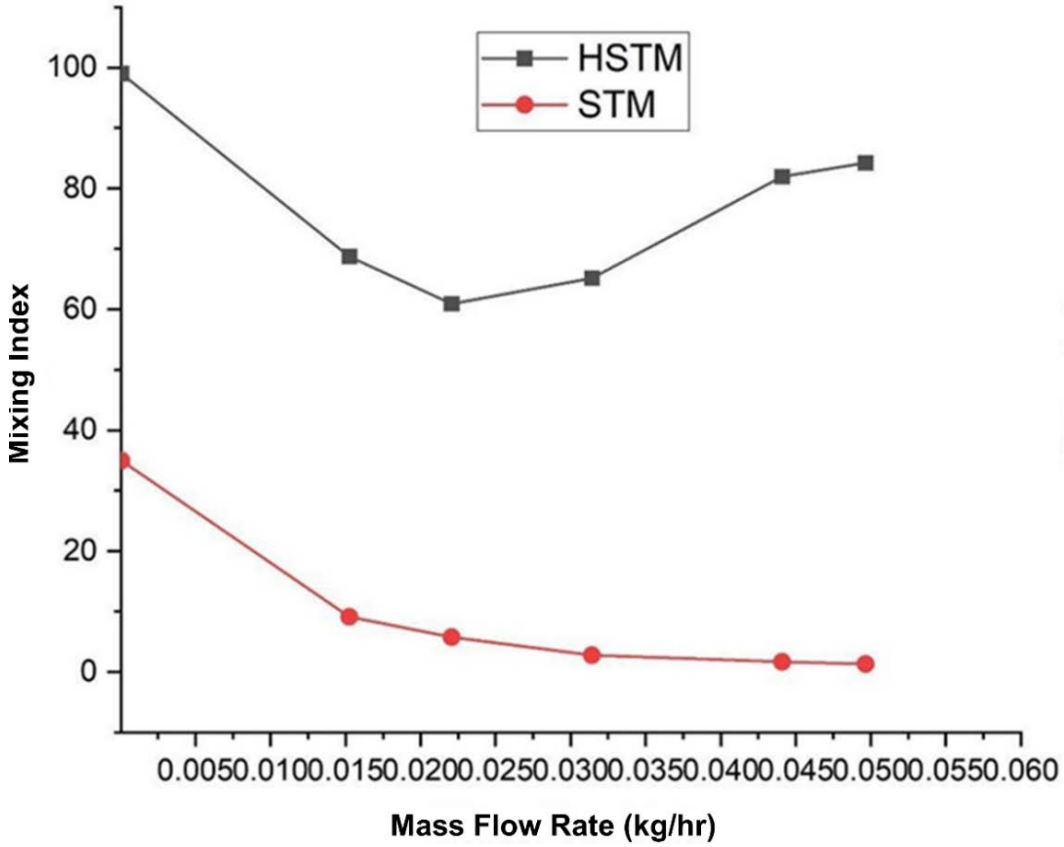

Figure 4.26 Comparison of STM and HSTM η for $\dot{m}$.

With a minimal η of 1.21% at the highest mass flow rate of 0.095 kg/hr, poor mixing quality is consequently seen at higher mass loading values. In contrast, HSTM demonstrates better η across all $\dot{m}$, achieving complete mixing even at the lowest $\dot{m}$ of 0.00004 kg/hrs. The η of HSTM shows a decline until a $\dot{m}$ of 0.00165 kg/hr, beyond which the centrifugal forces increase and cause rotation, stretching, and folding of the

particles in fluids. This leads to a noticeable improvement in the η. At a $\dot{m}$ of 0.00165 kg/hr, the η of HSTM decreases, but it starts to increase again as the centrifugal forces increase and cause folding, stretching and rotation of the fluid. This enhancement in the mixing efficiency results in a sharp rise in the mixing index from 55.4% to 78.6% as the $\dot{m}$ is increased to 0.095 kg/hrs.

The distribution of species mass fraction at various locations along the microchannel is shown in Figure 4.26 to visualize the extent of mixing in the system, with each plane located at a different distance from the T-junction. The η experiences the most significant increase from the beginning to the end of the micromixer for the smallest $\dot{m}$ (0.00004 kg/hr). A considerable rise in the η from 8.46% to 97% indicates complete mixing. The η curves obtained at different mass flow rates, namely, 0.0004 kg/hr, 0.00165 kg/hr, and 0.0065 kg/hr, show a linear trend to the axial distance of the micromixer. For axial distances less than 450 mm, the η remains relatively constant. A negligible change is noticed on planes after X = 500 mm. When the $\dot{m}$ is increased to 0.045 kg/hr and 0.095 kg/hr, the mixing curve's slope increases quickly until X = 450 mm. However, the η gradually increases on the subsequent planes, with a maximum value of 78.6% achieved at the outlet.

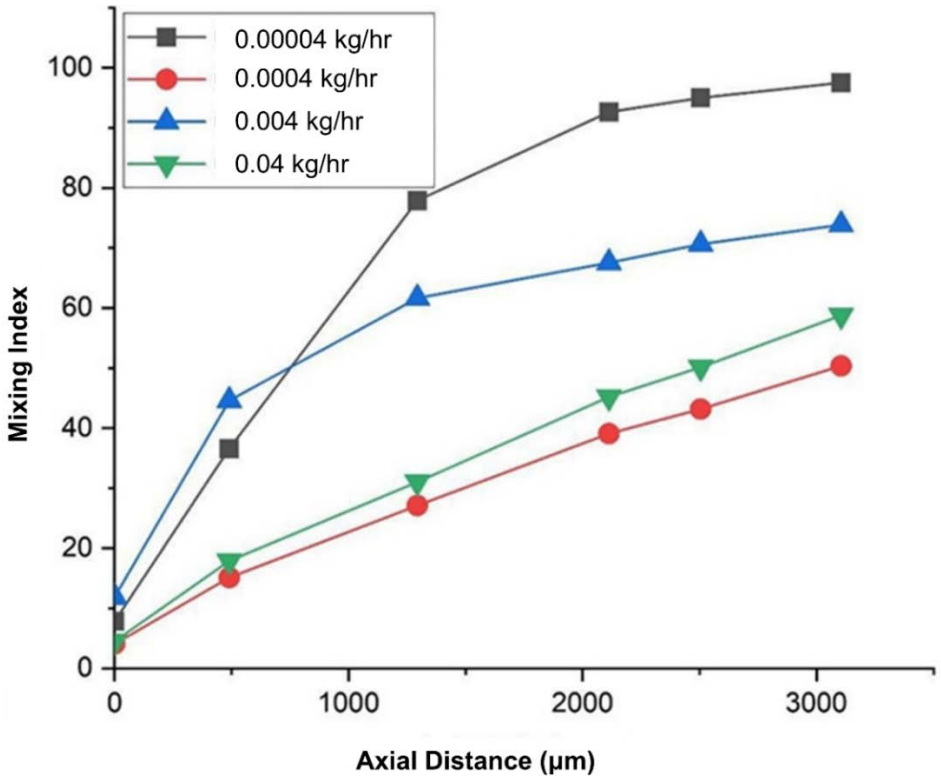

Figure 4.27 η at various axial lengths (μm).

Additionally, the interaction between the interfaces and the mixing mechanism is examined. At a $\dot{m}$ 0.00004 kg/hr, the fluid streams' interface appears linear at the helical microchannel's beginning. However, at 450 mm, the interface becomes diagonal, increasing the thickness of the diffusion zone and, therefore, a higher η. At low mfr, the fluid is thoroughly mixed at the micromixer outlet. However, the intersection becomes smaller in size as the $\dot{m}$ increases (0.0004 kg/hr and 0.0024 kg/hr). As a result, there is a noticeable drop in η and less mixed fluid at the exit portion. When the $\dot{m}$ is 0.038 kg/hr, the conformity of the fluid intersection is disrupted at the plane of the inlet. This leads to an increase in the intersectional area, which enhances the mass diffusion transport. The mixing performance improves due to the chaotic flow that enhances the mixing mechanism. The η rises after reaching 0.0014 kg/hr.

4.4.1 Effect of variation of geometric parameters of the micromixer on η and ΔP

The cases studied here represent geometries with two degrees of freedom: twists (T) and base diameter (B) with a constant axial length of 3000μm. The pressure differential (ΔP) and mixing percentage (η), measured at the micromixers' outlet section, are the response variables utilized to analyze the geometries.

A rapid rise in mass flow rates causes a corresponding rise in pressure drop. At the maximum mass loading, 92.32 KPa is the pressure decrease that can be measured (Figure 4.28). With $\dot{m}$ = 0.09 Kg/hr, it is clear that increasing the amount of energy needed to drive the flow is a constant trade-off for better mixing performance.

Simulated optimum points show minimal difference between η and ΔP, particularly for η. In contrast, ΔP exhibits more substantial changes, even with more exact measures.

4.4.1.1 *Mixing energy cost: A performance index*

The mixing energy cost (MeC) in micromixers is primarily influenced by fluid properties, micromixer design, and operating conditions. Passive micromixers are energy-efficient but may require high-pressure gradients. The Mixing Energy Cost

evaluates system performance based on η and ΔP response variables. Table 4.12 assesses the MeC of optimal configurations achieved with the i-GWO, highlighting the significance of high mixing percentage and minimal pressure drop.

CFD may be used to assess pressure difference in micromixers; however, experimental verification is still needed. Even with low microscale pressure, MeC is crucial for assessing micromixer designs.

Micromixers are used as reactors to create nanoparticles. As particles collect in slow-flowing areas, fluid passage becomes more challenging and energy-intensive. Designing with reduced resistance to flow (ΔP) can help alleviate this impact. This concept aligns with the Constructional theory perspective of enabling flow and maintaining system survival.

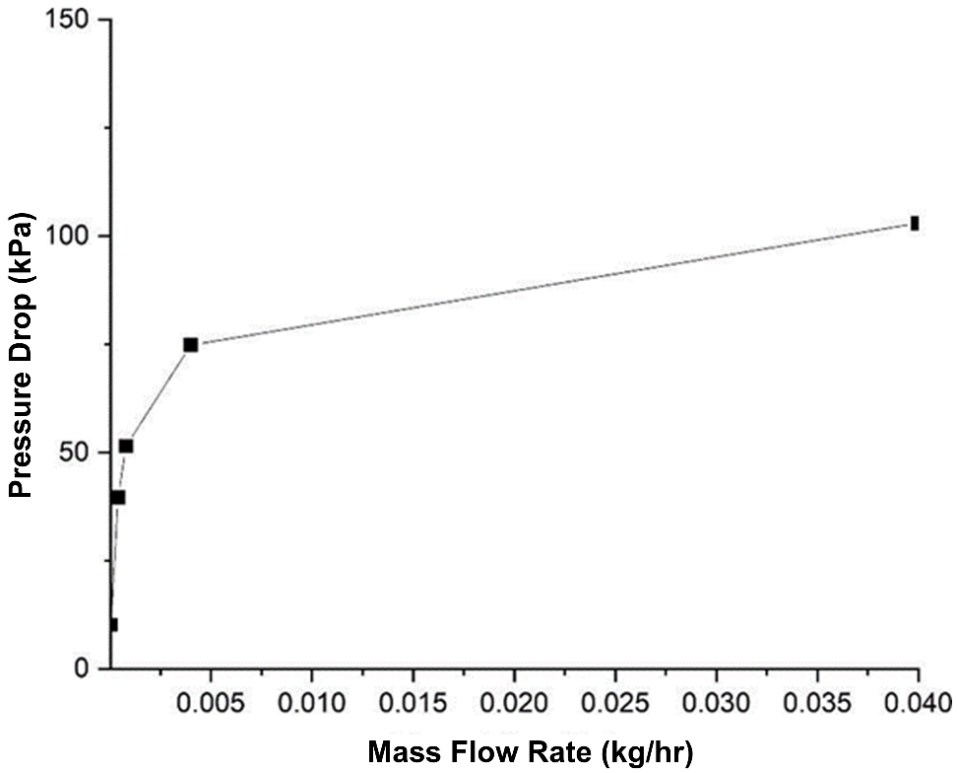

Figure 4.28 HSTM ΔP at various blood flow rates

4.4.1.2 *Optimization techniques*

This study included optimization approaches, including a design of the experiment, response surface method, sensitivity analysis, and a multi-objective i-GWO

algorithm using Python and ANSYS 2022 R1. Figure 3.4 presents an overview of the optimization approach employed in this study. To accomplish this, two alternative methodologies are used for the optimization process. The initial method emphasized enhancing MI, whereas the subsequent one aimed to optimize η and reduce ΔP. i-GWO is an evolutionary algorithm that produces a randomly initialized population. This population undergoes evolution via crossover and mutations. The crossover operator amalgamates attributes from both progenitors to generate a unique child, whereas the mutation operator instigates random modifications to an individual's traits to produce a new organism. The parent and offspring populations are combined, evaluated, and organized into Pareto fronts according to dominance criteria. Individuals are evaluated to ascertain dominance. Dominated persons hurt at least one aim without improving in any others. The sample is rated, and top recipients are picked as parents for the ones to come. More significant numbers are preferred as they are more distributed in the solution space. This approach evolves the population around the best possible outcomes. Table 4.12 summarizes the optimization outcomes for various Re numbers. To illustrate optimization impacts, we show MI and pressure changes compared to the basic scenario.

Table 4.14 Comparison of Simulation and Optimised Results for HSTM

	Spiral	**Re**	**η**	**ΔP (Pa)**	**ΔP/η**
Simulation	1	0.09	60.30039	2355.81	39.0679
Optimal	1.4	0.09	78.22	2438.2	31.17

4.5 Comparative Study of Newtonian and non-Newtonian Fluid

Newtonian and non-Newtonian fluids exhibit distinct flow behaviours due to differences in their viscosity response to shear stress. Their characteristics, governing equations, and real-world applications vary significantly. In microfluidic systems, particularly in micromixers, the behaviour of fluids significantly impacts mixing efficiency. Newtonian and non-Newtonian fluids exhibit different flow characteristics,

which influence the choice of micromixer design and operational parameters. Below is a comparison of these two fluid types in the context of micromixing Table 4.15:

i. Newtonian fluids rely primarily on diffusion and advection for mixing, often requiring high Reynolds numbers or active mixing techniques.
ii. Non-Newtonian fluids can exhibit unique flow behaviors (such as shear-thinning and elasticity) that enhance mixing in certain micromixer designs, even at low Reynolds numbers.

Table 4.15 Comparison between Newtonian and non-Newtonian

Aspect	**Newtonian**	**Non-Newtonian**
Definition	Fluids with constant viscosity independent of shear rate.	Fluids with viscosity that varies based on shear rate or stress.
Flow Behaviour	Follows linear shear-stress vs. shear-rate relationship.	Exhibits shear-thinning (pseudoplastic), shear-thickening (dilatant), or yield-stress behaviour.
Mixing mechanism	Diffusion-dominated at low Reynolds numbers (Re).	Complex flow patterns due to shear-dependent viscosity, aiding mixing in some cases.
Reynold number influence	Mixing efficiency increases with higher Re as inertial effects become significant.	Mixing efficiency is highly dependent on the viscosity model; some non-Newtonian fluids mix better at low Re due to elasticity effects.
Pressure drop	Relatively predictable and proportional to flow rate.	Higher or lower depending on fluid properties and micromixer design.

Performance in Passive Micromixers	Limited mixing at low Re due to laminar flow nature.	Exhibit improved mixing due to secondary flow effects in shear-thinning or viscoelastic fluids.
Application in Micromixers	Used in applications requiring predictable flow behavior, such as chemical and pharmaceutical mixing.	Essential in biomedical, food, and polymer processing industries where complex fluid properties must be considered.

4.6 Numerical Analysis of OTMB with Nanofluids

A numerical investigation of water's flow and mixing characteristics and a nanofluid including ferrous oxide nanoparticles within a T-shaped microchannel. The Reynolds number fluctuated between 10 and 400, whilst the nanoparticle volume concentration ranged from 2% to 5% (properties described in Table 4.16). Nanofluids with particle dimensions ranging from 20 to 100 nm were examined. The viscosity coefficient of the nanofluid, derived from experimental data, was consistently more significant than that of water. The viscosity was affected by nanoparticle concentration and particle size, with smaller particles leading to increased viscosity. The research delineated various flow regimes, encompassing steady irrotational flow, steady vortex flow characterized by two horseshoe vortices, and steady flow exhibiting two vortices within the mixing channel.

The FVM is utilized to solve the governing equations, incorporating predefined boundary conditions to achieve a precise mixing index for OTMB. A non-uniform structured grid is used for the analysis, as demonstrated in Figure 3.2.

The viscosity of the fluids in question is a crucial determinant of their flow and mixing behaviour. Experiments and modelling utilizing the molecular dynamics technique have shown that the viscosity of nanofluids is markedly more significant than that of the carrier fluid. This has been confirmed to have a satisfactory level of dependability. Furthermore, it relies not only on the concentration of nanoparticles but also on their

sizes and materials. Figure 4.29a shows the mass fraction and Figure 29b shows the velocity streamline of the OMTB.

The study results shown in Table 4.14 indicate that the nanofluid differs from the essential fluid in two significant aspects. Initially, it exhibits a greater density that increases proportionally with the volume concentration of nanoparticles, and at the peak concentration, it exceeds the density of water by thirty percent. Conversely, the viscosity of fluids increases nonlinearly with concentration and considerably exceeds the density of water. Thus, the presence of these two components will markedly modify the flow properties of fluids combined in the micromixer. The density of the nanofluid is independent of the nanoparticle size. However, the viscosity of the nanofluid is contingent upon the nanoparticle size. Consequently, it is prudent to examine the effects of nanoparticle volume concentration and size on flow and mixing regimes independently (Figure 4.32).

$$Re_{cr} = 135 + 0.25\emptyset + 1.25\emptyset^2 \quad (4.1)$$

Within this particular case, combining a conventional fluid (water) with nanofluid leads to the production of distinguishing properties that result from nanoparticle diffusion. At the beginning of the procedure, one of its inlets will inject water into the micromixer, which has a concentration of nanoparticles equal to zero. In addition, a nanofluid that has a particular volume concentration of particles, which is represented by the symbol $\emptyset$, is being injected by the other inlet. Under the condition that the T-shaped microchannel is entirely mixed, it will be possible to generate a nanofluid with a particular medium concentration. If the flow rates at the inlet are the same, the concentration of the created mixed nanofluid will be equivalent to the square root of $\emptyset$. Consequently, the mixing process might be shown by how the volume concentration of nanoparticles is altered (Figure 4.30).

Under these conditions, the mixing of the fluid and the nanofluid is minimal, and it can only be seen on the contact line that separates the two fluid bodies. Even if the diffusion coefficient decreases due to the rise in the viscosity coefficient, a minor improvement in mixing occurs as the concentration of nanoparticles increases.

Table 4.16 Nanofluids viscosity and density at various fraction and diameter

Volume Fraction (∅, %)	**0**	**2**	**5**
Viscosity (Pa.s)	10e-03	0.000923	0.00054
ρ (kg/m^3)	998	1159	1235

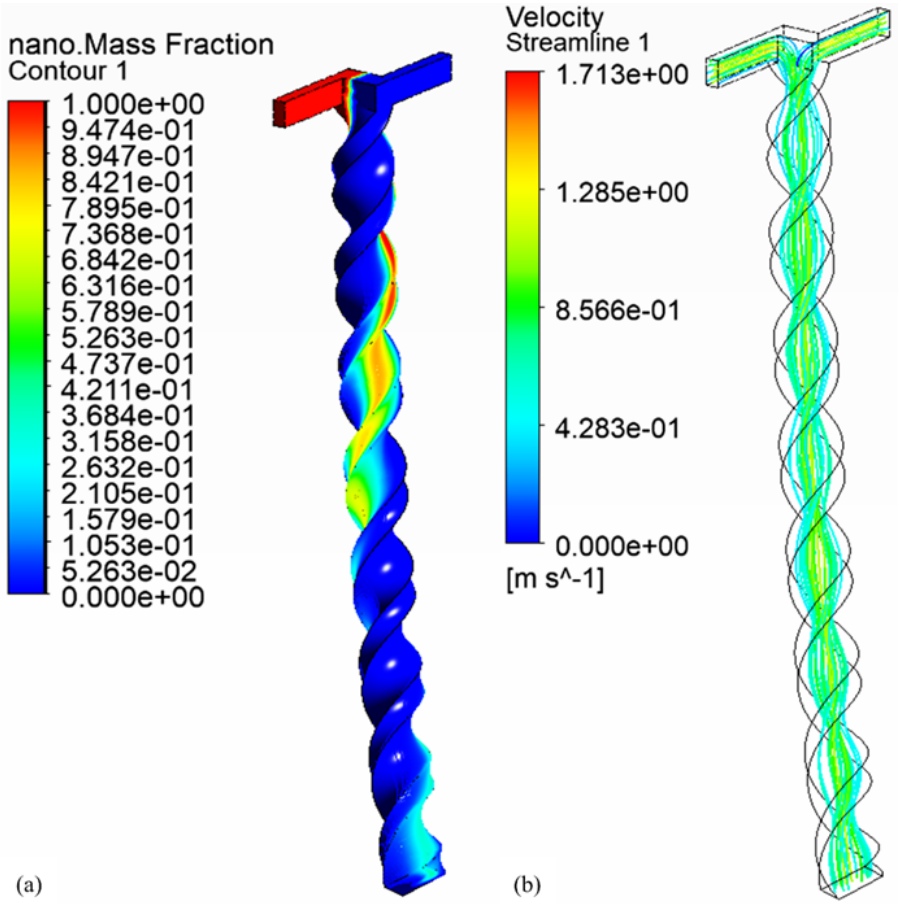

Figure 4.29 Mass Fraction of the OTMB with 4 Twists and Bend 50° (a) Mass Fraction (b) Velocity Streamline.

This forms a pair of symmetric horseshoe vortices within the mixer, which arises as the Reynolds number increases. These vortices, which begin close to the wall on the left side of the mixer, expand out into the mixing channel as they go through the mixer. When referring to these vortices, it is common practice to call them Dean vortices. They come into existence due to the creation of secondary flows, which are brought about by the action of the centripetal acceleration, which turns the flow. The simulation findings made it possible to determine the degree to which the critical

Reynolds number of the flow conditions depends on the concentration of nanoparticles. Figure 4.31 illustrates this dependence on the variable for the pressure drop. Nanofluids offer enhanced mixing properties in micromixers but introduce a higher pressure drop due to increased viscosity, particle-fluid interactions, and potential aggregation effects. In this context, the term "critical Reynolds number" refers to the value of the Reynolds number at which the flow undergoes a "turn-over," which means that instead of two vortices in the mixing channel, two single vortices start to exist. The critical

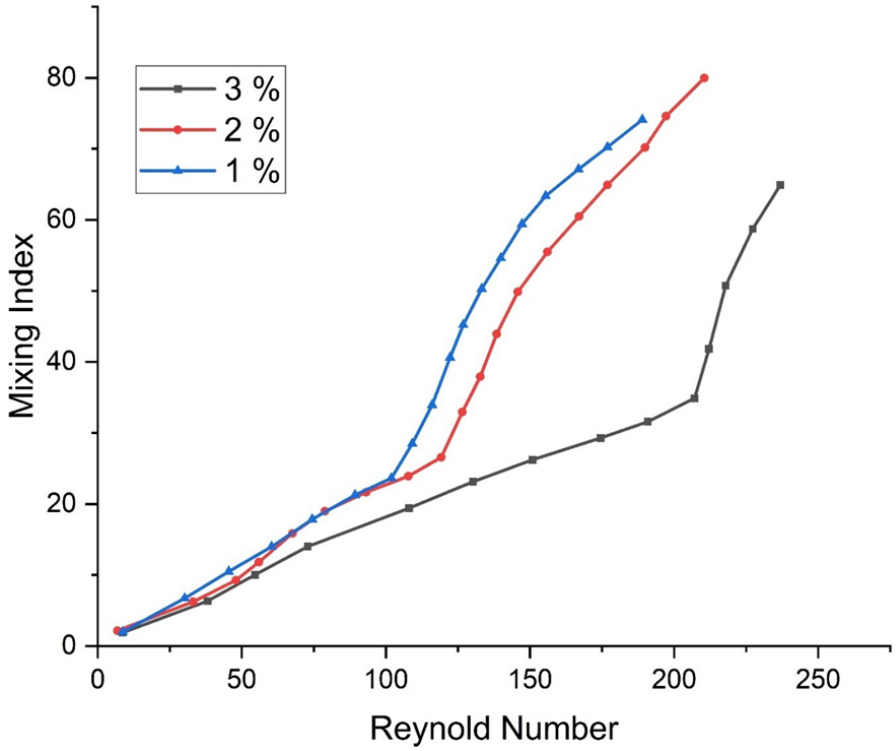

Figure 4.30 Mixing effect with Re at ø 1%, 2% and 3%.

Reynolds number will increase in a monotonic fashion as the concentration of nanoparticles increases. There is a correlation (Equation 4.1) of the type that can adequately represent the calculated dependency of the critical Reynolds number on the concentration of nanoparticles (Figure 4.32). Table 4.17 shows the design variable variation for different parameters for a 2 % volume fraction of ferrous oxide in the nanofluid effects on mixing index and pressure drops.

Table 4.17 Design variable 1st generation with the response for 2% Volume Fraction of Fe_3O_4

Twists	Bend	Velocity (m/s)	Mixing Index	Pressure Drop (Pa)
1	30°	2	67 %	198
1	30°	1	65.1 %	98
1	30°	0.5	64.5 %	49.5
2	30°	2	74.4 %	268
2	30°	1	72 %	201.5
2	30°	0.5	70.5 %	61
4	50°	2	79 %	269
4	50°	1	77.7 %	123
4	50°	0.5	77.5 %	61.25

Under the findings of an investigation into the impact that the concentration of nanoparticles has on the flow, the "turn-over" regime of the flow undergoes a transition toward more significant Reynolds values as the volume concentration of nanoparticles increases. As an illustration, it has been established that the shift occurs at a Reynolds number of around 150 when the concentration of nanoparticles is 2%. On the other hand, the shift takes place at a Reynolds number of around 180 when the concentration is 5%. These phenomena may be explained by the fact that there is an increase in the viscosity of the nanofluid that takes place whenever there is an increase in the volume concentration of nanoparticles in the nanofluid. The findings of this investigation indicated that as the viscosity of one of the fluids is raised, the "turn-over" of the flow tends toward more significant Re values.

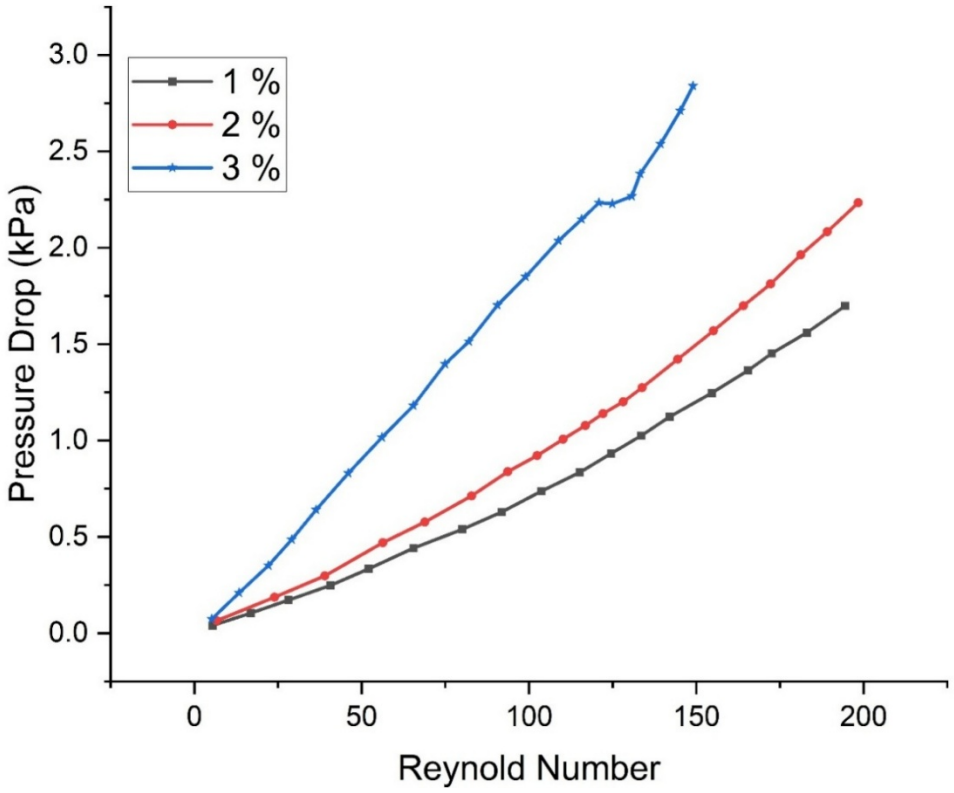

Figure 4.31 Pressure drop (kPa) dependency with Re at volume fractions 1%, 2% and 3%.

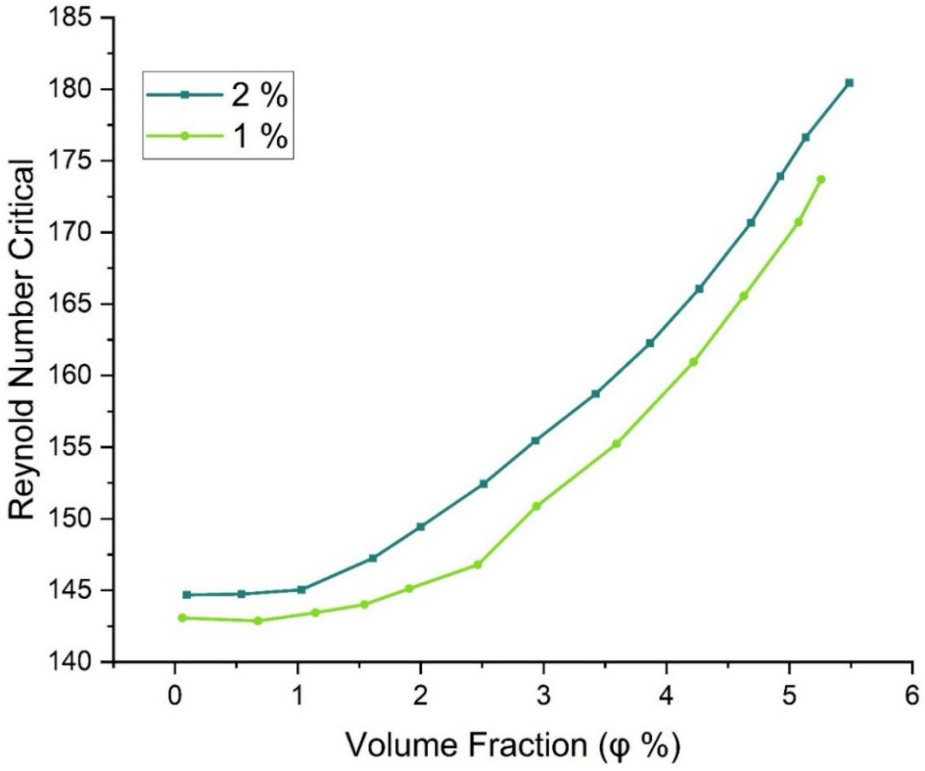

Figure 4.32 Critical Re at volume fraction of nanoparticles

Chapter 5 CONCLUSIONS, FUTURE SCOPE AND SOCIAL IMPACT

5.1 Conclusions

5.1.1 Numerical Analysis and Optimization of TBM Model

We have examined the performance of a T-junction micromixer with a twisted and bent mixing channel using computational analysis and a metaheuristic algorithm. According to our research, the radial secondary flow rises as the mixing channel's number of turns and bend angle increases, enhancing mixing efficiency. Based on the findings of the study, the following conclusions are made:

i. Additionally, we have shown that the twisted mixing channel performs best for Reynolds values between 10 and 550 since it significantly raises the mixing index while having a negligible influence on the pressure drop.

ii. A combination of simulations was run to assess the effect of twist and bend parameters on a micromixer channel. The collected data was capitalized to test and train a neural network, resulting in more than 99% accuracy for η and 97% for ΔP predictions. The nonlinearity of the TBM model may be captured using neural networks.

iii. A global optimization approach with the parameters of twist and bend was performed to get the optimal model. The MFO algorithm resulted in ‘twists of 4 and a bend of 70° at a Reynolds number 10.

iv. Upon verification of the optimized TBM model through simulation, the resulting values of η (79.76%) and ΔP (17.925 Pa) showed minor errors of 0.56% and 2.78%, respectively. This indicates that the optimization process led to a micromixer design with accurate values of both η and ΔP.

Our process is significantly faster than that of CFD simulation-based optimization.

5.1.2 Optimizing Offset Passive Micromixer

In this study utilised the principles of constructal theory to undertake an evolutionary design of passive micromixers. The constructal design method, in conjunction with the RSM, HHO and CFD, serves as a framework for improving the performance of a given configuration by gradually introducing additional degrees of freedom and progressing towards more optimal designs. In this investigation, the best values of parameters impacting the performance of the micromixer were explored with CFD simulations and metaheuristic algorithms to obtain the maximum η and minimal ΔP. A neural network was trained and tested using the gathered data, and the results showed more than 99% accuracy for predictions η and 98.5% for ΔP predictions. A global optimization strategy based on the twist and bend parameter was used to obtain the ideal model.

The optimised OMTB model's simulation-based verification revealed slight inaccuracies of 0.378% and 1.4% in the calculated values of max η (87.76%) and min ΔP (13.28 Pa). It shows a micromixer with precise η and ΔP values from this optimization procedure.

The findings of this investigation led to the following conclusions.

i. The CFD simulations indicate that mixing is enhanced at low and very high Reynolds numbers (Re). However, pressure drops increase at high Re, countering the optimization goal. This occurs due to elevated transverse velocities within the channel bends and twists, which enhance mixing. A higher transverse velocity factor intensifies chaotic convection, increasing mixing efficiency (η) while aiming to minimize pressure drop (ΔP).
ii. The response surfaces also demonstrated that, after crossing the threshold point, the mixing improved with increasing Re in all values of bend and twists. With an overall desirability of 0.898 for a micromixer with bends and twists

with η = 79.31% and ΔP = 988.65 Pa, at input variable of $\mathrm{Re} = 450$, $\mathrm{bend} = 48°$, and $\mathrm{twists} = 4$ was obtained.

iii. HHO outperformed RSM, optimizing for optimal parameters. The preferred design, with parameters, are $\mathrm{Re} = 400$, $\mathrm{bend} = 60°$, and $\mathrm{twist} = 4$, was determined for optimality, having η= 87.76% and ΔP = 974.20 Pa.

iv. A better ratio of the $\Delta P/\eta$ achieved using RSM rather than through optimization with HHO. HHO and RSM came up with results of 1109.86 and 1259.17, respectively. The best input factor values from the RSM and HHO approaches were used in the CFD simulation.

5.1.3 Numerical Analysis of HSTM with C-Y Model

The study found that the HSTM performs better than the STM in η for non-Newtonian fluid blood across all examined mass flow rates. To investigate the relationship between mixing performance and $\dot{m}$, the study presents several types of analysis, such as streamlines and graphs for fluids at different planes. The results indicate that the HSTM design demonstrates superior η over the STM design across a broad range of mass flow rates. Specifically, at the lowest mass flow rate of $\dot{m}$ = 0.00004 Kg/hrs, the HSTM shows a significant improvement in η of 62.5% compared to the STM. Even at the highest mass flow rate of $\dot{m}$=0.095 Kg/hrs, the HSTM outperforms the STM, achieving a remarkable η of 78.6% versus a mere 1.21% for the STM. These findings suggest the proposed HSTM design has great potential for practical use in various applications.

5.1.4 Numerical Analysis of OTMB with Nanofluids

The simulation data demonstrated that the flow conditions observed in mixing a typical fluid and a nanofluid are qualitatively identical to those observed in mixing two normal fluids. These flow conditions include steady irrotational flow, steady vortex flow with two horseshoe vortices, a stepwise change in the flow structure (turn-over), and steady flow with two vortices in the mixing channel. When the flow

transitions from a regime with two vortices to a flow regime with two single vortices, it has been demonstrated that the mixing efficiency increases several times. However, the shift from one regime to another is not as simple to forecast as one might think. This is because the viscosity of nanofluids significantly increases, and the density is also significantly higher. Further, the viscosity of a substance is determined by the particle size, and it rises as the particle size decreases. According to equation 4.61, the diffusion coefficient is inversely proportional to the particle diameter and the viscosity coefficient, which depends on the particle size. On the other hand, the particle size has a complex relationship with the diffusion coefficient since it depends on the particle size. The critical value of the Reynolds number of the transition of flow regimes has been determined to be dependent on the concentration of nanoparticles as a result of the analysis of the calculation data. This was discovered as a result of the findings of the discussion. Increasing the concentration of nanoparticles has been demonstrated to increase the critical value of the Reynolds number. The crucial value of the Reynolds number is dependent on the size of the nanoparticles once this dependence has been established. It has also been demonstrated that the crucial value of the Reynolds number decreases as the average size of nanoparticles grows. This is something that has been proven from previous research. Therefore, it is possible to modify the flow and mixing regimes in the micromixer by adjusting the nanoparticle concentration and the particles' size.

i. Under the suggested micromixers, the hydrodynamic behaviour of Newtonian flow was enhanced by the effects of generalized Reynolds numbers.
ii. If there is a high concentration of nanofluids, the micromixer will produce robust secondary flows to enhance the mixing quality throughout the process.
iii. The micromixer is designed to produce strong secondary flows, improving the mixing quality regardless of the nanofluid concentration.
iv. The higher amount of disorder in the system suggested by increased entropy generation can be advantageous in specific applications where efficiency is crucial.

5.2 Future Scope

i. Exploring Alternative Passive Designs

Passive micromixer**s** leverage channel geometry and fluid dynamics to enhance mixing without external energy sources. Future studies could investigate various channel shapes, bifurcations, and curvatures to optimize mixing efficiency while maintaining low energy consumption.

ii. Introducing Pillars or Obstacles

Incorporating obstacles such as pillars, ridges, or baffles into micromixer designs can improve fluid mixing. These structures induce secondary flows (e.g., vortices, chaotic advection), enhancing fluid diffusion and overall performance in microfluidic systems.

iii. Multi-Objective Optimization Algorithms

Future research could utilize MOEA to refine micromixer designs by balancing key parameters:

Cost – Considering material and fabrication expenses.

iv. Expanding to Non-Newtonian and Complex Fluids

Most studies focus on Newtonian fluids, but many applications involve non-Newtonian fluids (e.g. polymers and suspensions) with complex behaviours like shear-thinning or viscoelastic effects. Investigating these fluids could expand micromixer applications in biomedical, pharmaceutical, and chemical industries.

5.3 Application and Social Impact of Micromixers

Microfluidic micromixers have a wide range of applications, particularly in fields requiring precise and efficient mixing of fluids at a microscale. Here are some key applications:

i. Chemical Synthesis: Micromixers enable precise control over reaction parameters, such as temperature and concentration, at the microscale. This results in higher yields, reduced waste, and quicker reaction times. They are used in synthesizing nanoparticles, polymers, and other fine chemicals with consistent quality.

ii. Clinical Diagnostics: In diagnostic devices, micromixers are crucial for mixing patient samples with reagents. This ensures uniform reactions, leading to accurate detection of biomarkers, pathogens, or disease indicators. For instance, micromixers are integrated into point-of-care testing devices for rapid and reliable results.

iii. DNA Analysis: Micromixers are used in processes like DNA extraction, amplification (e.g., PCR), and sequencing. Efficient mixing helps in preparing DNA samples by blending them with enzymes, primers, or dyes, which is essential for high-quality data in genetic research or forensic analysis.

iv. Pharmaceutical Applications: In drug development and testing, micromixers play a role in formulating and testing drug candidates. They allow precise control over reagent mixing, aiding in enzyme assays, protein folding studies, and the production of liposomes or drug delivery systems.

v. Biochemical Assays: Micromixers facilitate complex biochemical processes, such as enzyme kinetics studies or immunoassays. They enable rapid and

efficient dilution, reaction, or detection steps, saving time and resources in laboratory workflows.

5.3.1 Micromixers Application in the Industry

5.3.1.1 *Micromixers as Microreactors*

i. Micromixers are crucial in the chemical industry due to their rapid mixing process.
ii. They facilitate the synthesis of novel, unattainable products in significant reactors.
iii. The efficiency of the micromixer directly impacts the overall reaction rate.

5.3.1.2 *Homogeneous Reactions*

i. Micromixers can serve as microreactors for homogeneous liquid-phase reactions.
ii. They are effective platforms for synthesizing solid microparticles, offering control over particle size and shape.
iii. They are well-suited for combinatorial chemistry, particularly in synthesising proteins for drug discovery.

5.3.1.3 *Heterogeneous Reactions*

i. Micromixers allow for the incorporation of solid catalysts in the form of beads or porous materials within the mixing channel.
ii. They can generate microdroplets that create a large interfacial area, enabling high-efficiency synthesis reactions between organic and aqueous phases.

5.3.1.4 *Chemical Sensitivity Enhancement*

i. Micromixers can control chemical selectivity, the relative preference for forming specific products.
ii. The influence of selectivity is shaped by competing reactions that can take place in parallel or sequentially.
iii. Micromixers effectively regulate selectivity in kinetics-driven reactions, but they do not affect selectivity controlled by thermodynamic stability.

5.3.1.5 *Biochemical Sensors and Preconcentration and Purification*

i. Micromixers with chaotic advection enhance analyte transport to surface-immobilized receptors.
ii. This method enables efficient and controlled binding between antibodies and immobilized protein.
iii. The level of chaotic advection plays a critical role in determining detection quality.

5.3.1.6 *Preconcentration and Purification*

i. DNA sample preconcentration and purification are crucial for accurate and reliable pathogen detection.
ii. Micromixers allow for precise control over buffer concentrations and facilitate the generation of chaotic advection.
iii. Examples include serpentine micromixers for DNA purification and di-electrophoresis (DEP).

References

Afzal, A., Kim, K.-Y., 2015. Convergent–divergent micromixer coupled with pulsatile flow. Sens. Actuators B Chem. 211, 198–205. https://doi.org/10.1016/j.snb.2015.01.062

Afzal, A., Kim, K.-Y., 2014. Three-objective optimization of a staggered herringbone micromixer. Sens. Actuators B Chem. 192, 350–360. https://doi.org/10.1016/j.snb.2013.10.109

Afzal, A., Kim, K.-Y., 2012. Passive split and recombination micromixer with convergent–divergent walls. Chem. Eng. J. 203, 182–192. https://doi.org/10.1016/j.cej.2012.06.111

Ahmadian Yazdi, A., Sadeghi, A., Saidi, M.H., 2015. Electrokinetic mixing at high zeta potentials: Ionic size effects on cross stream diffusion. J. Colloid Interface Sci. 442, 8–14. https://doi.org/10.1016/j.jcis.2014.11.059

Ahmed, D., Mao, X., Shi, J., Juluri, B.K., Huang, T.J., 2009. A millisecond micromixer via single-bubble-based acoustic streaming. Lab. Chip 9, 2738. https://doi.org/10.1039/b903687c

Alam, A., Afzal, A., Kim, K.-Y., 2014. Mixing performance of a planar micromixer with circular obstructions in a curved microchannel. Chem. Eng. Res. Des. 92, 423–434. https://doi.org/10.1016/j.cherd.2013.09.008

Al-Halhouli, A., Alshare, A., Mohsen, M., Matar, M., Dietzel, A., Büttgenbach, S., 2015. Passive Micromixers with Interlocking Semi-Circle and Omega-Shaped Modules: Experiments and Simulations. Micromachines 6, 953–968. https://doi.org/10.3390/mi6070953

Ang, K.M., Yeo, L.Y., Hung, Y.M., Tan, M.K., 2016. Amplitude modulation schemes for enhancing acoustically-driven microcentrifugation and micromixing. Biomicrofluidics 10, 054106. https://doi.org/10.1063/1.4963103

Ansari, M., Kim, K.-Y., Kim, S., 2018. Numerical and Experimental Study on Mixing Performances of Simple and Vortex Micro T-Mixers. Micromachines 9, 204. https://doi.org/10.3390/mi9050204

Arshad Afzal, Kwang-Yong Kim, 2014. Performance Evaluation of Three Types of Passive Micromixer with Convergent-Divergent Sinusoidal Walls. J. Mar. Sci. Technol. 22. https://doi.org/10.6119/JMST-014-0321-2

Bahei Islami, S., Ahmadi, S., 2019. The effect of flow parameters on mixing degree of a three dimensional rhombus micromixer with obstacles in the middle of the mixing channel using oscillatory inlet velocities. Transp Phenom Nano Micro Scales 7. https://doi.org/10.22111/tpnms.2019.14668.1092

Balasubramaniam, L., Arayanarakool, R., Marshall, S.D., Li, B., Lee, P.S., Chen, P.C.Y., 2017. Impact of cross-sectional geometry on mixing performance of spiral microfluidic channels characterized by swirling strength of Dean-vortices. J. Micromechanics Microengineering 27, 095016. https://doi.org/10.1088/1361-6439/aa7fc8

Ballard, M., Owen, D., Mills, Z.G., Hesketh, P.J., Alexeev, A., 2016. Orbiting magnetic microbeads enable rapid microfluidic mixing. Microfluid. Nanofluidics 20, 88. https://doi.org/10.1007/s10404-016-1750-1

Bayareh, M., Usefian, A., Ahmadi Nadooshan, A., 2018. Rapid mixing of Newtonian and non-Newtonian fluids in a three-dimensional micro-mixer using non-uniform magnetic field. J. Heat Mass Transf. Res. https://doi.org/10.22075/jhmtr.2018.15611.1218

Bazaz, S.R., Mehrizi, A.A., Ghorbani, S., Vasilescu, S., Asadnia, M., Warkiani, M.E., 2018. A hybrid micromixer with planar mixing units. RSC Adv. 8, 33103–33120. https://doi.org/10.1039/C8RA05763J

Bazaz, S.R., Mehrizi, A.A., Javid, S.M., n.d. Increasing the efficiency of microfluidic micromixer with gaps and baffles using design of experiments based on Taguchi method 8.

Bessoth, F.G., deMello, A.J., Manz, A., 1999. Microstructure for efficient continuous flow mixing. Anal. Commun. 36, 213–215. https://doi.org/10.1039/a902237f

Bhagat, A.A.S., Peterson, E.T.K., Papautsky, I., 2007. A passive planar micromixer with obstructions for mixing at low Reynolds numbers. J. Micromechanics Microengineering 17, 1017–1024. https://doi.org/10.1088/0960-1317/17/5/023

Bhattacharyya, S., Bera, S., 2015. Combined electroosmosis-pressure driven flow and mixing in a microchannel with surface heterogeneity. Appl. Math. Model. 39, 4337–4350. https://doi.org/10.1016/j.apm.2014.12.050

Boroun, S., 2016. Enhancing Liquid Micromixing Using Low‐Frequency Rotating Nanoparticles. AIChE J. 00, 10.

Branebjerg, J., Gravesen, P., Krog, J.P., Nielsen, C.R., 1996. Fast mixing by lamination, in: Proceedings of Ninth International Workshop on Micro Electromechanical Systems. Presented at the Ninth International Workshop on Micro Electromechanical Systems, IEEE, San Diego, CA, USA, pp. 441–446. https://doi.org/10.1109/MEMSYS.1996.494022

Buchegger, W., Wagner, C., Lendl, B., Kraft, M., Vellekoop, M.J., 2011. A highly uniform lamination micromixer with wedge shaped inlet channels for time resolved infrared spectroscopy. Microfluid. Nanofluidics 10, 889–897. https://doi.org/10.1007/s10404-010-0722-0

Charmet, J., Arosio, P., Knowles, T.P.J., 2018. Microfluidics for Protein Biophysics. J. Mol. Biol. 430, 565–580. https://doi.org/10.1016/j.jmb.2017.12.015

Chen, C.-Y., Lin, C.-Y., Hu, Y.-T., 2014. Inducing 3D vortical flow patterns with 2D asymmetric actuation of artificial cilia for high-performance active micromixing. Exp. Fluids 55, 1765. https://doi.org/10.1007/s00348-014-1765-x

Chen, X., Li, T., 2017. A novel passive micromixer designed by applying an optimization algorithm to the zigzag microchannel. Chem. Eng. J. 313, 1406–1414. https://doi.org/10.1016/j.cej.2016.11.052

Chen, X., Li, T., 2016. A novel design for passive misscromixers based on topology optimization method. Biomed. Microdevices 18, 57. https://doi.org/10.1007/s10544-016-0082-y

Chen, X., Zhang, L., 2017. A review on micromixers actuated with magnetic nanomaterials. Microchim. Acta 184, 3639–3649. https://doi.org/10.1007/s00604-017-2462-2

Chen, X., Zhang, S., Wu, Z., Zheng, Y., 2019. A novel Koch fractal micromixer with rounding corners structure. Microsyst. Technol. 25, 2751–2758. https://doi.org/10.1007/s00542-019-04296-4

Cheng, K.C., Lin, R.-C., Ou, J.-W., 1976. Fully Developed Laminar Flow in Curved Rectangular Channels. J. Fluids Eng. 98, 41–48. https://doi.org/10.1115/1.3448205

Choi, E., Kim, B., Park, J., 2009. High-throughput microparticle separation using gradient traveling wave dielectrophoresis. J. Micromechanics Microengineering 19, 125014. https://doi.org/10.1088/0960-1317/19/12/125014

Chung, C.K., Shih, T.R., 2007. A rhombic micromixer with asymmetrical flow for enhancing mixing. J. Micromechanics Microengineering 17, 2495–2504. https://doi.org/10.1088/0960-1317/17/12/016

Daghighi, Y., Li, D., 2013. Numerical study of a novel induced-charge electrokinetic micro-mixer. Anal. Chim. Acta 763, 28–37. https://doi.org/10.1016/j.aca.2012.12.010

Daghighi, Y., Sinn, I., Kopelman, R., Li, D., 2013. Experimental validation of induced-charge electrokinetic motion of electrically conducting particles. Electrochimica Acta 87, 270–276. https://doi.org/10.1016/j.electacta.2012.09.021

Deshmukh, A.A., Liepmann, D., Pisano, A.P., 2000. Continuous Micromixer with Pulsatile Micropumps, in: 2000 Solid-State, Actuators, and Microsystems Workshop Technical Digest. Presented at the 2000 Solid-State, Actuators, and Microsystems Workshop, Transducer Research Foundation, Inc., Hilton Head, South Carolina, USA, pp. 73–76. https://doi.org/10.31438/trf.hh2000.18

Deval, J., Tabeling, P., Chih-Ming Ho, 2002. A dielectrophoretic chaotic mixer, in: Technical Digest. MEMS 2002 IEEE International Conference. Fifteenth IEEE International Conference on Micro Electro Mechanical Systems (Cat. No.02CH37266). Presented at the Technical Digest. MEMS 2002 IEEE International Conference. Fifteenth IEEE

International Conference on Micro Electro Mechanical Systems, IEEE, Las Vegas, NV, USA, pp. 36–39. https://doi.org/10.1109/MEMSYS.2002.984074

Dietzel, A., 2016. A Brief Introduction to Microfluidics, in: Dietzel, Andreas (Ed.), Microsystems for Pharmatechnology. Springer International Publishing, Cham, pp. 1–21. https://doi.org/10.1007/978-3-319-26920-7_1

Du, M., Ma, Z., Ye, X., Zhou, Z., 2013. On-chip fast mixing by a rotary peristaltic micropump with a single structural layer. Sci. China Technol. Sci. 56, 1047–1054. https://doi.org/10.1007/s11431-013-5140-6

Du, Y., Zhang, Z., Yim, C., Lin, M., Cao, X., 2010. A simplified design of the staggered herringbone micromixer for practical applications. Biomicrofluidics 4, 024105. https://doi.org/10.1063/1.3427240

Ebrahimi, S., Hasanzadeh-Barforoushi, A., Nejat, A., Kowsary, F., 2014. Numerical study of mixing and heat transfer in mixed electroosmotic/pressure driven flow through T-shaped microchannels. Int. J. Heat Mass Transf. 75, 565–580. https://doi.org/10.1016/j.ijheatmasstransfer.2014.04.004

El Moctar, A.O., Aubry, N., Batton, J., 2003. Electro-hydrodynamic micro-fluidic mixerElectronic supplementary information (ESI) available: Video of effect of electric field on channel flow mixing. See http://www.rsc.org/suppdata/lc/b3/b306868b/. Lab. Chip 3, 273. https://doi.org/10.1039/b306868b

Ergin, F.G., Watz, B.B., Ērglis, K., Cēbers, A., 2015. Time-resolved velocity measurements in a magnetic micromixer. Exp. Therm. Fluid Sci. 67, 6–13. https://doi.org/10.1016/j.expthermflusci.2015.02.019

Evans, J.D., Palhares Junior, I.L., Oishi, C.M., 2017. Stresses of PTT, Giesekus, and Oldroyd-B fluids in a Newtonian velocity field near the stick-slip singularity. Phys. Fluids 29, 121604. https://doi.org/10.1063/1.4993782

Fox, R.W., Mitchell, J.W., 2019. Fox and McDonald's introduction to fluid mechanics, 10th edition. ed. Wiley, Hoboken.

Fu, L.M., Tsai, C.H., Leong, K.P., Wen, C.Y., 2010. Rapid micromixer via ferrofluids. Phys. Procedia 9, 270–273. https://doi.org/10.1016/j.phpro.2010.11.060

Fu, Y.Q., Luo, J.K., Nguyen, N.T., Walton, A.J., Flewitt, A.J., Zu, X.T., Li, Y., McHale, G., Matthews, A., Iborra, E., Du, H., Milne, W.I., 2017. Advances in piezoelectric thin films for acoustic biosensors, acoustofluidics and lab-on-chip applications. Prog. Mater. Sci. 89, 31–91. https://doi.org/10.1016/j.pmatsci.2017.04.006

Gale, B., Jafek, A., Lambert, C., Goenner, B., Moghimifam, H., Nze, U., Kamarapu, S., 2018. A Review of Current Methods in Microfluidic Device Fabrication and Future Commercialization Prospects. Inventions 3, 60. https://doi.org/10.3390/inventions3030060

Gobby, D., Angeli, P., Gavriilidis, A., 2001. Mixing characteristics of T-type microfluidic mixers. J. Micromechanics Microengineering 11, 126–132. https://doi.org/10.1088/0960-1317/11/2/307

Gray, B.L., Jaeggi, D., Mourlas, N.J., van Drieenhuizen, B.P., Williams, K.R., Maluf, N.I., Kovacs, G.T.A., 1999. Novel interconnection technologies for integrated microfluidic systems 9.

Green, J., Holdø, A., Khan, A., 2007. A review of passive and active mixing systems in microfluidic devices. Int. J. Multiphysics 1, 1–32. https://doi.org/10.1260/175095407780130544

Hama, B., Mahajan, G., Fodor, P.S., Kaufman, M., Kothapalli, C.R., 2018. Evolution of mixing in a microfluidic reverse-staggered herringbone micromixer. Microfluid. Nanofluidics 22, 54. https://doi.org/10.1007/s10404-018-2074-0

Hardt, S., Schönfeld, F., 2003. Laminar mixing in different interdigital micromixers: II. Numerical simulations. AIChE J. 49, 578–584. https://doi.org/10.1002/aic.690490305

Harrson Santana, Rodrigo L. Amaral, Osvaldir Pereira Taranto, 2015. Numerical study of mixing and reaction for biodiesel production in spiral microchannel. Chem. Eng. Trans. 43, 1663–1668. https://doi.org/10.3303/CET1543278

Hashmi, A., Xu, J., 2014. On the Quantification of Mixing in Microfluidics. J. Lab. Autom. 19, 488–491. https://doi.org/10.1177/2211068214540156

He, X., Xia, T., Gao, L., Deng, Z., Uzoejinwa, B.B., 2019. Simulation and experimental study of asymmetric split and recombine micromixer with D-shaped sub-channels. Micro Nano Lett. 14, 293–298. https://doi.org/10.1049/mnl.2018.5219

Hejazian, M., Nguyen, N.-T., 2017. A Rapid Magnetofluidic Micromixer Using Diluted Ferrofluid. Micromachines 8, 37. https://doi.org/10.3390/mi8020037

Hessel, V., Hardt, S., Löwe, H., Schönfeld, F., 2003. Laminar mixing in different interdigital micromixers: I. Experimental characterization. AIChE J. 49, 566–577. https://doi.org/10.1002/aic.690490304

Hessel, V., Löwe, H., Schönfeld, F., 2005. Micromixers—a review on passive and active mixing principles. Chem. Eng. Sci. 60, 2479–2501. https://doi.org/10.1016/j.ces.2004.11.033

Hong, C.-C., Choi, J.-W., Ahn, C.H., 2004. A novel in-plane passive microfluidic mixer with modified Tesla structures. Lab. Chip 4, 109. https://doi.org/10.1039/b305892a

Hossain, S., Ansari, M.A., Husain, A., Kim, K.-Y., 2010. Analysis and optimization of a micromixer with a modified Tesla structure. Chem. Eng. J. 158, 305–314. https://doi.org/10.1016/j.cej.2010.02.002

Hossain, S., Kim, K.-Y., 2014. Mixing Analysis of Passive Micromixer with Unbalanced Three-Split Rhombic Sub-Channels. Micromachines 5, 913–928. https://doi.org/10.3390/mi5040913

Huang, C., Tsou, C., 2014. The implementation of a thermal bubble actuated microfluidic chip with microvalve, micropump and micromixer. Sens. Actuators Phys. 210, 147–156. https://doi.org/10.1016/j.sna.2014.02.015

Huang, J.J., Lo, Y.J., Hsieh, C.M., Lei, U., Li, C.I., Huang, C.W., n.d. An electro-thermal micro mixer 4.

Huang, K.-R., Chang, J.-S., Chao, S.D., Wung, T.-S., Wu, K.-C., 2012. Study of Active Micromixer Driven by Electrothermal Force. Jpn. J. Appl. Phys. 51, 047002. https://doi.org/10.1143/JJAP.51.047002

Hussain, M., Pöschel, T., Müller, P., 2019. Mixing of rarefied gases in T-shape micromixers. Appl. Therm. Eng. 146, 39–44. https://doi.org/10.1016/j.applthermaleng.2018.09.090

Jain, M., Nandakumar, K., 2010. Novel index for micromixing characterization and comparative analysis. Biomicrofluidics 4, 031101. https://doi.org/10.1063/1.3457121

Jang, L.-S., Chao, S.-H., Holl, M.R., Meldrum, D.R., 2005. Microfluidic circulatory flows induced by resonant vibration of diaphragms 8.

Jeon, H., Massoudi, M., Kim, J., 2017. Magneto-hydrodynamics-driven mixing of a reagent and a phosphate-buffered solution: A computational study. Appl. Math. Comput. 298, 261–271. https://doi.org/10.1016/j.amc.2016.11.026

Jiang, F., Drese, K.S., Hardt, S., Küpper, M., Schönfeld, F., 2004. Helical flows and chaotic mixing in curved micro channels. AIChE J. 50, 2297–2305. https://doi.org/10.1002/aic.10188

Joshua Clark, Miron Kaufman, Petru Fodor, 2018. Mixing Enhancement in Serpentine Micromixers with a Non-Rectangular Cross-Section. Micromachines 9, 107. https://doi.org/10.3390/mi9030107

Kang, H.-J., Choi, B., 2011. Development of the MHD micropump with mixing function. Sens. Actuators Phys. 165, 439–445. https://doi.org/10.1016/j.sna.2010.11.011

Kang, T.G., Hulsen, M.A., Anderson, P.D., n.d. Chaotic mixing induced by a magnetic chain in a rotating magnetic field. Phys. Rev. E 11.

Karthikeyan, K., Sujatha, L., Sudharsan, N.M., 2018. Numerical Modeling and Parametric Optimization of Micromixer for Low Diffusivity Fluids. Int. J. Chem. React. Eng. 16. https://doi.org/10.1515/ijcre-2016-0231

Kazemi, S., Nourian, V., Nobari, M.R.H., Movahed, S., 2017. Two dimensional numerical study on mixing enhancement in micro-channel due to induced charge electrophoresis. Chem. Eng. Process. - Process Intensif. 120, 241–250. https://doi.org/10.1016/j.cep.2017.07.007

Kazemi, Z., Rashidi, S., Esfahani, J.A., 2017. Effect of flap installation on improving the homogeneity of the mixture in an induced-charge electrokinetic micro-mixer. Chem. Eng. Process. Process Intensif. 121, 188–197. https://doi.org/10.1016/j.cep.2017.08.015

Kim, D., Raj, A., Zhu, L., Masel, R.I., Shannon, M.A., n.d. NON-EQUILIBRIUM ELECTROKINETIC NANOFLUIDIC MIXERS 3.

Kim, H.-S., Kim, H.-O., Kim, Y.-J., 2018. Effect of Electrode Configurations on the Performance of Electro-Hydrodynamic Micromixer, in: ASME 2018 16th International Conference on Nanochannels, Microchannels, and Minichannels. Presented at the ASME 2018 16th International Conference on Nanochannels, Microchannels, and Minichannels, American Society of Mechanical Engineers, Dubrovnik, Croatia, p. V001T02A005. https://doi.org/10.1115/ICNMM2018-7654

Kumar, C., Hejazian, M., From, C., Saha, S.C., Sauret, E., Gu, Y., Nguyen, N.-T., 2019a. Modeling of mass transfer enhancement in a magnetofluidic micromixer. Phys. Fluids 31, 063603. https://doi.org/10.1063/1.5093498

Kumar, C., Hejazian, M., From, C., Saha, S.C., Sauret, E., Gu, Y., Nguyen, N.-T., 2019b. Modeling of mass transfer enhancement in a magnetofluidic micromixer. Phys. Fluids 31, 063603. https://doi.org/10.1063/1.5093498

Kunti, G., Bhattacharya, A., Chakraborty, S., 2018. Electrothermally actuated moving contact line dynamics over chemically patterned surfaces with resistive heaters. Phys. Fluids 30, 062004. https://doi.org/10.1063/1.5028172

Kunti, G., Bhattacharya, A., Chakraborty, S., 2017. Rapid mixing with high-throughput in a semi-active semi-passive micromixer: Microfluidics & Miniaturization. ELECTROPHORESIS 38, 1310–1317. https://doi.org/10.1002/elps.201600393

Lee, C.Y., Lin, C., Hung, M.F., Ma, R.H., Tsai, C.H., Lin, C.H., Fu, L.M., 2006. Experimental and Numerical Investigation into Mixing Efficiency of Micromixers with Different Geometric Barriers. Mater. Sci. Forum 505–507, 391–396. https://doi.org/10.4028/www.scientific.net/MSF.505-507.391

Lee, K.Y., Park, S., Lee, Y.R., Chung, S.K., 2016. Magnetic droplet microfluidic system incorporated with acoustic excitation for mixing enhancement. Sens. Actuators Phys. 243, 59–65. https://doi.org/10.1016/j.sna.2016.03.009

Li, Z., Kim, S.-J., 2017. Pulsatile micromixing using water-head-driven microfluidic oscillators. Chem. Eng. J. 313, 1364–1369. https://doi.org/10.1016/j.cej.2016.11.056

Lim, E., Lee, L., Yeo, L.Y., Hung, Y.M., Tan, M.K., 2019. Acoustically Driven Micromixing: Effect of Transducer Geometry. IEEE Trans. Ultrason. Ferroelectr. Freq. Control 66, 1387–1394. https://doi.org/10.1109/TUFFC.2019.2920683

Lim, E., Lee, L., Yeo, L.Y., Hung, Y.M., Tan, M.K., n.d. Acoustically-Driven Micromixing: Effect of Transducer Geometry 1.

Lim, T.W., Son, Y., Jeong, Y.J., Yang, D.-Y., Kong, H.-J., Lee, K.-S., Kim, D.-P., 2011. Three-dimensionally crossing manifold micro-mixer for fast mixing in a short channel length. Lab Chip 11, 100–103. https://doi.org/10.1039/C005325M

Lin, Y., Gerfen, G.J., Rousseau, D.L., Yeh, S.-R., 2003. Ultrafast Microfluidic Mixer and Freeze-Quenching Device. Anal. Chem. 75, 5381–5386. https://doi.org/10.1021/ac0346205

Lion, N., Rohner, T.C., Dayon, L., Arnaud, I.L., Damoc, E., Youhnovski, N., Wu, Z.-Y., Roussel, C., Josserand, J., Jensen, H., Rossier, J.S., Przybylski, M., Girault, H.H., 2003. Microfluidic systems in proteomics. ELECTROPHORESIS 24, 3533–3562. https://doi.org/10.1002/elps.200305629

Liu, F., Zhang, J., Alici, G., Yan, S., Mutlu, R., Li, W., Yan, T., 2016. An inverted micro-mixer based on a magnetically-actuated cilium made of Fe doped PDMS. Smart Mater. Struct. 25, 095049. https://doi.org/10.1088/0964-1726/25/9/095049

Liu, K., Yang, Q., Chen, F., Zhao, Y., Meng, X., Shan, C., Li, Y., 2015. Design and analysis of the cross-linked dual helical micromixer for rapid mixing at low Reynolds numbers. Microfluid. Nanofluidics 19, 169–180. https://doi.org/10.1007/s10404-015-1558-4

Liu, R.H., Stremler, M.A., Sharp, K.V., Olsen, M.G., Santiago, J.G., Adrian, R.J., Aref, H., Beebe, D.J., 2000. Passive mixing in a three-dimensional serpentine microchannel. J. Microelectromechanical Syst. 9, 190–197. https://doi.org/10.1109/84.846699

Liu, R.H., Yang, J., Pindera, M.Z., Athavale, M., Grodzinski, P., 2002. Bubble-induced acoustic micromixing. Lab. Chip 2, 151. https://doi.org/10.1039/b201952c

Löb, P., Drese, K.S., Hessel, V., Hardt, S., Hofmann, C., Löwe, H., Schenk, R., Schönfeld, F., Werner, B., 2004. Steering of Liquid Mixing Speed in Interdigital Micro Mixers– From Very Fast to Deliberately Slow Mixing. Chem. Eng. Technol. 27, 340–345. https://doi.org/10.1002/ceat.200401995

Mao, H., Yang, T., Cremer, P.S., 2002. A Microfluidic Device with a Linear Temperature Gradient for Parallel and Combinatorial Measurements. J. Am. Chem. Soc. 124, 4432–4435. https://doi.org/10.1021/ja017625x

Mariotti, A., Galletti, C., Salvetti, M.V., Brunazzi, E., 2019. Unsteady Flow Regimes in a T-Shaped Micromixer: Mixing and Characteristic Frequencies. Ind. Eng. Chem. Res. 58, 13340–13356. https://doi.org/10.1021/acs.iecr.9b01259

Matsubara, K., Narumi, T., 2016. Microfluidic mixing using unsteady electroosmotic vortices produced by a staggered array of electrodes. Chem. Eng. J. 288, 638–647. https://doi.org/10.1016/j.cej.2015.12.013

Mehrdel, P., Karimi, S., Farré-Lladós, J., Casals-Terré, J., 2018. Novel Variable Radius Spiral–Shaped Micromixer: From Numerical Analysis to Experimental Validation. Micromachines 9, 552. https://doi.org/10.3390/mi9110552

Melin, J., Giménez, G., Roxhed, N., Wijngaart, W. van der, Stemme, G., 2004. A fast passive and planar liquid sample micromixer. Lab Chip 4, 214–219. https://doi.org/10.1039/B314080F

Meng, J., Li, S., Li, J., Yu, C., Wei, C., Dai, S., 2018. AC electrothermal mixing for high conductive biofluids by arc-electrodes. J. Micromechanics Microengineering 28, 065004. https://doi.org/10.1088/1361-6439/aab39b

Milotin, R., Lelea, D., 2016. The Passive Mixing Phenomena in Microtubes with Baffle Configuration. Procedia Technol. 22, 243–250. https://doi.org/10.1016/j.protcy.2016.01.075

Mondal, B., Mehta, S.K., Patowari, P.K., Pati, S., 2019. Numerical study of mixing in wavy micromixers: comparison between raccoon and serpentine mixer. Chem. Eng. Process. - Process Intensif. 136, 44–61. https://doi.org/10.1016/j.cep.2018.12.011

Moroney, R.M., White, R.M., Howe, R.T., 1991. Ultrasonically induced microtransport, in: [1991] Proceedings. IEEE Micro Electro Mechanical Systems. Presented at the IEEE Micro Electro Mechanical Systems, IEEE, Nara, Japan, pp. 277–282. https://doi.org/10.1109/MEMSYS.1991.114810

Mousavi Shaegh, S.A., Nguyen, N.-T., Wereley, S., 2019. Fundamentals and Applications of Microfluidics.

Munson, M.S., Yager, P., 2004. Simple quantitative optical method for monitoring the extent of mixing applied to a novel microfluidic mixer. Anal. Chim. Acta 507, 63–71. https://doi.org/10.1016/j.aca.2003.11.064

Nguyen, N.-T., Hejazian, M., Ooi, C., Kashaninejad, N., 2017. Recent Advances and Future Perspectives on Microfluidic Liquid Handling. Micromachines 8, 186. https://doi.org/10.3390/mi8060186

Nguyen, N.-T., Wu, Z., 2005. Micromixers—a review. J. Micromechanics Microengineering 15, R1–R16. https://doi.org/10.1088/0960-1317/15/2/R01

Nimafar, M., Viktorov, V., Martinelli, M., 2012. Experimental comparative mixing performance of passive micromixers with H-shaped sub-channels. Chem. Eng. Sci. 76, 37–44. https://doi.org/10.1016/j.ces.2012.03.036

Niu, X., Lee, Y.-K., 2003. Efficient spatial-temporal chaotic mixing in microchannels. J. Micromechanics Microengineering 13, 454–462. https://doi.org/10.1088/0960-1317/13/3/316

Nouri, D., Zabihi-Hesari, A., Passandideh-Fard, M., 2017. Rapid mixing in micromixers using magnetic field. Sens. Actuators Phys. 255, 79–86. https://doi.org/10.1016/j.sna.2017.01.005

Oh, K.W., Lee, K., Ahn, B., Furlani, E.P., 2012. Design of pressure-driven microfluidic networks using electric circuit analogy. Lab Chip 12, 515–545. https://doi.org/10.1039/C2LC20799K

Orbay, S., Ozcelik, A., Lata, J., Kaynak, M., Wu, M., Huang, T.J., 2017a. Mixing high-viscosity fluids via acoustically driven bubbles. J. Micromechanics Microengineering 27, 015008. https://doi.org/10.1088/0960-1317/27/1/015008

Orbay, S., Ozcelik, A., Lata, J., Kaynak, M., Wu, M., Huang, T.J., 2017b. Mixing high-viscosity fluids via acoustically driven bubbles. J Micromech Microeng 7.

Owen, D., Ballard, M., Alexeev, A., Hesketh, P.J., 2016. Rapid microfluidic mixing via rotating magnetic microbeads. Sens. Actuators Phys. 251, 84–91. https://doi.org/10.1016/j.sna.2016.09.040

Parsa, M.K., Hormozi, F., 2014. Experimental and CFD modeling of fluid mixing in sinusoidal microchannels with different phase shift between side walls. J. Micromechanics Microengineering 24, 065018. https://doi.org/10.1088/0960-1317/24/6/065018

Peng, R., Li, D., 2015. Effects of ionic concentration gradient on electroosmotic flow mixing in a microchannel. J. Colloid Interface Sci. 440, 126–132. https://doi.org/10.1016/j.jcis.2014.10.061

Qi, A., Yeo, L.Y., Friend, J.R., 2008. Interfacial destabilization and atomization driven by surface acoustic waves. Phys. Fluids 20, 074103. https://doi.org/10.1063/1.2953537

Rafeie, M., Welleweerd, M., Hassanzadeh-Barforoushi, A., Asadnia, M., Olthuis, W., Ebrahimi Warkiani, M., 2017. An easily fabricated three-dimensional threaded lemniscate-shaped micromixer for a wide range of flow rates. Biomicrofluidics 11, 014108. https://doi.org/10.1063/1.4974904

Raza, W., Kim, K.-Y., 2020. Unbalanced Split and Recombine Micromixer with Three-Dimensional Steps. Ind. Eng. Chem. Res. 59, 3744–3756. https://doi.org/10.1021/acs.iecr.9b00682

SadAbadi, H., Packirisamy, M., Wüthrich, R., 2013. High performance cascaded PDMS micromixer based on split-and-recombination flows for lab-on-a-chip applications. RSC Adv. 3, 7296. https://doi.org/10.1039/c3ra40910d

Sadegh Cheri, M., Latifi, H., Salehi Moghaddam, M., Shahraki, H., 2013. Simulation and experimental investigation of planar micromixers with short-mixing-length. Chem. Eng. J. 234, 247–255. https://doi.org/10.1016/j.cej.2013.08.067

Samiei, E., Tabrizian, M., Hoorfar, M., 2016. A review of digital microfluidics as portable platforms for lab-on a-chip applications. Lab. Chip 16, 2376–2396. https://doi.org/10.1039/C6LC00387G

Saroj, S.K., Asfer, M., Sunderka, A., Panigrahi, P.K., 2016. Two-fluid mixing inside a sessile micro droplet using magnetic beads actuation. Sens. Actuators Phys. 244, 112–120. https://doi.org/10.1016/j.sna.2016.04.004

Sasaki, N., Kitamori, T., Kim, H.-B., 2012. Fluid mixing using AC electrothermal flow on meandering electrodes in a microchannel: Microfluidics and Miniaturization. ELECTROPHORESIS 33, 2668–2673. https://doi.org/10.1002/elps.201200099

Scherr, T., Quitadamo, C., Tesvich, P., Park, D.S.-W., Tiersch, T., Hayes, D., Choi, J.-W., Nandakumar, K., Monroe, W.T., 2012. A planar microfluidic mixer based on

logarithmic spirals. J. Micromechanics Microengineering 22, 055019. https://doi.org/10.1088/0960-1317/22/5/055019

Schönfeld, F., Hardt, S., 2004. Simulation of helical flows in microchannels. AIChE J. 50, 771–778. https://doi.org/10.1002/aic.10071

Schwesinger, N., Frank, T., Wurmus, H., 1996. A modular microfluid system with an integrated micromixer. J. Micromechanics Microengineering 6, 99–102. https://doi.org/10.1088/0960-1317/6/1/023

Shamloo, A., Mirzakhanloo, M., Dabirzadeh, M.R., 2016. Numerical Simulation for efficient mixing of Newtonian and non-Newtonian fluids in an electro-osmotic micro-mixer. Chem. Eng. Process. - Process Intensif. 107, 11–20. https://doi.org/10.1016/j.cep.2016.06.003

Sheu, T.S., Chen, S.J., Chen, J.J., 2012. Mixing of a split and recombine micromixer with tapered curved microchannels. Chem. Eng. Sci. 71, 321–332. https://doi.org/10.1016/j.ces.2011.12.042

Sudarsan, A.P., Ugaz, V.M., 2006. Fluid mixing in planar spiral microchannels. Lab Chip 6, 74–82. https://doi.org/10.1039/B511524H

Tan, H., 2019. Numerical study of a bubble driven micromixer based on thermal inkjet technology. Phys. Fluids 31, 062006. https://doi.org/10.1063/1.5098449

Tran-Minh, N., Dong, T., Karlsen, F., 2014. An efficient passive planar micromixer with ellipse-like micropillars for continuous mixing of human blood. Comput. Methods Programs Biomed. 117, 20–29. https://doi.org/10.1016/j.cmpb.2014.05.007

Tsai, R.-T., Wu, C.-Y., 2011. An efficient micromixer based on multidirectional vortices due to baffles and channel curvature. Biomicrofluidics 5, 014103. https://doi.org/10.1063/1.3552992

Usefian, A., Bayareh, M., 2019. Numerical and experimental study on mixing performance of a novel electro-osmotic micro-mixer. Meccanica 54, 1149–1162. https://doi.org/10.1007/s11012-019-01018-y

Usefian, A., Bayareh, M., Shateri, A., Taheri, N., 2019. Numerical study of electro-osmotic micro-mixing of Newtonian and non-Newtonian fluids. J. Braz. Soc. Mech. Sci. Eng. 41, 238. https://doi.org/10.1007/s40430-019-1739-2

Vanka, S.P., Winkler, C.M., Coffman, J., Linderman, E., Mahjub, S., Young, B., 2003. Novel Low Reynolds Number Mixers for Microfluidic Applications, in: Volume 2: Symposia, Parts A, B, and C. Presented at the ASME/JSME 2003 4th Joint Fluids Summer Engineering Conference, ASMEDC, Honolulu, Hawaii, USA, pp. 887–892. https://doi.org/10.1115/FEDSM2003-45122

Veldurthi, N., 2015. Computational fluid dynamic analysis of poly(dimethyl siloxane) magnetic actuator based micromixer 6.

Veldurthi, N., Chandel, S., Bhave, T., Bodas, D., 2015. Computational fluid dynamic analysis of poly(dimethyl siloxane) magnetic actuator based micromixer. Sens. Actuators B Chem. 212, 419–424. https://doi.org/10.1016/j.snb.2015.02.048

Vijayendran, R.A., Motsegood, K.M., Beebe, D.J., Leckband, D.E., 2003. Evaluation of a Three-Dimensional Micromixer in a Surface-Based Biosensor †. Langmuir 19, 1824–1828. https://doi.org/10.1021/la0262250

Viktorov, V., Mahmud, M.R., Visconte, C., 2016. Numerical study of fluid mixing at different inlet flow-rate ratios in Tear-drop and Chain micromixers compared to a new H-C passive micromixer. Eng. Appl. Comput. Fluid Mech. 10, 182–192. https://doi.org/10.1080/19942060.2016.1140075

Walker, G., 2004. Cell infection within a microfluidic device using virus gradients. Sens. Actuators B Chem. 98, 347–355. https://doi.org/10.1016/j.snb.2003.10.014

Wang, H., Iovenitti, P., Harvey, E., Masood, S., 2002. Optimizing layout of obstacles for enhanced mixing in microchannels. Smart Mater. Struct. 11, 662–667. https://doi.org/10.1088/0964-1726/11/5/306

Wang, L., Ma, S., Wang, X., Bi, H., Han, X., 2014. Mixing enhancement of a passive microfluidic mixer containing triangle baffles: PASSIVE MICROMIXER CONTAINING TRIANGLE BAFFLES. Asia-Pac. J. Chem. Eng. 9, 877–885. https://doi.org/10.1002/apj.1837

Wang, S.S., Jiao, Z.J., Huang, X.Y., Yang, C., Nguyen, N.T., 2009. Acoustically induced bubbles in a microfluidic channel for mixing enhancement. Microfluid. Nanofluidics 6, 847–852. https://doi.org/10.1007/s10404-008-0357-6

Wasim Raza, Sang-Bum Ma, Kwang-Yong Kim, 2018. Multi-Objective Optimizations of a Serpentine Micromixer with Crossing Channels at Low and High Reynolds Numbers. Micromachines 9, 110. https://doi.org/10.3390/mi9030110

Whitesides, G.M., 2006. The origins and the future of microfluidics. Nature 442, 368–373. https://doi.org/10.1038/nature05058

Whulanza, Y., Utomo, M.S., Hilman, A., 2018. Realization of a passive micromixer using herringbone structure. Presented at the 2ND BIOMEDICAL ENGINEERING'S RECENT PROGRESS IN BIOMATERIALS, DRUGS DEVELOPMENT, AND MEDICAL DEVICES: Proceedings of the International Symposium of Biomedical Engineering (ISBE) 2017, Bali, Indonesia, p. 040003. https://doi.org/10.1063/1.5023973

Wong, S., Ward, M., Wharton, C., 2004. Micro T-mixer as a rapid mixing micromixer. Sens. Actuators B Chem. 100, 359–379. https://doi.org/10.1016/j.snb.2004.02.008

Wu, J.W., Xia, H.M., Zhang, Y.Y., Zhao, S.F., Zhu, P., Wang, Z.P., 2019. An efficient micromixer combining oscillatory flow and divergent circular chambers. Microsyst. Technol. 25, 2741–2750. https://doi.org/10.1007/s00542-018-4193-7

Xia, Q., Zhong, S., 2013. Liquid mixing enhanced by pulse width modulation in a Y-shaped jet configuration. Fluid Dyn. Res. 45, 025504. https://doi.org/10.1088/0169-5983/45/2/025504

Yang, A.-S., Chuang, F.-C., Chen, C.-K., Lee, M.-H., Chen, S.-W., Su, T.-L., Yang, Y.-C., 2015. A high-performance micromixer using three-dimensional Tesla structures for bio-applications. Chem. Eng. J. 263, 444–451. https://doi.org/10.1016/j.cej.2014.11.034

Yang, J., Qi, L., Chen, Y., Ma, H., 2013. Design and Fabrication of a Three Dimensional Spiral Micromixer. Chin. J. Chem. 31, 209–214. https://doi.org/10.1002/cjoc.201200922

Yang, Z., Matsumoto, S., Goto, H., Matsumoto, M., Maeda, R., 2001. Ultrasonic micromixer for micro¯uidic systems 7.

Yaralioglu, G.G., Wygant, I.O., Marentis, T.C., Khuri-Yakub, B.T., 2004. Ultrasonic Mixing in Microfluidic Channels Using Integrated Transducers. Anal. Chem. 76, 3694–3698. https://doi.org/10.1021/ac035220k

Yoshimura, M., Shimoyama, K., Misaka, T., Obayashi, S., 2019. Optimization of passive grooved micromixers based on genetic algorithm and graph theory. Microfluid. Nanofluidics 23, 30. https://doi.org/10.1007/s10404-019-2201-6

Zhang, F., Chen, H., Chen, B., Wu, J., 2016. Alternating current electrothermal micromixer with thin film resistive heaters. Adv. Mech. Eng. 8, 168781401664626. https://doi.org/10.1177/1687814016646264

Zhang, J., He, G., Liu, F., 2006. Electro-osmotic flow and mixing in heterogeneous microchannels. Phys. Rev. E 73, 056305. https://doi.org/10.1103/PhysRevE.73.056305

Zhang, K., Ren, Y., Hou, L., Feng, X., Chen, X., Jiang, H., 2018. An efficient micromixer actuated by induced-charge electroosmosis using asymmetrical floating electrodes. Microfluid. Nanofluidics 22, 130. https://doi.org/10.1007/s10404-018-2153-2

Zhang, S., Chen, X., Wu, Z., Zheng, Y., 2019. Numerical study on stagger Koch fractal baffles micromixer. Int. J. Heat Mass Transf. 133, 1065–1073. https://doi.org/10.1016/j.ijheatmasstransfer.2019.01.009

Zhang, Zhang, Wu, Shen, Chen, Lan, Li, Cai, 2019. Comparison of Micro-Mixing in Time Pulsed Newtonian Fluid and Viscoelastic Fluid. Micromachines 10, 262. https://doi.org/10.3390/mi10040262

Zhao, W., Yang, F., Wang, K., Bai, J., Wang, G., 2017. Rapid mixing by turbulent-like electrokinetic microflow. Chem. Eng. Sci. 165, 113–121. https://doi.org/10.1016/j.ces.2017.02.027

LIST OF PUBLICATIONS

Published paper in International Journals

i. Mustafa, M. G., Zunaid, M., & Gautam, S. (2023). Numerical Analysis and Moth Flame Optimization of Passive T-Micromixer with Twist and Bend mixing channel. Chemical Engineering and Processing - Process Intensification, 109436. (SCIE, Impact Factor-3.8 (JCR 2022)) doi.org/10.1016/j.cep.2023.109436.

ii. Mustafa, M. G., Zunaid, M., & Gautam, S. (2024). Optimizing passive micromixers: Enhancing mixing efficiency through computational fluid dynamics and metaheuristic algorithms. The Canadian Journal of Chemical Engineering. (SCIE, Impact Factor-1.6 (JCR 2022) doi.org/10.1002/cjce.25566.

Paper Presented/Published in International Conferences

i. Gulam Mustafa Md. and Zunaid, M. and S. (2024). Numerical Analysis of Helical Spiral Micromixer of Non-Newtonian Fluid. ICMech-REC-2023, NIT Warangal, June 2023. Recent Advances in Mechanical Engineering, Volume 1 (pp. 341–351). Scopus Indexed Proceeding. doi.org/10.1007/978-981-97-0918-2_27

ii. Mustafa, M. G., Zunaid, M., & Gautam, S. (2023). A novel passive micromixer model computational analysis with twist and bend. Journal of Physics: Conference Series. Ist International Conference on Material Science, Mechanics and Technology (ICMMT 2022), Sushila Devi Bansal College of Technology, Indore. Scopus Indexed doi.org/10.1088/1742-6596/2484/1/012041

CURRICULUM VITAE

Md Gulam Mustafa

Research Scholar | Mechanical Engineering | Computational Fluid Dynamics

Md Gulam Mustafa is a dedicated research scholar at Delhi Technological University, specializing in computational fluid dynamics and finite element analysis. With a strong academic background, he holds a Ph.D. in Mechanical Engineering, focusing on computational analysis for mixing Newtonian and non-Newtonian fluids in 3D micromixers. His expertise extends to machine learning applications, Python programming, Ansys Workbench, and SolidWorks.

I have extensive teaching and research experience as a Teaching Assistant in the Department of Mechanical Engineering at Delhi Technological University since 2019. His research contributions include numerous publications in reputed journals and conferences, covering lithium-ion battery cooling, passive micromixers, and wind turbine blade optimization.

His skill set encompasses MS Office, modelling, and numerical simulations, with a keen interest in renewable energy and fluid mechanics. He aims to advance the understanding of fluid dynamics in microfluidic systems through his research, contributing to energy efficiency and mechanical engineering design.

Key Skills: Machine Learning, Python, Computational Fluid Dynamics, Finite Element Analysis, Ansys Workbench, SolidWorks, Renewable Energy Technologies.

LinkedIn: MD Gulam Mustafa
Email: gm09mes31@gmail.com